Pyrite Precipitation Around the 2.63 Gya Spherule Layer

By

EMILIA SAKAI HERNANDEZ
DISSERTATION

Submitted in partial satisfaction of the requirements for the degree of

DOCTOR OF PHILOSOPHY

in

Earth AND Planetary Sciences

in the

OFFICE OF GRADUATE STUDIES

of the

UNIVERSITY OF CALIFORNIA

DAVIS

Approved:

Dawn Sumner, Chair

Isabel Montañez

Kenneth Williford

Committee in Charge

2023

For my grandpa, who always encouraged me to pursue science.

Contents

Abstract

At about 2.65 Gya, the concentration of sulfide minerals increased in the Monteville Formation, Campbellrand Subgroup, Transvaal Supergroup, Griqualand West Basin, South Africa. Many textures of sulfides show evidence of pre-compaction lithification, suggesting that reduced sulfur and iron were available in the sedimentary environment. A large, Chixulub-scale meteorite impact during this sulfidic event does not change the concentration or morphology of pyrite, indicating that this event did not have long-term effects on the sulfur cycle.

Pyrite morphology can reveal how pyrite formed. The relative timing of formation of different textures of pyrite can be used to infer when during sedimentation and diagenesis a particular piece of pyrite formed. Such textural relationships have been used to reconstruct geobiological (*Meyer et al.*, 2017) and geochemical (*Izon et al.*, 2022) processes in the sulfur cycle in Archean-age rocks. The use of in situ analyses of sedimentary pyrite can be contrasted with whole-rock geochemical analyses which have been used to investigate long-term trends in trace element and redox conditions. However, late-stage diagenesis, metamorphism, and hydrothermal activity can affect pyrite geochemical signatures. An understanding of pyrite formation processes is essential for linking redox changes in the Neoarchean across continents (*Cui et al.*, 2018; *Partridge et al.*, 2008). This chapter illustrates a variety of pyrite textures observed in cores spanning the 2.65-2.63 Ga Jeerinah Formation, Western Australia, through a euxinic interval. Where possible, models for formation mechanisms are discussed. This work provides key constraints on the formation of various pyrite phases and helps refine prior interpretation of geochemical signatures through the euxinic interval.

The 2.63 Gya Jeerinah Formation contains pyrite nodules that show textural evidence of having precipitated on the Neoarchean seafloor. Shale and thin carbonate turbidites lap onto the nodules, demonstrating relief on the seafloor over the nodules. In addition, overhanging pyrite growths produced shelter porosity later filled with calcite. The petrographic textures at the tops of the nodules are sometimes laminated and columnar in contrast to euhedral crystal forms at the bases of nodules, demonstrating different growth conditions upward versus downward. This differential growth of nodules at the seafloor is analogous to polymetallic manganese nodules in the modern ocean. These very unusual iron sulfide seafloor nodules suggest that iron and sulfur cycling may

have been unique in Earth history during this ca. 20 Ma interval, consistent with an overall exceptionally high concentration of pyrite in a subtidal siliciclastic/carbonate ramp of this age.

Acknowledgments

No ideas exist in isolation. The words within this thesis are a synthesis of countless interactions with family, friends, and colleagues who have shaped my thinking. The following list is not exhaustive, I am just exhausted. My first attempts to write this down came as a result of conversations at CIDER 2022, out of which grew the Earthlikeness group that gives me hope of a better, more inclusive future for the field of Astrobiology.

This work owes an immense debt to my thesis advisor, Dawn Sumner. Thank you for hours of great, wide-ranging conversations and for the way that you do science. Thanks to my lab twin, Sydney Salley, for being an amazing field mate and for your support through the years. To Christy Grettenberger, for your sense of humor, "saw this paper and thought of you" messages, and for being such an amazing role model. To Sarah King, Kaylah Marcello, Michelle Tran, and Tyler Powell for continuing necessary work in and out of the lab. To Tyler Mackey, for letting me use your microscope, and to Jared Clance, for showing me around UNM and talking to me about petrography. To Austin Behmer, thanks for your friendship and research help – we both did it!

I also must extend my gratitude to the other members of my thesis committee, whose expertise and guidance has been instrumental in shaping this research and enriching my academic journey. Isabel Montañez, your ability to bring Precambrian geology back to sedimentary basics challenged me to think critically and greatly refined this work. Ken Williford, your expertise in petrography was essential to the management of my data.

To the other UC Davis Earth and Planetary Science grad students, particularly the cohort that came in with me. We went through so much together that is impossible to describe to anyone who was not there. I could not have made it through those things without you.

This endeavor would not have been possible without the friends that I have been lucky to live with and around. Living with you and spending time with you has been a refuge from the demands of academia. Game nights and shared meals during my busiest moments provided balance and joy to my life. Esha, I feel so lucky that we met. From nights on the porch our first year, to knitting together for hours, to always having a great book recommendation, my life is forever improved because of your friendship. Isabel, you have always been a great friend to talk to and watch TV with. Elena, thank you for making me coffee in the morning and for your infectious humor. Agatha,

thank you for box cake and great movie suggestions. To Karen, Peter, and Omar, I could not have asked for a better group of people to spend three months of COVID lockdown with.

To my parents and grandparents, thank you for supporting me all the way though my education. Maia and Paul, thank you for often knowing me better than myself. So much of my success I owe to your love and sacrifices.

Finally, my endless gratitude to my incredible partner, Dandhi'on, for putting up with my thesis grumpiness and for helping me deal with the basics of existence during the depths of writing.

I also must acknowledge the Land on which UC Davis stands and where the bulk of this work was done. For thousands of years, this land has been the home of the Patwin people. Today, there are three federally recognized Patwin tribes: Cachil DeHe Band of Wintun Indians of the Colusa Indian Community, Kletsel Dehe Wintun Nation, and Yocha Dehe Wintun Nation. The Patwin people have remained committed to the stewardship of this land over many centuries. It has been cherished and protected, as elders have instructed the young through generations. I am honored and grateful to have been there on their traditional lands. I also acknowledge the ancestral lands of the Dena people of the lower Tanana River, where I am finishing this thesis. Undertaking this work caused me to examine my and my fields' assumed access to native land. My fieldwork was done in South Africa and my core samples are from the Pilbara region of Western Australia. The model of science that I was taught and that I perpetuated did not and does not allow for proper relationships with Land and Country. I hope that whoever reads and uses this work does a better job than I have.

CHAPTER 1

Stability of Sulfide-Rich Microbial Ecosystems Across a Giant Impact

1.1. Abstract

At about 2.65 Gya, the concentration of sulfide minerals increased in the Monteville Formation, Campbellrand Subgroup, Transvaal Supergroup, Griqualand West Basin, South Africa. Many textures of sulfides show evidence of pre-compaction lithification, suggesting that reduced sulfur and iron were available in the sedimentary environment. A large, Chixulub-scale meteorite impact during this sulfidic event does not change the concentration or morphology of pyrite, indicating that this event did not have long-term effects on the sulfur cycle.

1.2. Introduction

1.2.1. The Archean Sulfur Cycle around 2.63 Gya. Earth's surface oceans provided a source of reductants that consumed photosynthetically produced oxygen leading up to the Great Oxygenation Event (GOE). Marine records in this interval record significant changes in the concentration of reduced iron in seawater as well as major changes in the sulfur cycle (*Eigenbrode and Freeman*, 2006; *Izon et al.*, 2022; *Mishima et al.*, 2017; *Olson et al.*, 2019; *Ostrander et al.*, 2021; *Sen et al.*, 2022). From about 2.8 Ga through the GOE, volumetrically significant banded iron formation (BIF) accumulated on marine shelves below wave base while near-shore sedimentation patterns were broadly similar to those seen today, including carbonate platform growth in shallow, warm waters and shale deposition where there was a sufficient supply of siliciclastics. Facies distributions suggest a deep marine source of reduced iron for most BIF (*Araújo and Lobato*, 2019; *Heard et al.*, 2020; *Muhling and Rasmussen*, 2020; *Sindhuja et al.*, 2020). Similarly, sulfur isotopic patterns suggest low but increasing shallow marine sulfate concentrations through the Neoarchean. Sulfate concentrations were likely low (< 100 µM) until about 2.4 Gya (*Crowe et al.*, 2014; *Farquhar*

et al., 2013; *Jamieson et al.*, 2013; *Paris et al.*, 2014), but the increasingly large mass independent fractionations leading up to the GOE are consistent with significant changes in the details of the sulfur cycle (*Johnston*, 2011).

Embedded within this overall trend is a highly pyritic interval at about 2.65 Gya when the concentration of pyrite in marine shales increased and stayed elevated for tens of meters of sediment. This interval has been interpreted as long-lasting euxinia or a geochemical state characterized by elevated water column concentration of sulfide (*Ostrander et al.*, 2021). This euxinic event has been most closely studied in the Jeerinah Formation, Fortescue Supergroup, Hamersley Basin, Western Australia (*Koehler et al.*, 2018; *Olson et al.*, 2019; *Ostrander et al.*, 2021). However, this event is well correlated to the Monteville Formation, South Africa, through sequence stratigraphy and the presence of an impact spherule marker bed (*Simonson et al.*, 2009a,b). The similarity between sulfidic textures in these different basins across this interval has been noted (*Knoll and Beukes* (2009), Chapters 2, 3). This elevated sulfide likely had significant influences on the sedimentology and biology of marine ecosystems in this Archean interval.

A plausible source for this elevated sulfide being delivered to the oceans is an increase in oxidative weathering and oxygen in the surface environment (*Ostrander et al.*, 2021). This biologically oxidized sulfur has been proposed to be a significant source of sulfur to the oceans since at least 2.7 Gya (*Stüeken et al.*, 2012). The 2.63 Ga euxinic event contains high positive (4-6‰) $\delta^{15}N$ values, which require nitrate to be present in the environment. Further supporting the potential role for terrestrial oxidative weathering is the fact that molybdenum (*Olson et al.*, 2019) and selenium (*Koehler et al.*, 2018) also increase in a near-shore core, AIDP-2, from the Jeerinah Formation. These metals are more soluble in oxidizing conditions and insoluble in sulfidic conditions. However, a coeval increase in molybdenum is not observed in deep-water cores AIDP-3 and FGV-1, suggesting that riverine-transported molybdenum and selenium may have become depleted between the deposition of the two cores. Euxinia and oxidizing conditions may have therefore been a local phenomenon.

An alternate hypothesis for the source of sulfur to 2.63 Ga oceans is from an increase in subaerial volcanism (*Olson et al.*, 2019; *Scott et al.*, 2011). Supporting this model is the observation of non-zero $\Delta^{33}S$ in bulk pyrite through the Jeerinah Formation (*Ono et al.*, 2003) which is created through

photochemical reactions in an atmosphere without ozone, and therefore molecular oxygen (*Farquhar et al.*, 2000, 2001). This model is preferred to account for the observation that ion transport in oxidized, riverine environments averages out $\Delta^{33}S$ (*Torres et al.*, 2018); however, the preservation of non-zero $\Delta^{33}S$ throughout the Archean requires less active sulfur cycling overall.

1.2.2. The 2.63 Gya Giant Impact. Within the euxinic interval, at 2.63 Gya, an ordinary chondritic meteorite hit the seafloor, ejecting irregular melt particles and condensation spherules $>$ 1000 km from the impact crater (*Simonson et al.*, 2018). The impact spherules are chemically and texturally distinct from those in other impact layers and provide a precise chronostratigraphic correlation across facies boundaries (*Glass and Simonson*, 2013; *Jones-Zimberlin*, 2006; *Simonson and Glass*, 2004; *Simonson et al.*, 2009a,b; *Sumner and Beukes*, 2006). This impact horizon has been identified in subtidal environments ranging from basinal shales to shallow water carbonates in the Monteville Formation (*Simonson et al.*, 2000b, 2018), deep subtidal environments in the Roy Hill Shale, Western Australia (*Simonson et al.*, 2000a), and platformal to lagoonal carbonates in the Carawine Dolomite, Western Australia (*Glass and Simonson*, 2013; *Simonson et al.*, 2000b).

The impact created tsunamis that ripped up existing subtidal marine muds, caused collapse of a carbonate platform margin, created wave-rippled grainstones below storm-wavebase, and transported terrestrial quartz sand into sub-wavebase depositional environments (*Glass and Simonson*, 2013; *Hassler and Simonson*, 2001; *Jones-Zimberlin*, 2006; *Simonson et al.*, 1999). In places, the impact horizon contains boulder-sized clasts of platformal carbonates as well as smaller clasts of subtidal carbonates, argillite, and pyrite, indicating that this mass sediment transport event moved material from many different environments (see *Glass and Simonson* (2013).

An oceanic impact could have mixed the stratified Archean ocean (*Glikson*, 2006, 2010, 2008). Additionally, large meteorite impacts create long-lasting hydrothermal systems, which could plausibly affect ocean chemistry in the case of an oceanic impact (*Glikson*, 2006). A temporal link between banded iron formation and this impact has been proposed as a long-lasting consequence of these processes (*Glikson*, 2006) However, this hypothesis requires testing of the stratigraphic and sedimentological trends around the impact.

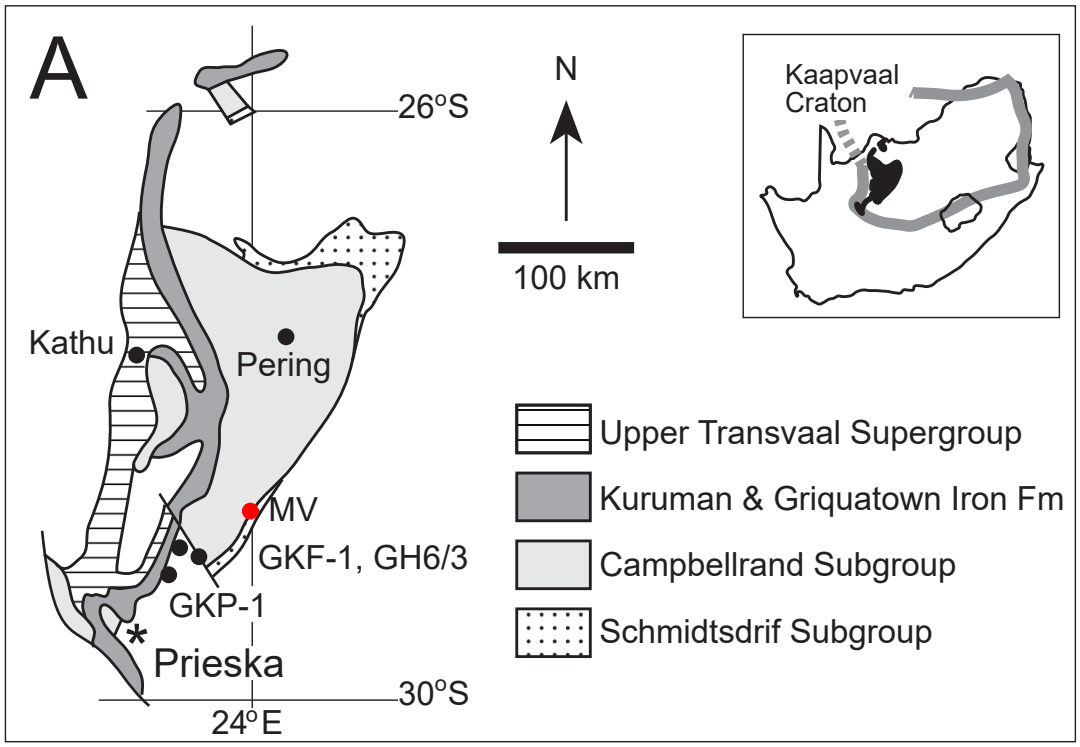

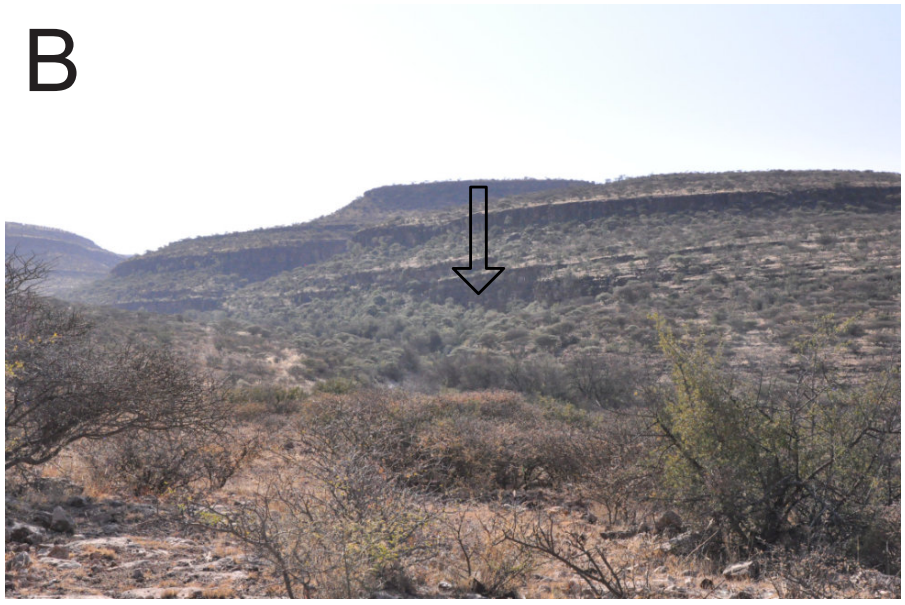

Figure 1.1. **A:** Map of the location of Monteville Farm (red MV(and other cores that contain the MSL. **B:** Black arrow marks the location of the MSL from the approach to the field site.

1.2.3. Geologic Context. At the time of the 2.63 Ga impact, much of the Kaapvaal Craton was exposed to erosion and fluvial deposition, preserved as the Black Reef Formation (*Nwaila et al.*, 2020, 2019), with the accumulation of mixed siliciclastic-carbonate marine deposits of the Monteville Formation on the west side of the craton (*Sumner and Beukes* (2006); Figure 1.1). The eroding bedrock of the Kaapvaal Craton was composed of the fluvial Mesoarchean Witswatersrand Supergroup and the overlying volcanic ca. 2.7 Ga Ventersdorp Supergroup. Witswatersrand quartzites contain detrital pyrite and uraninite, demonstrating a reduced sedimentary environment (*Nwaila et al.*, 2019). The Ventersdorp consists of continental flood basalts like modern-day Hawaiian and Icelandic volcanism (*Nwaila et al.*, 2020). Lacustrine deposits within rift basins in the Ventersdorp contain lacustrine stromatolites with evidence of sufficient local oxygenic photosynthesis to oxidize reduced iron, although the lake water remained anoxic (*Wilmeth et al.*, 2019, 2022). Subsequent contact metamorphism produced sulfide-rich deposits in the Ventersdorp Contact Reef. The overlying Black Reef Formation consists of a deepening upward sequence of rocks consisting of conglomerates at the base, followed by interbedded quartz arenites and shales indicative of subaerial to subtidal environment, and capped by a layer of carbonaceous shale (*Nwaila et al.*, 2020). The contemporaneous Monteville Formation represents equivalent deepening upward marine deposits (*Sumner and Beukes*, 2006).

The Witwatersrand and Ventersdorp supergroups provided sulfur-rich source rocks for the Blackreef and Monteville formations. Specifically, cobbles of the Ventersdorp Contact Reef were re-deposited in conglomerates within the Black Reef Formation (*Nwaila et al.*, 2019). Conditions in this riverine environment were reducing enough to preserve rounded grains of conglomeritic detrital pyrite, which are found alongside diagenetic and epigenetic pyrite (*Nwaila et al.*, 2020). However, evidence of oxygenic photosynthesis in older lakes suggests that some sulfide minerals may have oxidized during weathering, leading to an influx of sulfur-containing ions into the marine basin. Thus, both aqueous and detrital sources of sulfur were likely available during deposition of the Monteville Formation.

1.2.4. The Monteville Formation. To evaluate the effects of the impact on the sulfur cycle, we chose to study the Monteville Formation at the Monteville Farm locality, as this site exposes the euxinic event and the impact horizon along ≈ 40 m of cliff face. This outcrop-scale exposure

of mixed slope carbonates and shales allowed us to observe and the lateral continuity of sulfide deposition above and below the impact spherule layer. As a result, we were able to observe whether sulfide deposition was indicative of broader stratigraphic trends and characterize decameter to meter-scale sedimentary structures that could provide more detailed environmental interpretations.

The impact horizon is near the base of the Monteville Formation in a breccia layer (*Simonson et al.*, 2018) called the Monteville Spherule Layer or MSL. A tuff $\approx$ 50 meters below the MSL has been dated to 2650$\pm$8 Mya, while the Reivilo spherule layer, which is 200-300 m above the MSL, has been dated to 2.57 Gya. (*Glass and Simonson*, 2013). The Monteville Formation is the lowermost unit of the Campbellrand Subgroup of the Transvaal Supergroup in the Griqualand West Basin, South Africa (*Sumner and Beukes* (2006), Figure 1.1). The mixed siliciclastic and carbonate ramp represents a transition between the underlying shale-rich Lokammona Formation and the overlying carbonate-rich Reivillo Formation. It is the last unit deposited in a ramp geometry before the growth of the shallow-water carbonate platform of the Reivillo Formation.

1.3. Methods

Two stratigraphic columns were collected 15 meters apart at the Monteville Farm locality. The stratigraphy was the same between columns, so the stratigraphic column presented in Figure 2 represents a compilation of the two measured sections. Sections were measured using a Jacob's staff marked at 10 cm intervals. All beds thicker than 5 cm were logged, and the proportions of chert, carbonate, shale, and morphology of PP were recorded. Some thinner beds of PP-rich shale were logged. Beds were traced along the outcrop to observe lateral variability and to better understand the complexity of dewatering structures and microbialites.

Interpretations of original outcrop composition were guided by observations of unweathered cores through the same interval. Hand samples were collected from the field of various textures and examined with a hand lens.

1.4. Results

1.4.1. Stratigraphic column from Monteville Farm. Slightly more than 10 meters of section are exposed with a lateral extent of about 40 m, with no covered intervals. However, many beds are stained a deep red color due to oxidative weathering following Phanaerozoic exposure.

These rocks also often contain black nodules of chert. These nodules have the same morphology as pyrite nodules and concretions observed in contemporaneous cores, which lack the red staining (1.3; Chapters 2 and 3). Our interpretation is that in outcrop, pyrite was oxidized to iron oxides and oxyhydroxides and was replaced by chert pseudomorphs. As a result, we refer to the black chert nodules seen in outcrop as pyrite pseudomorphs (PP). This interpretation fits with the framework established in *Kohl et al.* (2006).

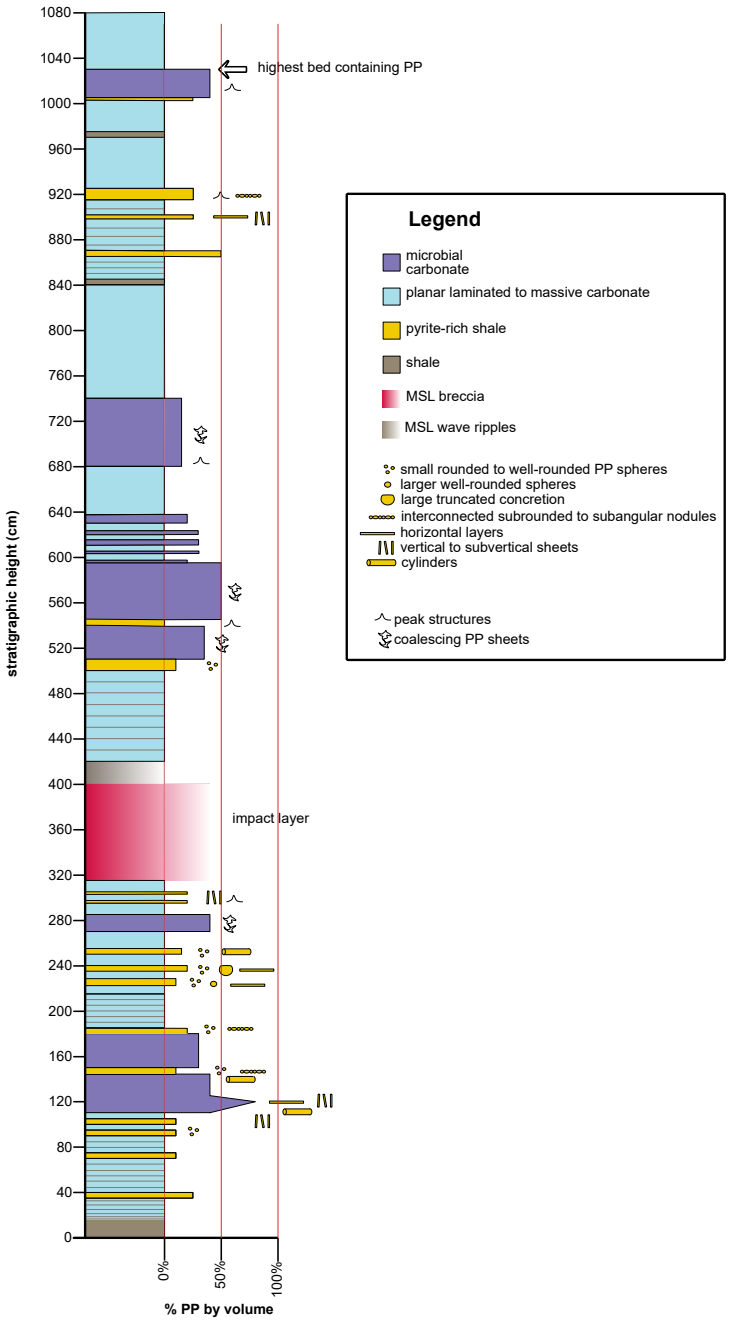

Figure 1.2. Stratigraphic column of the MSL and surrounding strata. Vertical axis is stratigraphic height in centimeters, horizontal axis is % PP by volume. Shale with $< 5\%$ PP by volume is represented with gray. Carbonate with $< 5\%$ PP by volume is represented with blue. Shale interbeds within planar laminated carbonate are represented with gray lines, with the proportion of gray being proportional to the amount of shale. Shale with $\geq 5\%$ PP by volume is represented in gold, with the x axis representing the proportion of PP, and the remainder of the volume consisting of shale minerals similar to non-PP rich shale. Carbonate with $> 5\%$ PP is represented in green, with observed textures marked alongside.

Table 1.1. Summary of PP morphologies observed in PP-rich shales around the Monteville spherule layer. Width corresponds to the shortest dimension and length corresponds to the longest dimension.

Pyrite shape	**Dimensions**	**Stratigraphic locations (cm)**
Horizontal layers	1-3 mm width, 10 mm length, may contain angular fractures with length 2-4 mm	110-145, 225-230, 235-240, 900
Vertical to subvertical sheets	1-3 mm width, 10-30 mm length	110-145, 295-300, 900
Cylinders (circular to oval cross section)	1-2 mm diameter (110-145 cm), $\geq$ 12 mm length and 3-4 mm diameter (250-255 cm), 3 mm diameter and 7 mm length (140 cm)	110-145, 250-255
Rounded to well-rounded spheres	1-5 mm (largest 7 x 5 mm at 235-240 cm)	110-150, 180-185, 225-230, 235-240, 500-510
Larger well-rounded spheres	2-6 mm diameter	225-230
Interconnected subrounded to subangular nodules	2-5 mm width, 15-40 mm length	145-150, 180-185, 915-925

1.4.2. Description of Facies.

1.4.2.1. *Shale.* The shale facies consist of interlaminated carbonaceous silty shale and siltstone (Figure 3). The thickness of individual beds ranges from a few millimeters to several centimeters. Two subfacies depend on the proportion of PP. Shale with $< 5\%$ PP by volume is referred to as "shale", and shale with 5-50% PP by volume is referred to as "pyrite-rich shale". Below 1030 m in the stratigraphic column, both shale and pyrite-rich shale tend to be a deep red color; however, some of these shales have a surface coating of tan to orange iron hydroxides. In contrast, shale above the pyritic zone (above 1030 m in the stratigraphic column is black in outcrop, pointing to the lower concentration of pyrite and highly reactive iron in the unweathered rock (Figure 1.3E).

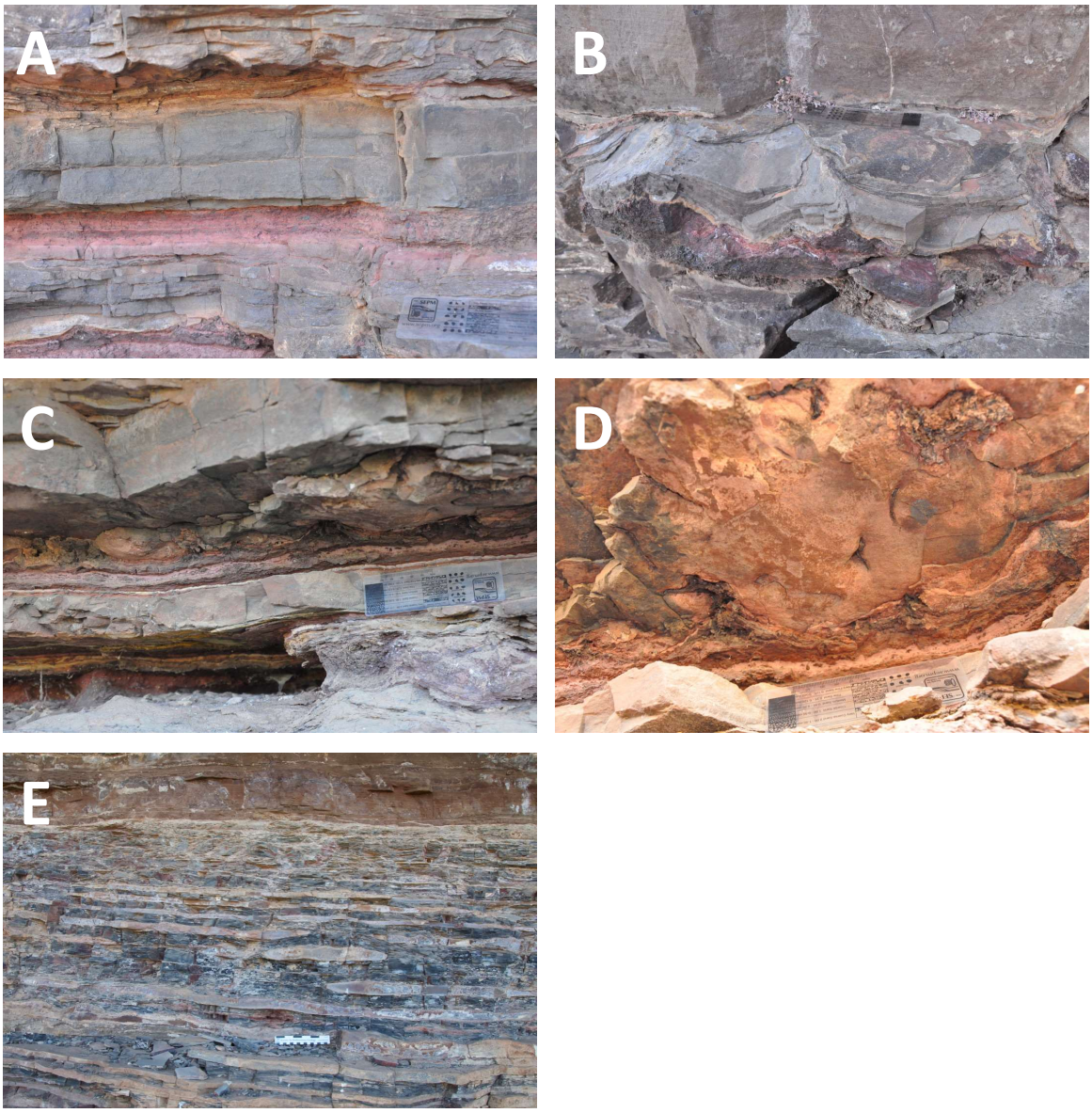

Figure 1.3. Caption on following page.

1.4.2.2. *Pyrite-Rich Shale.* Pyrite-rich shale is distinguishable from shale due to the presence of PP at $\geq 5\%$ of the bed by volume. PP in these shales ranges from isolated spheres, to disconnected laminae-confined spheres, to interconnected nodules, to fully connected horizontal layers. Interconnected nodules may form cylinders rather than layers. Beds of pyrite-rich shale that were ≥ 5 cm thick were logged in the stratigraphic column (Figure 1.2). Morphologies and abundance

Figure 1.3. Shale and pyrite-rich shale. **A:** Recessively-weathering PP-rich shale from 300 cm, below the base of the MSL. The bottommost PP-rich shale bed has peaks that have a higher concentration of PP than the underlying rock. The uppermost recessive-weathering bed consists of millimeter-scale shale and carbonate interbeds. The shale in these interbeds contains no visible PP nodules and appears more orange than the redder PP-rich shale. **B**: Peaks within a PP-rich shale between a massive carbonate bed below and an overlying laminated carbonate bed. The tops of the linear dewatering features can be observed trending into the rock face. Found at 900 cm, which is above the MSL. **C**: Pyrite-rich shale with sinusoidal dewatering features, found at 295 cm from the base of the measured section. These cuspate features are elongated perpendicular to the rock face (see 1.3D), with the crests aligned parallel to each other. These structures are interpreted to form from a combination of microbial growth processes and dewatering prior to lithification that deforms synsedimentary iron sulfide-rich layers. **D:** Underside of the rock overlying the sinusoidal dewatering features pictured in 1c. The dark shapes show how the crests create imprints in the overlying massive to laminated carbonate. **E:** Shale and laminated to massive carbonate beds and lenses above the euxinic interval. No PP is observed anywhere for at least 6 meters over the last observed PP-rich bed.

of PP nodules within these thicker beds is similar to those in thinner interbeds of shale between carbonate beds.

One feature of many pyrite-rich shales is the presence of cuspate to genticulate tented features, referred to as "peaks", separated by horizontal, flat-lying layers of PP with a thickness 1 mm or less. The peaks separated by ≈ 7 cm, and peaks are roughly 4 cm above the troughs. Under peaks, PP becomes more abundant, going from $\leq 10\%$ outside of peaks to $40-70\%$ under peaks. The PP sheets within peaks are sub-vertically to vertically oriented and thicken to $2-4$ mm. The thickest of these sheets are continuous for at least 4 cm, and shorter and thinner sheets may truncate against the base of the thickest sheet, which also forms the top of the peak.

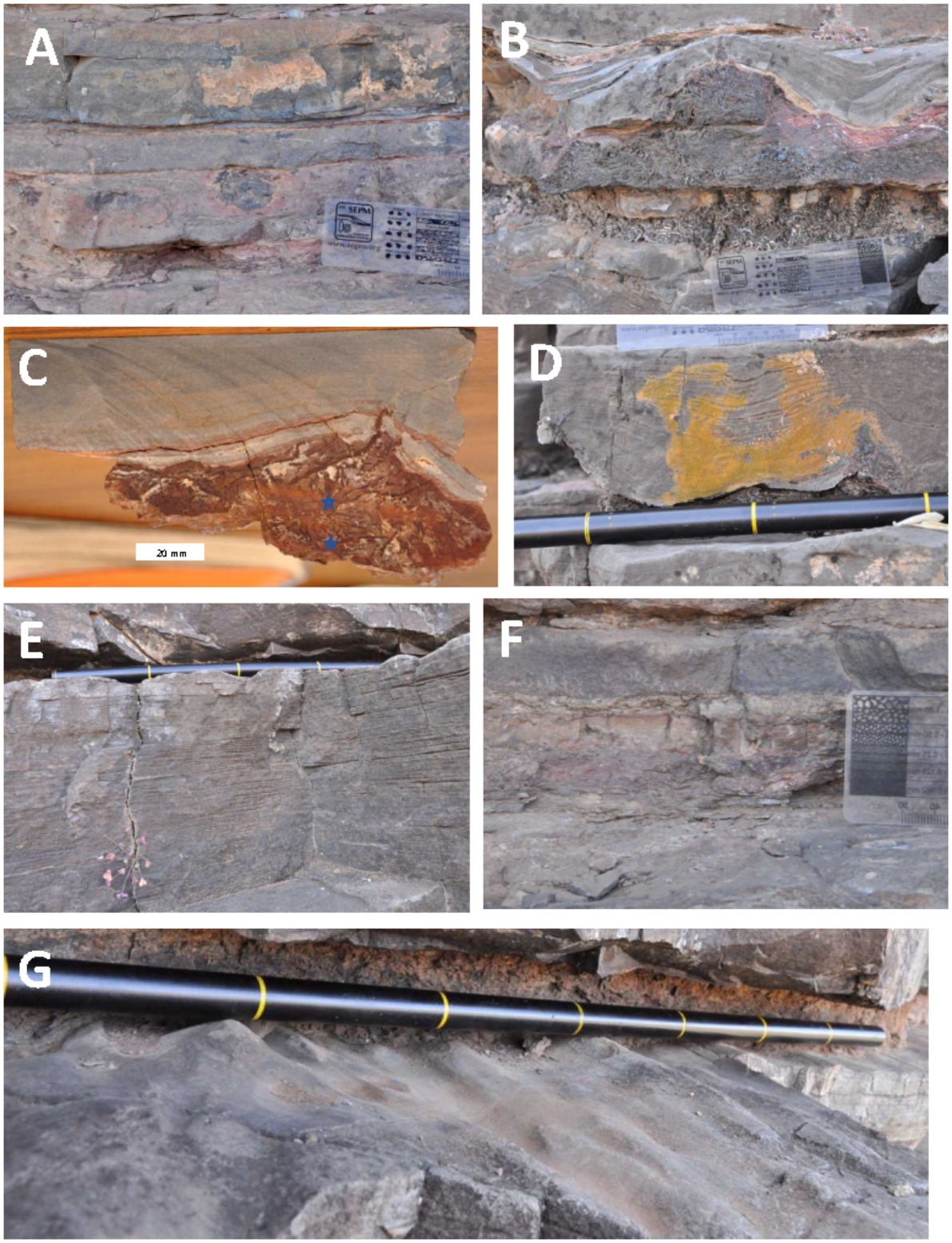
A
B
C
20 mm
D
E
F
G

Figure 1.3. Laminated to massive carbonate. A: Large (2 cm) rounded PP concretion within massive to laminated carbonate surrounded by thin (2-10 mm) thick beds of PP-rich shale. 2 cm diameter rounded PP bodies are loosely arranged in layers. The top of the large PP nodule is truncated by the overlying massive granular carbonate, indicating that the soft precursor of the lithified nodule formed prior to compaction and lithification. Found at 235 cm. B: Subhorizontal to subvertical sheets of PP underneath a dome with a peak at the top, from 915 cm in the stratigraphic column. These sheets are more subhorizontal coming out of the area directly underneath the point of the peak, becoming more vertical before intersecting the wall of the structure at a roughly perpendicular angle. The sheets are smoothly and continuously deformed, with no obvious brittle breakage seen on this face. C: Cut surface showing peaked structure within PP-rich shale. The center, thickest sheet is curled over on itself at the top, with no brittle deformation observed at the hairpin turn. Thinner sheets of PP grow outward from points, marked with stars. These points are no more than 1 cm away from the crest of the peak. The sheets radiating from the upper star truncate against the subhorizontal part of the center sheet. Deformation of the overlying planar laminated carbonate is observed. Euhedral, sparry calcite is found on the underside of thicker PP sheets, suggesting that it formed in the porosity under the PP sheets. Scale bar is 20 mm. D: Laminated carbonate overlaying the peaked structures in 2b. The right structure shows a 2 cm long and 3 mm width, vertically oriented sheet of pyrite. Thickness of the laminae in the bed immediately above the sinusoidal vertical structure is variable based on the topography of the vertical escape structures. The undulosing lamination is truncated at the top by a 1 cm layer of thinly, evenly laminated carbonate. E: Granular, rippled to planar laminated carbonate at 965 cm showing the mm-scale planar lamination, with occasional low-angle truncations indicating variable flow conditions. F: Laminated to massive carbonate at 505 cm showing rounded, isolated pyrite spheres, 1-5 mm in diameter, composing 10% of the rock by volume. G: The uppermost part of the planar laminated carbonate at 965 cm preserves symmetrical bedform tops below pyrite-rich shale.

1.4.2.3. *Laminated to massive carbonate.* Massive carbonate is dark gray in color and shows no evidence of bedding at < 1 cm scale in the field. The absence of lamination could be due to the extensive recrystallization of carbonate, which makes the identification of grain size difficult. These granular laminated beds grade into granular beds that contain mm-scale ripples with low angle truncations. The top of one of these beds has a wavy texture, with sub-parallel symmetric ridges. The sides of the ridges truncates an underlying horizontal bed (Figure 1.3E).

Massive carbonate can grade into finely laminated carbonate that consists of millimeter to sub-mm-scale laminations. These laminae have a crinkled texture and variable thickness over the topography in underlying layers, tending to be thinner above topographic highs (Figure 1.3B, D). These topographic highs are created by subvertical sheets of PP.

Laminated to massive carbonate with granular textures may have up to 10% PP by volume. PP is typically found as isolated spheroids 1-5 mm in diameter (ie, Figure 1.3F). Occasionally, these spheroids may be arranged along lamination planes (ie, Figure 1.3A). These layers of PP spheroids tend to be found near PP-rich shale. Rare large (2 cm length) nodules are truncated by

erosive surfaces at the bases of overlying granular carbonate layers. One such nodule, 40 mm in width, shows pointed to rounded protrusions on the upper surface (Figure 1.3A). This nodule may have begun to form at the sediment-water interface prior to lithification and may have continued to grow at the sediment-water interface after erosional removal of overlying sediment based on the protrusions and truncation.

The presence of erosive features such as symmetric wave ripples and low-angle truncations within granular carbonate beds suggests that lamination within coarser-bedded carbonates is primarily controlled by physical grain transport processes. The variable presence of PP within some laminated to massive carbonate beds, its formation along distinct layers, and its tendency to be found near PP-rich shales suggests that carbonate precipitated under fluctuating sulfide concentrations.

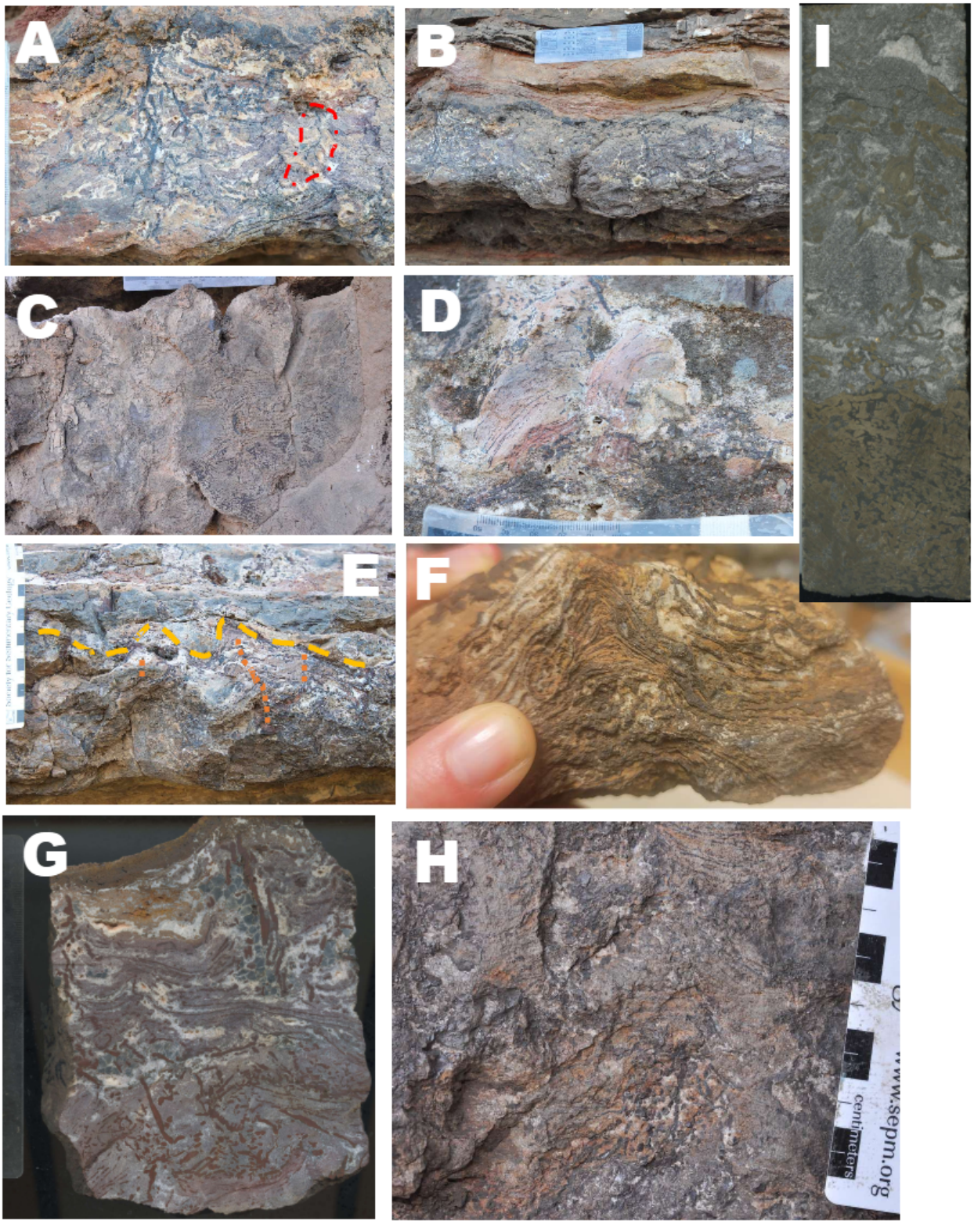
A
B
I
C
D
E
F
G
H
www.sepm.org
centimeters

Figure 1.3. Microbial carbonate. A: Bed of microbial carbonate at 280 cm. Vertical to sub-vertical coalescing sheets of PP below the impact, which spans the entire thickness of the 10 cm bed. The thickest sheet is 3 mm wide. A thinner (1 mm), shorter (40 mm), and discontinuous vertical to subvertical sheet of PP is outlined in red. Fewer sheets of PP join this structure when compared to the thicker structure to the left. The thinnest PP consists of fine (¡ 1 mm, horizontal to sub-horizontal, concave-upward laminations that are found in between the subvertical to vertical sheets. B: Broader view of microbial carbonate bed at 280 cm, showing truncated tops of the vertically branching PP. The contact with the underlying red PP-rich shale is wavy. At the very top of the bed is a thick (1 cm) layer of PP with topographic highs above the vertically oriented PP. The overlying rock is reddish laminated PP-poor shale. C: Continuous, sigmoidal darker-colored laminae (1mm thick) separated 2 mm by lighter micritic carbonate matrix. These laminae are more resistant to weathering and are interpreted as having a chert mineralogy. Seen at 510 to 540 cm. PP (orange outline) occurs as 2 mm-wide nodules with laminated morphology (center-right). These nodules occur along subvertically to subhorizontally aligned planes within the rock. D: Laminated thin PP within carbonate in the MSL, showing soft sediment deformation of a cohesive block of carbonate. This clast, which has a similar texture to 5C in terms of mineralogy as well as thickness and spacing of PP laminae, would have necessarily been initially formed before the MSL. E: Stromatolitic microbially influenced carbonate .at 150 m The tops of stromatolite columns are cuspate to genticulate at the top. The layer outlined with dashed yellow is continuous over a meter of outcrop before it is covered by surface weathering products. Thinly laminated PP follows concave-up geometry and is found in the lows between peaks. Branching intermediate to thick PP is outlined in the orange dashed line and is frequently found below topographic highs. F: Rolled mat next to conical structure pyrite-carbonate stromatolite, indicating that laminae within stromatolites was cohesive to a degree that suggests a biological influence. G: Cut surface of microbialite carbonate, showing both coalescing sheets of pyrite and concave-up laminated pyrite. H: Microbially influenced carbonate, showing thin laminated PP (top) and thicker coalescing PP sheets. Colorless, sparry calcite is observed between the sheets of coalescing PP but not the thin laminated PP. From the same layer as 5C. I: Core sample GKF1 1419.70. Pyrite-rich shale overlain by microbialite carbonate containing vertically oriented sheets of pyrite. White calcite forms to the side and underneath sheets of pyrite.

1.4.2.4. *Microbialite carbonate and pyrite.* Microbialite facies include stromatolites and very finely planar laminated carbonates with variable concentrations of pyrite. Stromatolitic and associated planar lamination is 1 mm thick or less. The spacing between the laminations is highly variable, ranging from $<$ 1 mm to 3 mm. Some laminae are rolled up and contorted, requiring a cohesive rheology, consistent with a microbial influence on this texture (*Simonson and Carney*, 1999; *Sumner*, 1997). Thus, laminae are interpreted to represent microbial mats. Stromatolite geometry ranges from columnar to domed to genticulate, with the majority of stromatolites having domed tops. Columns and domes consist of at least two size classes. The larger domes to columns are $20-25$ cm in diameter with 5-7 cm of synoptic relief and lateral spacing of $5-20$ cm. Smaller domes grew off of the larger ones and are $2-5$ cm in diameter, with $2-5$ cm of synoptic relief and lateral spacing of $1.5-5$ cm. Many of the smaller size class of stromatolites grew at a single horizon

marked by a single continuous pyrite layer, roughly 3 mm thick was traced from stromatolite to stromatolite over a meter of bed length.

Carbonate is the dominant mineral in this rock type, representing $50 - 80\%$ of the rock by volume. This carbonate may be either microsparitic with a dull luster, typically with an orange to pink color, or euhedral and colorless. Euhedral carbonate tends to be found parallel and perpendicular to bedding. Bladed crystals of euhedral, sparry calcite grew inward from the walls of voids within the cores of stromatolites. This calcite cuts through pyrite nodules. Vertically-oriented bodies of coarsely crystalline carbonate are oriented perpendicular to bedding, alongside vertical and below sub-vertical pyrite features.

Thin pyrite laminations are present in all microbially influenced carbonate. These thin pyrite laminae tend to be subhorizontally oriented; however, some steepen to a subvertical arrangement, particularly on the edges of laminated stromatolites or microbialites. Occasionally, $1 - 2$ mm thick pyrite sheets are arranged nearly vertically with a geometry that suggests upward branching. Typically, vertical to subvertically oriented pyrite sheets thicken upward. Some microbialite beds contain particularly thick, coalescing, subvertical to vertically oriented pyrite sheets. These sheets can be as thick as 5 mm but are more typically 2 mm thick. These sheets may extend the entire height of the beds, at least 10 cm. Thicker vertically oriented pyrite tends to be located below the crests of stromatolitic highs and can occasionally protrude above the top of a heavily pyritized layer within a stromatolite. The geometry associated with these protrusions is consistent with mechanical fracturing, and they are interpreted as compaction features, similar to the sigmoidal dewatering structures seen in pyrite-rich shale.

1.4.2.5. *Impact-Associated Beds.* The impact associated beds consist of a lower breccia overlain by symmetrically rippled grainstone. The impact breccia consists of clasts up to 1.8 m in diameter (*Hassler and Simonson*, 2001) with a fine-grained matrix containing abundant impact spherules, some of which have been converted to pyrite (*Kohl et al.*, 2006). PP is found within carbonate clasts with similar morphology to PP in microbialite carbonate (Figure 1.3D). The pyrite in laminated carbonate is softly and continuously deformed. Coalescing pyrite 7 x 3 mm is also observed and shows both soft and brittle deformation. The matrix consists of up to 50% PP or pyrite by volume. Most PP consists of 2 to 5 mm rounded to subrounded nodular spheroids and sheets. These

features may show evidence of synsedimentary brittle deformation, with angular breakage infilled with microsparitic carbonate. The PP textures in the matrix, as well as the deformation of PP laminae in some breccia clasts suggests that PP was present in the sediments prior to the impact and that the rheology of the carbonate and pyrite precursor was soft during the impact.

The layer overlying the impact breccia consists of 15 cm of symmetric-rippled carbonate grainstone. This bed has been previously interpreted as being deposited from oscillating impact-induced tsunami waves (*Hassler et al.*, 2000). No PP is observed within this bed, consistent with *Hassler and Simonson* (2001).

1.4.3. Stratigraphic Trends. The proportion of shale generally decreases up section. The topmost bed of PP-rich carbonate is the last bed that contains PP for at least 6 meters. The beds above the measured stratigraphic column consist of interbedded shales and lenses of carbonate (Figure 1.3E). There are no significant facies differences before versus after the impact interval.

1.5. Discussion

1.5.1. Pre-Compaction Precipitation of Iron Sulfides. Sheets of PP in outcrop and pyrite in cores show evidence of soft sediment deformation along with brittle deformation within the impact breccia. The precursor iron sulfide minerals are inferred to have had a softly deformable rheology prior to complete lithification as pyrite. This phase may form due to concentration of iron and sulfide within soft, organic-rich microbial layers. Complete hardening of iron sulfides into pyrite layers requires additional sulfide, as described in Chapter 2.

Pyrite precipitated prior to compaction and lithification of the sediments both before and after the 2.63 Ga giant impact. This can be readily observed from the brittle deformation of pyrite nodules, spheres, and laminae directly next to impact spherules. This fracturing must have occurred near the time of emplacement of the spherules. Microbially-influenced carbonate is limited to the stratigraphic interval immediately preceding and following the MSL, meaning that the temporal interval for this mineralization to occur is limited. Additionally, the deformation of laminated carbonate by underlying sigmoidal escape structures similarly points to early mineralization of an iron-sulfide phase.

Extensive pyrite precipitation requires the presence of both reduced iron and sulfide in a localized area, which may explain the paleogeographic limits of elevated pyrite at about 2.63 Ga. For example, abundant evidence of synsedimentary pyrite deposition is found along the shelf-slope transition, but pyrite is mostly absent during this interval at the Pering Mine locality, which was higher on the shelf in a carbonate platform (*Simonson et al.*, 2018). The presence of deeper water abundant, synsedimentary pyrite requires the presence of both iron and sulfide in the environment near the sediment-water interface. The Monteville Formation at Monteville Farm was likely a slope environment where different fluids mix, or rapid environmental elemental cycling allowed for the presence of different reduced species at different times.

1.5.2. Persistence of Microbial Morphology Following the Large Impact. The similarity between pre- and post-impact microbially influenced facies includes the persistence of the thinly laminated pyrite within micritic carbonate. This texture is seen throughout the euxinic interval and suggests similar patterning of microbial mats through the impact. The presence of branching pyrite above and below the impact suggests similar complex community dynamics pre- and post-impact.

The textural and depositional similarities pre- and post-impact suggest that environmental gradients and supply of iron and sulfide were similar before and after the disruption associated with the impact. Larger-scale environmental forces such as subaerial volcanism and oxidative weathering driving the high concentration on sulfide in the basin at this time may have been responsible for the mineralogy observed in this interval.

1.5.3. Other Large Impacts and the Sulfur Cycle. The best studied large meteorite impact is the Chixulub impact. The K-T impact had a particularly strong effect on the sulfur cycle, as the target material was an evaporitic gypsum basin *Ishida et al.* (2007); *Pierazzo et al.* (2003). The impact aerosolized the sulfate, causing acid rain and shielding sunlight, creating a global primary productivity and climatic crisis.

In contrast, the target material for the 2.63 Ga giant impact was likely oceanic crust. This impact could have created a long-lasting hydrothermal system which may have affected the supply of reduced sulfur and iron to the Archean oceans, possibly related to the deposition of the Marra

Mamba iron formation (*Glikson*, 2006, 2010). However, this hydrothermal system would have been subaqueous and therefore would not have had the dramatic climatic effects of the K-T impact. However, these long-lasting hydrothermal systems may change the chemistry of the deep ocean when it was more reduced and therefore had a longer residence time for reduced iron (*Glikson*, 2006).

The absence of any long-lasting changes in sedimentology and pyrite content of sediments suggests that this impact did not have a significant impact on the climate or sulfur cycle. Elevated sulfide contents in sediments predated the impact, and return after a 60 cm hiatus of significant sulfide content in shales and carbonates following the top of the wave-rippled layer at the top of the MSL. The absence of pyrite in this background facies may suggest a short-term disruption of the processes that caused euxinia. The correlation of this absence with the impact horizon suggests a possible role of the impact in changing the style of chemical sedimentation; further comparison of stratigraphy at different localities and between basins across the impact horizon would help elucidate the scale and timing of a possible disruption of the sulfur cycle.

1.6. Conclusion

No change in lithology or pyrite morphology and abundance was observed above and below the MSL, excepting a 60 cm hiatus above the top of a bed of tsunami-rippled carbonate grainstone. These results suggest that similar mechanisms causing high iron sulfide concentrations and precipitation must have operated similarly both before and after the impact. Although the MSL had a significant effect on the immediate sedimentology, causing deposition of large breccia clasts, there was no long-term change in sedimentation. Similar amounts of shale and carbonate were deposited above and below the impact. Additionally, the PP-free interval above the euxinic interval contains similar lithology to the euxinic interval except that it lacks PP. The combination of these results suggests that carbonate and shale deposition predominated for the deposition of the Monteville euxinic interval, and that transport of iron and sulfide ions was mediated by large-scale processes that were not affected by the impact. Further work is required to characterize the disappearance of the euxinic interval above the impact.

CHAPTER 2

Petrography of Pyrite in the 2.63 Gya Euxinic Interval

2.1. Abstract

Pyrite morphology can reveal how pyrite formed. The relative timing of formation of different textures of pyrite can be used to infer when during sedimentation and diagenesis a particular piece of pyrite formed. Such textural relationships have been used to reconstruct geobiological (*Meyer et al.*, 2017) and geochemical (*Izon et al.*, 2022) processes in the sulfur cycle in Archean-age rocks. The use of in situ analyses of sedimentary pyrite can be contrasted with whole-rock geochemical analyses which have been used to investigate long-term trends in trace element and redox conditions. However, late-stage diagenesis, metamorphism, and hydrothermal activity can affect pyrite geochemical signatures. An understanding of pyrite formation processes is essential for linking redox changes in the Neoarchean across continents (*Cui et al.*, 2018; *Partridge et al.*, 2008). This chapter illustrates a variety of pyrite textures observed in cores spanning the 2.65-2.63 Ga Jeerinah Formation, Western Australia, through a euxinic interval. Where possible, models for formation mechanisms are discussed. This work provides key constraints on the formation of various pyrite phases and helps refine prior interpretation of geochemical signatures through the euxinic interval.

2.2. Introduction

2.2.1. Pyrite as a geochemical indicator of Archean conditions. Synsedimentary pyrite can provide an important record of biogeochemical process affecting the sulfur cycle, including microbial metabolisms, weathering, volcanic outgassing, and atmospheric ozone (*Farquhar et al.*, 2013; *Havig et al.*, 2017; *Izon et al.*, 2015; *Johnston*, 2011; *Schieber*, 2002b). However, pyrite also forms during burial and metamorphism, which can complicate the interpretation of synsedimentary processes. For example, significant discrepancies exist between geochemical interpretations of disseminated versus large aggregates of pyrite from Neoarchean sedimentary rocks (*Anbar et al.*

(2007) versus *Slotznick et al.* (2022)). Disseminated pyrite-rich rocks have been interpreted to contain evidence of "whiffs" of oxygen in 2.5 Ga rocks from South Africa and Western Australia (*Anbar et al.*, 2007; *Duan et al.*, 2010; *Kendall et al.*, 2010; *Ostrander et al.*, 2019, 2020; *Wille et al.*, 2007). These "whiffs" of oxidative weathering are inferred from the presence of elevated concentrations of molybdenum in black, sulfide-rich shales. Molybdenum dissolves under oxidative conditions and precipitates under sulfidic conditions. Therefore, the presence of high concentrations of molybdenum has been inferred to represent transient amounts of oxidative weathering, perhaps in environments analogous to the stromatolites with oxygen-containing bubbles (*Wilmeth et al.*, 2019, 2022).

However, work on larger pyrite features has called into question whether the elevated molybdenum seen in these rocks is due to a primary, synsedimentary signal, or represents later mobilization of molybdenum-rich fluids (*Slotznick et al.*, 2022). These authors looked at a nodule of pyrite that was near disseminated pyrite and found that the molybdenum was localized within veins that cross-cut the shale and nodule. This result was taken to indicate that molybdenum became emplaced in the Mt. McRae Shale only after significant burial and late-stage fluid flow, contradicting the interpretation that the molybdenum enrichment indicates synsedimentary oxidative weathering. Slotznick et al. demonstrated the importance of petrographic relationships for putting geochemical analyses into better context, although their study was too limited to contradict all evidence for synsedimentary molybdenum enrichment in that interval.

In addition, some pyritic intervals lack molybdenum enrichment, raising questions about alternative sulfur sources. One of these intervals is the 2.63 Ga euxinic event in the Kaapvaal and Pilbara cratons. Rocks from this interval been proposed as recording an even earlier interval of enhanced oxidative weathering even though the geochemical signatures are different from the younger "whiff" interval (*Ostrander et al.*, 2021). However, the petrogenesis of pyrite in the $\sim$ 2.63 Ga interval is particularly complex, with evidence for the precipitation of seafloor pyrite nodules (Chapter 3) as well as late diagenetic veins. This chapter provides key constraints on the formation of various pyrite phases to help place geochemical signatures into context.

2.2.2. Petrography and Petrogenesis of Pyrite: Background. The relative timing and rates of generations of pyrite precipitation can be evaluated in the context of detailed petrographic

analysis. Cross-cutting relationships between depositional laminae, sulfide minerals, and veins tell a petrogenetic story that can be used to distinguish depositional from diagenetic and metasomatic processes. Cross-cutting relationships among generations of pyrite may reveal relative petrogenetic timing whereas crystal textures provide insights into different precipitation mechanisms, including kinetics of pyrite nucleation and crystal growth.

2.2.2.1. *Kinetics of Pyrite Precipitation.* Pyrite kinetics can be controlled either by nucleation or growth rate. The nucleation of pyrite is extremely slow and may not occur directly at low temperatures (*Schoonen and Barnes*, 1991a). Pyrite growth may occur more rapidly on seed nuclei, which may be pyrite or a monosulfide precursor such as mackinawite (*Schoonen and Barnes*, 1991a). Pyrite growth in the presence of seed nuclei occurs spontaneously above a critical saturation state (Ω), which is defined as the supersaturation above which a phase will spontaneously precipitate. Ω was measured at $5.7 * 10^{14}$ for the reaction $FeS_{2p} \longleftrightarrow Fe^{2+} + {S_2}^{-2}$ (*G. Harmandas et al.*, 1998; *Rickard*, 2012c). However, the saturation state for spontaneous nucleation should be reexamined considering that ${S_2}^{-2}$ does not exist in aqueous solution (*May et al.*, 2018), and other sulfide phases can also precipitate pyrite, such as disulfide (H_2S_2) and polysulfide (H_2S_n) (*Rickard*, 2012c; *Schoonen and Barnes*, 1991a,b). These species are present at higher activities with higher total concentrations of sulfur, lower pH, and Eh intermediate between the stability fields of sulfide and sulfate (*Rickard*, 2012a).

2.2.2.2. *Metastable Iron Sulfide Minerals.* Metastable iron sulfide minerals can precipitate in conditions different from those that favor pyrite precipitation. Mackinawite precipitation occurs rapidly when its Ω is even slightly exceeded (*Rickard*, 2012a). The activities of iron and sulfur where this occurs are very close to the activities of iron and sulfur where pyrite precipitation begins (*Rickard*, 2012c). Thus, mackinawite crystals may potentially provide seed nuclei for pyrite nucleation and growth. Even though mackinawite may form first, it rapidly converts to other more stable iron sulfides so it is not preserved in ancient rocks.

Marcasite (orthorhombic FeS_2) is the dominant iron sulfide to precipitate at pH < 5, T < 240°C, and lasts over geologic timescales if it is not heated above ca. 160°C for longer than about a million years (*Murowchick*, 1992); otherwise, it reverts to the more stable pyrite. Pyrite with marcasite ancestry can retain the acicular habit of the parent marcasite (*Schieber*, 2011); however, pyrite

can also precipitate with an acicular habit (*Rickard*, 2012c). A better indicator of a marcasite precursor to pyrite is remnant anisotropy (*Bannister*, 1932; *Murowchick*, 1992) that remains after alkaline polishing (*Libowitzky*, 1994). Marcasite to pyrite conversion results in a 2.6% volume reduction, which creates numerous small pores along grain-twin boundaries (*Murowchick*, 1992). Finally, because marcasite only precipitates at a pH low enough to dissolve pyrite and carbonate, dissolved grains of pyrite and carbonate can provide further evidence of conditions that could have precipitated marcasite (*Schieber*, 2007, 2011). Therefore, the presence of marcasite or pyrite formed from marcasite inversion (i.e., *Schieber* (2002a,b, 2007); *Schieber and Riciputi* (2005)) is indicative of acidic conditions saturated in marcasite.

Pyrrhotite is a non-stoichiometric compound ($Fe_{(1-x)}S$, where $x > 0.2$) and a monoclinic or hexagonal structure (*Rickard*, 2012b). When pyrrhotite reverts to pyrite, it undergoes a 30.4% decrease in volume and typically dissolves, leaving voids that can be filled with other minerals (*Murowchick*, 1992; *Qian et al.*, 2011). Because pyrrhotite must dissolve to reprecipitate as pyrite, pyrite after pyrrhotite has no preferred orientation (*Murowchick*, 1992). However, if pyrrhoite goes through a marcasite intermediate before being converted to pyrite, it may have domains that have a preferred orientation representing preserved anisotropy from the marcasite crystal structure (*Qian et al.*, 2011).

2.3. Geologic Context and Methods

The Pilbara Craton is a segment of Paleoarchean continental crust in northwestern Western Australia (Chapter 3 Figure **??**A, *Hickman* (2012)). The 2.78—2.63 Ga Fortescue Group formed on the Pilbara Craton and is a predominantly volcanic succession, consisting mainly of a basaltic large igneous province. Deposition along a passive margin at the top of the Fortescue Group and the overlying Hamersley Group resulted in the simultaneous deposition of the Carawine Formation (a shallow carbonate platform) and the Jeerinah Formation (a deep water shale). A meteorite impact at 2.63 Ga provides an instantaneous marker bed that stretches across these depositional environments (Chapter 1, *Simonson et al.* (2009a,b).

The stratigraphy surrounding the meteorite impact has been previously studied (*Czaja et al.*, 2010; *Eigenbrode and Freeman*, 2006; *French et al.*, 2015; *Knoll and Beukes*, 2009; *Simonson et al.*,

2009b) and represents a platform-basin transition below storm wave base with abundant microturbidites. Around the time of this meteorite impact, both the Carawine and Jeerinah formations contain extensive pyrite deposition that has been proposed to record an early euxinic interval (*Koehler et al.*, 2018; *Lyons et al.*, 2009; *Olson et al.*, 2019; *Ostrander et al.*, 2021). However, the source of sulfur to the basin at this time has not been conclusively identified. It has been proposed that the source of sulfur is due to an increase in oxidative weathering on land (*Koehler et al.*, 2018; *Ostrander et al.*, 2019, 2021, 2020). Another hypothesis is that the sulfur is due to an increase in volcanism (*Olson et al.*, 2019). These scenarios are discussed in more detail in Chapter 1.

2.3.1. Cores. Cores AIDP-2 and AIDP-3 were drilled through the Fortescue and Hamersley Groups, specifically targeting organic-rich sedimentary rocks, by the Agouron Drilling Project (*French et al.*, 2015). Core AIDP-2 was collected less than 1 km from the older RHDH2A core and contains the same stratigraphy which has been previously studied (*Eigenbrode and Freeman*, 2006; *Gregory et al.*, 2019, 2015; *Ono et al.*, 2003; *Williford et al.*, 2016). Pyrite has diverse phases that precipitated at different times. Prior work has not characterized the petrography of pyrite in this interval or connected pyrite precipitation to regional processes. Our work shows that some pyrite precipitated directly on the seafloor, identifying a texture that is likely to preserve the geochemistry of the seawater it precipitated from (Chapter 3).

A prior study identified an enrichment in molybdenum in the shallower water AIDP-2 and to a lesser degree in AIDP-3 (Figures 2.0 and 2.0, *Olson et al.* (2019)). Additional iron speciation data in the same study identified periods of euxinic and ferruginous conditions. For AIDP2, the shales between 400 and 380 m have modest enrichments reactive Fe primarily bound in carbonate rather than pyrite. This geochemistry is consistent with a ferruginous ocean. Between 380 and 340 m, the amount of highly reactive Fe increases, and that iron is predominately found within pyrite. This increase in pyrite is accompanied with an increase in molybdenum and organic carbon. Above 340 m, pyrite content drops, and iron is predominately found within carbonate. For ADIP3, pyrite enrichment is observed in shales between 160 and 120 m. This pyrite enrichment is accompanied by an increase in molybdenum but not organic carbon. Shales between 120 and 105 m are enriched in iron-rich carbonates, consistent with ferruginous conditions. A larger magnitude of pyrite enrichment is observed between 105 and 65 m, which is not associated with an increase in molybdenum

but is associated with a modest enrichment in organic carbon. The lower euxinic interval in AIDP3 may be equivalent to the euxinic interval in AIDP2; however, correlations between the shales in these cores has been difficult.

2.3.2. Samples. Samples used in this study, as well as their depths relative to the geochemical zones described by (*Olson et al.*, 2019), are shown in Figures 2.0 and 2.0.

2.3.3. Methods. Cores were collected using methods described in *French et al.* (2015) and were split in half, with one half of each shipped to the United States (US). The US portions of the cores was logged and sampled by D. Sumner to obtain representative petrographic textures for pyrite within euxinic intervals. Thin sections were cut to 30 and 100 µm and polished with Buehler MicroPolish^{TM} Alumina 0.3 µm, which has a basic pH. Textures representing possible sea floor pyrite nodules were identified based on sample inspection at the slide scale and with reflected light petrography. Large mosaic images were collected in a grid using a Nikon SMZ25 with an automated stage and single-point coaxial reflected light illumination. The focus was adjusted manually every five frames since reflected light has only a single plane of focus. Large mosaics were stitched with the Nikon Advanced Research Best Path algorithm. Pairwise images were stitched with the ImageJ Stitcher program (*Preibisch et al.*, 2009).

Element maps of selected regions of interest were collected with the Hitachi SU 3500 VP-SEM with a Oxford Instruments X-Max^{N} 150 mm^2 silicon drift energy dispersive spectroscopy system at Jet Propulsion Laboratory's Astrobiogeochemistry Laboratory. Energy-Dispersive Spectroscopy (EDS) maps were generated on this system, as well as with the Cameca SX-100 electron microprobe at UC Davis Earth and Planetary Sciences.

2.4. Petrographic Textures

The analyzed thin sections showed numerous petrographic textures; seven of the textures are described here. Pyrite crystals ranged from < 5 µm to mm-scale in size and anhedral to euhedral in habit.

2.4.1. Inclusion-rich Pyrite. Inclusion-rich pyrite forms numerous features ranging in from thin laminae ($\sim$ 100 µm thick) to large nodules and concretions ($>$ 27 mm by 100–1000 µm in cross

section). Inclusions range from < 1 to ~ 20 µm in size and may contain calcite, kerogen, or shale minerals. The boundary between the inclusions and pyrite is highly irregular, suggesting that the crystals are anhedral; however, distinct boundaries between pyrite crystals leading to identification of crystal size is difficult to determine. Under EDS, it appears mottled, with the mottling being created from regions of different electron density $\sim 5 - 10$ µm in diameter (Figure 2.0C).

2.4.2. Euhedral, Inclusion-poor Pyrite. Inclusion-poor pyrite commonly coats the edges of pyrite nodules and concretions in addition to growing into pores and veins filled with calcite. Isolated crystals of inclusion-rich pyrite may also be found disseminated within shale. Where inclusion-poor pyrite crystals has completely replaced a pre-existing texture, compromise crystal boundaries are typically planar but do not follow crystal boundaries. One such texture consists of bean-shaped bodies of lighter, inclusion-poor pyrite outlined by kerogen and shale inclusions.

The size range of inclusion-poor pyrite is quite large, ranging from ~ 5 µm to 500 µm. Inclusion-poor pyrite is typically euhedral, and crystal points are often visible. It has variable color in reflected light but is typically lighter-colored than co-existing inclusion-rich pyrite.

2.4.3. Feather Pyrite. Feather pyrite has patterns of inclusions that define a central stalk and radiating regions that define a feather-like pattern (Figure 2.0A). Central stalks ~ 20 to 50 µm thick are composed of inclusion-poor pyrite and extend in all directions relative to the surrounding laminations The tops of stalks often have points that extend into the surrounding laminations. Additional pyrite grew subperpendicular to the central stalks and consists of thin (~ 15 µm thick) bands of inclusion-poor pyrite separated by subparallel lines of inclusions. Feather pyrite is isotropic under crossed polars (Figure 2.0B).

2.4.4. Blade Pyrite. Blade pyrite consists of fans of pyrite crystals extending upward from a point or a parabola-like base. The fans can be up to 1000 µm tall and 200 µm wide at the top. The tops of the fans are parallel to the laminated pyrite on the top of the pyrite body. Each fan is composed of a single pyrite domain that is vertically elongated. These domains contain some ~ 10 µm inclusions, but more are present at the boundaries between fans. Blade pyrite shows a red-green anisotropy under crossed polars in reflected light. Under EDS, the fans are a similar electron density within a fan, with slight variations between different fans.

2.4.5. Small Isolated to Aggregated Pyrite Crystals. Small (< 10 µm) disseminated pyrite crystals have several petrographic characteristics (Figure 2.1). They are commonly either equant and euhedral or elongate and anhedral. Euhedral crystals usually lack inclusions whereas anhedral ones often contain inclusions. Both textures can be present adjacent to each other (Figure 2.1G). In one case, 5 µm equant, euhedral crystals are present in a calcite-dominated vein (Figure 2.4E). Some of these crystals contain kerogen inclusions in their cores.

Some larger disseminated pyrite aggregates consist of a rim of pyrite, $5 - 20$ µm thick, surrounding $5 - 50$ µm calcite cores (Figure 2.2A, B). The rim consists of < 1 µm diameter crystals of pyrite. The outside edge of the pyrite rim is continuous and may be straight sided, suggesting that the small-grained pyrite replaced a euhedral crystal. The edges of pyrite on the inside of the rim is less well defined.

Similar pyrite crystals also aggregate to form thin layers and small concretions of pyrite. These bodies are composed of a mix of euhedral to anhedral crystals with compromise crystal boundaries where crystals grew into each other. In many cases, areas with small, isolated crystals grade into areas with larger, intergrown crystals (Figure 2.3). These then grade into areas of inclusion-rich or euhedral, inclusion-poor pyrite (Figure 2.2).

2.4.6. Sphalerite and Chalcopyrite. Sphalerite and chalcopyrite may be found associated with pyrite and calcite in veins, or as isolated crystals within shale. When found in veins, chalcopyrite and sphalerite tends to be subhedral to euhedral and may be as large as 200 µm in diameter, although is more typically around 50 µm. These two minerals tend to co-occur and intergrow with each other. Sphalerite is occasionally found as small ($5 - 20$ µm) subhedral crystals within shale.

2.4.7. Calcite Textures. Calcite is present in veins, shelter porosity, and surrounded by pyrite. The calcite cement within the vein consists of blocky, euhedral, equant crystals of calcite, $100 - 500$ µm in diameter. There is no trend in crystal size relative to the margins of the vein. Calcite cement in shelter porosity under pyrite growths (see Chapter 3) is typically composed of 10|50 µm crystals, again with no size trends relative to the margins of the original pores. Calcite rimmed by pyrite consists of single crystals $5 - 50$ µm in size. In some cases, calcite rimmed by

pyrite forms bean-shaped inclusions within concretions. They consist of $5 - 150$ µm long crystals with their boundaries commonly defined by kerogen and shale inclusions.

2.5. Petrographic Relationships

Petrographic textures contain various crosscutting relationships which demonstrate that pyrite precipitated during multiple intervals ranging from on the seafloor to after lithification.

2.5.1. Disseminated Pyrite in Sediment. The matrix for disseminated pyrite consists of calcite and silica cements and grains (Figure 2.1A) as well as clay minerals (Figure 2.1B). Even when the crystals are sparse, there is often a mix of anhedral and euhedral forms. In addition, disseminated pyrite is often found in higher concentrations in specific laminae, which are visible at both high magnification and at the thin section scale (Figure 2.1). These fine bands of disseminated pyrite likely represent small variations in sedimentation rate or composition.

Interpretation: The diversity of petrographic textures suggests that disseminated pyrite formed at multiple times during sedimentation, diagenesis and metamorphism, even within the same sample.

2.5.2. Seafloor Nodule Formation. Pyrite nodules are elongate parallel to sedimentary layering and can be 0.5 to more than 27 mm wide. Some expand outward from a narrower base to a wider top, while others span the whole core width. They tend to have bulbous tops and flatter bottoms, making them morphologically complex in three dimensions. Shale and thin carbonate turbidites lap onto the nodules, demonstrating relief on the seafloor over the nodules. In addition, overhanging pyrite growths produced shelter porosity later filled with calcite. The petrographic textures at the tops of the nodules are sometimes laminated and columnar in contrast to euhedral crystal forms at the bases of nodules, demonstrating different growth conditions upward versus downward.

Interpretation: Pyrite nodules are interpreted to precipitate on the seafloor in a manner analogous to precipitation of polymetallic manganese nodules (Chapter 3). In order for iron sulfide minerals to precipitate in such large quantities at the sediment-water interface, unique iron and sulfur cycling during this interval is required. The inferred high concentration of sulfur in seawater

required to form these nodules would have affected the precipitation of other textures described in this chapter.

2.5.3. Pyrrhotite Recrystallization to Pyrite. Several petrographic textures suggest that pyrrhotite prior to sediment compaction and later recrystallized into pyrite. Specifically, < 100 µm diameter rim pyrite surrounds calcite crystals, sometimes forming discontinuous layers visible at lower magnifications (ie, Figure 2.1B). These rims consist of inclusion-rich pyrite which is confided to $50 - 200$ µm regions with polyhedral borders.

Rim pyrite around calcite is also seen at a millimeter scale, for example, in sample AIDP3 132.98 (Figure 2.2F, G). A 0 to $\sim$ 1300 µm thick pyrite layer is surrounded by shale and disseminated pyrite. At the core of the pyrite layer are 200–500 µm crystals of calcite, which are rimmed by $\sim$ 100 µm thick coatings of subhedral pyrite. The pyrite closest to the calcite crystals tends to have fewer inclusions than the pyrite that borders the shale.

Another large pyrite feature also is partially composed of rim pyrite. It is $\sim$ 2 mm wide and 1 mm tall, and the surrounding laminae are deformed above the top and bottom of the thickest part of the pyrite body. It is composed of inclusion-rich pyrite that is confined to $50-200$ µm polyhedral regions, which is the same shape and size as rim pyrite in the surrounding shale laminae. This inclusion-rich pyrite has overgrowths of euhedral, inclusion-poor pyrite. Unlike the pyrite in the surrounding shale laminae, the pyrite rims do not have cores of calcite at the center. The bottom of this pyrite body has the closest packing of rim pyrite observed in this study.

Interpretation: Rim pyrite is interpreted to represent pyrite that formed as pyrrhotite dissolved, because the conversion of pyrrhotite to pyrite involves a decrease in the unit cell volume by 30.4% (*Murowchick*, 1992). This transformation has been experimentally shown to result in textures like those documented here (*Qian et al.*, 2011).

Compaction around pyrite growths with rim pyrite textures suggests that the original pyrrhotite formed early in diagenesis, followed by recrystallization to rim pyrite and overgrowth by inclusion-poor pyrite, with all these processes taking place before final compaction. The conversion of pyrrhotite to pyrite requires either the addition of sulfur or the loss of iron to the mineral system. Conversion of pyrrhotite to pyrite may be associated with the growth of euhedral pyrite, and the fluid that flowed through the sediments to supply the additional sulfide could have caused excess

pyrite growth in a layer that was particularly rich in pyrrhotite. As a result, the geochemistry of iron and sulfur in rocks with this texture of pyrite cannot be assumed to represent a purely sedimentary signal.

2.5.4. Iron Sulfide Minerals Forming During Compaction.

2.5.4.1. *Concretionary Pyrite.* Pyrite concretions show uniform compression around a circular to elliptical pyrite body ≥ 1 mm in diameter (Figure 2.3). Faint layering of pyrite may be observed within the shale around concretions. Some $100 - 500$ µm thick layers of pyrite have similar textures to those in the concretions.

The internal textures of concretions usually consist of a mix of inclusion-rich and inclusion-poor pyrite. Inclusion-rich pyrite forms irregular aggregates within the larger pyrite concretion. Many inclusion-rich pyrite areas contain bean-shaped inclusions of calcite $5 - 150$ µm in length. Small, lighter-colored euhedral pyrite crystals grow inward from the inclusion-rich pyrite into the calcite. Bean-shaped bodies of inclusion-poor pyrite outlined by kerogen and shale inclusions are common, and these lie on a continuum with bean-shaped calcite inclusions. Unlike with pyrite nodules, inclusion-poor pyrite does not seem to prefer a given side or location relative to the edge of a pyrite concretion.

Interpretation: These concretions and layers are interpreted as nucleating within the sediment and growing during and after compaction of the surrounding sediment based on the patterns in surrounding laminae. The uniform compaction of layers above and below the concretions suggest growth within the sediment prior to significant burial. The inclusion-rich pyrite may either replace synsedimentary pyrrhotite or represent the growth of pyrite crystals from multiple nuclei that included the host sediment. The prior presence of pyrrhotite could explain the presence of calcite crystal inclusions; the loss of volume during pyrrhotite recrystallization to pyrite could have produced voids in which calcite precipitated. Even if another process formed the calcite filled voids, later pyrite replacement of the calcite is indicated by the similarities in texture between the remaining bean-shaped calcite inclusions and bean-shaped areas of lighter, inclusion-poor pyrite; the similarities in texture suggest that lighter pyrite progressively replaced calcite during late diagenesis or early burial. Euhedral calcite may form within voids on top of concretions that opened during compaction.

2.5.4.2. *Feather Pyrite.* Feather pyrite is typically found within highly pyritized shale laminae (¿80% pyrite by volume) (Figure 2.0H). The tips of feather pyrite may grow in any direction relative to bedding, and the laminae it forms within may be horizontal to subvertical relative to horizontal. The laminae are softly deformed around the tips of the feathers.

Interpretation: Feather pyrite is interpreted to form along a diffusion gradient, where growth of the tips was fed by incoming ions. The lack of an overall direction of growth suggests that gradients of sulfide within the sediments were highly laterally variable.

2.5.4.3. *Blade Pyrite.* Blade pyrite is found at the top of one pyrite concretion within AIDP2 358.56 (Figure 2.0H). The base of the blade fans is above a zone of feather pyrite and inclusion-rich pyrite. The area of bladed pyrite forms a domed lens 1.5 to 0.7 mm thick that is cut by the edge of the thin section. The inclusion-rich pyrite above is deformed around the lens of blade pyrite.

Interpretation: Blade pyrite is inferred to form from the solid-state conversion of marcasite to pyrite, which preserves some relict anisotropy (*Murowchick*, 1992). Marcasite requires low (< 5) pH, which should dissolve calcite. However, a vein of calcite cuts through the blade pyrite lens, and calcite cores within pyrite inferred to form after pyrrhotite are observed in the overlying sediment. Additionally, some rounded grains of calcite are also seen in the overlying sediment, suggesting that acidic conditions were not present during primary deposition of sediment. At some point, conditions within the rock became acidic, driving marcasite precipitation locally but not enough to dissolve detrital calcite 1.5 mm above the blade pyrite lens. The inferred presence of several metastable iron sulfides within a small area suggests highly complex iron-sulfur chemistry.

2.5.5. Lenses of Pyrite and Sphalerite. Some layers of calcite are associated with lenses of sulfide minerals, usually composed of pyrite (Figure 2.3) with one sphalerite example (Figure 2.4). These lenses of sulfide minerals form elongate bodes which are pointed at the edges and thickest near the middle. The curvature to the tops and bottoms is about equivalent, with minimal deflection of laminae around the tops and bottoms of the lenses. Lenses of pyrite are mostly confined to a calcite layer, the tops can extend into the overlying shale. The sphalerite lens is within shale below rather than within a calcite layer. For both, the crystals are aggregates of small (~ 5 µm), usually euhedral crystals that have the same morphology whether they grew in shale or calcite. The crystals commonly crosscut the boundaries of rounded grains when replacing calcite.

Interpretation: The petrographic relationships suggest that most sulfide mineral growth in these lenses took place after the sediment had already mostly compacted. Thus, it is possible that the pyrite and sphalerite crystals nucleated during late diagenesis or early burial and replaced some of the original calcite. If these lenses did form after initial compaction, the small size of pyrite crystals is not sufficient to suggest precipitation during early diagenesis.

2.5.6. Post-Lithification Veins. Veins cut through at least seven samples, crosscutting all other petrographic textures. Thus, they are interpreted as forming after full lithification of the host rock. Most are filled with equant to elongate calcite crystals. They also contain various sulfide minerals as well as shale inclusions that are partly to mostly replaced by pyrite.

2.5.6.1. *Late Pyrite in a Vein Also Containing Chalcopyrite and Sphalerite.* In AIDP3 132.98, a vein cuts through shale (Figure 2.4A-D) with a near constant width of $\sim$ 700 µm. While it is mostly filled with calcite, it also contains pyrite and intergrown chalcopyrite and sphalerite. Disseminated pyrite, some consisting of 100 by 700 µm aggregates of rim pyrite, is found in a layer that begins no more than 100 µm from the upper edge of the vein (Figure 2.4C). Chalcopyrite and sphalerite are intergrown in the thickest limb of the vein, which is $\sim$ 1000 µm in thickness. Euhedral calcite crystals 200–500 µm in diameter compose most of the vein. Sphalerite is subhedral and forms 100—200 µm cubic crystals. Small (5 µm), round equant inclusions of chalcopyrite are found inside some sphalerite crystals. Chalcopyrite forms an anhedral web between sphalerite and calcite crystals. The vein cuts through shale, which is pyritized to $\sim$ 80% by volume in the pyrite-rich region. The pyrite here forms 200—500 µm wedges which are more heavily included away from the calcite vein. Euhedral pyrite crystals (100 — 200 µm) with fewer inclusions are found at the edges of the calcite vein. These euhedral crystals of pyrite crosscut intergrown calcite, chalcopyrite, and sphalerite.

Interpretation: The presence of various sulfide minerals suggests that a fluid containing copper, zinc, calcium, sulfide, and carbonate cut through shale, resulting in precipitation of calcite, chalcopyrite, and sphalerite. Later fluid flow delivered iron to drive the precipitation of pyrite. The relatively large size of the cubic pyrite crystals suggests that they formed under nucleation-limited conditions.

2.5.6.2. *Nucleation-Dominated Pyrite in a Vein.* In sample AIDP3 136.57 a vein mostly filled with calcite also has small, equant subhedral pyrite crystals (Figure 2.4E and F). The vein crosscuts shale and carbonate layers, with anhedral host calcite crystals. The vein-filling calcite crystals are euhedral and $\sim$ 200 µm in diameter. The pyrite crystals are concentrated along specific margins between euhedral calcite crystals. They are all roughly the same size, 5 µm in diameter, and occasionally have kerogen inclusions at the center.

Interpretation: The small pyrite crystals are interpreted to have precipitated from the vein fluid after precipitation of the calcite. Their small, uniform size and close spatial association suggests that the formed under nucleation-dominated pyrite growth conditions. The kerogen at the center of some pyrite crystals could represent the remnants of a subsurface biosphere, which would require relatively low temperatures when they formed, possibly associated with uplift. Alternatively, kerogen could represent oil mobilized from deeper sediments during metamorphosis.

2.5.7. Relative Timing of Different Pyrite Textures. Petrographic relationships demonstrate that pyrite precipitated during multiple intervals ranging from nodules on the seafloor to inclusion-poor pyrite within post-lithification veins. Textures such as seafloor nodules should be targeted for geochemical analyses relating to questions about surface processes during the 2.63 Gya euxinic event. Diagenetic pyrite textures forming during compaction such as feather pyrite need further characterization for interpretation. Blade pyrite may have shifts in trace elements and isotopes that could represent changing conditions during diagenesis. Some late-precipitating pyrite has size and morphological characteristics that are similar to disseminated pyrite that is typically analyzed for bulk geochemistry. Thus, comparisons between bulk analyses of sulfur isotopes and metal concentrations within pyrite should be directly compared between pyrite inferred to form at different times.

In one thin section (Figure 2.5), the relative timing of a nucleation-dominated lens, concretion growth, and calcite vein formation can be inferred from textures. The wings to the side of the nucleation-dominated layer come are flat-lying except over the top of a rounded pyrite concretion. The wing of the lens is deflected around the top of the concretion, following the deflection of the pyrite laminae. The vein of calcite runs parallel to the top of the pyrite lens, and some pyrite of the same size as within the lens is seen cutting across the calcite crystal contacts.

Concretion growth happened while the sediment was still soft, resulting in compaction around a growing concretion. A vein of calcite cut across the shale after compaction had mostly finished. The fluid that delivered the vein also delivered either sulfide or iron, which precipitated as pyrite along a band of increased concentration of either iron or sulfide. Nucleation of pyrite crystals continued after the precipitation of calcite within the vein.

2.6. Conclusion

Pyrite within sediments spanning the 2.63 Gya euxinic event show a diversity of textures, requiring multiple generations of pyrite precipitation. The presence of anisotropic pyrite suggesting marcasite conversion and rim pyrite suggesting pyrrhotite dissolution suggests that iron and sulfide chemistry was highly dynamic during diagenesis and metamorphism. Although it is assumed that small crystals of pyrite within shale precipitated during early diagenesis, pyrite crystal size does not predict the timing of formation. Many small crystals of pyrite must have precipitated at the same time or after post-compaction veins. In the light of petrographic evidence suggesting a dynamic seafloor and subsurface iron and sulfur chemistry, researchers working on the 2.63 Gya euxinic interval should be aware of when analyzed pyrite precipitated, and what that timing could reveal about geochemistry at different stages of lithification. Further work on the geochemistry of early-forming textures such as pyrite nodules may more accurately reflect surface cycling of iron, sulfur, and carbon chemistry during the 2.63 Gya euxinic event. Future studies of this interval might lump processes happening at different times during diagenesis if they ignore the petrographic relationships recorded in pyrite textures.

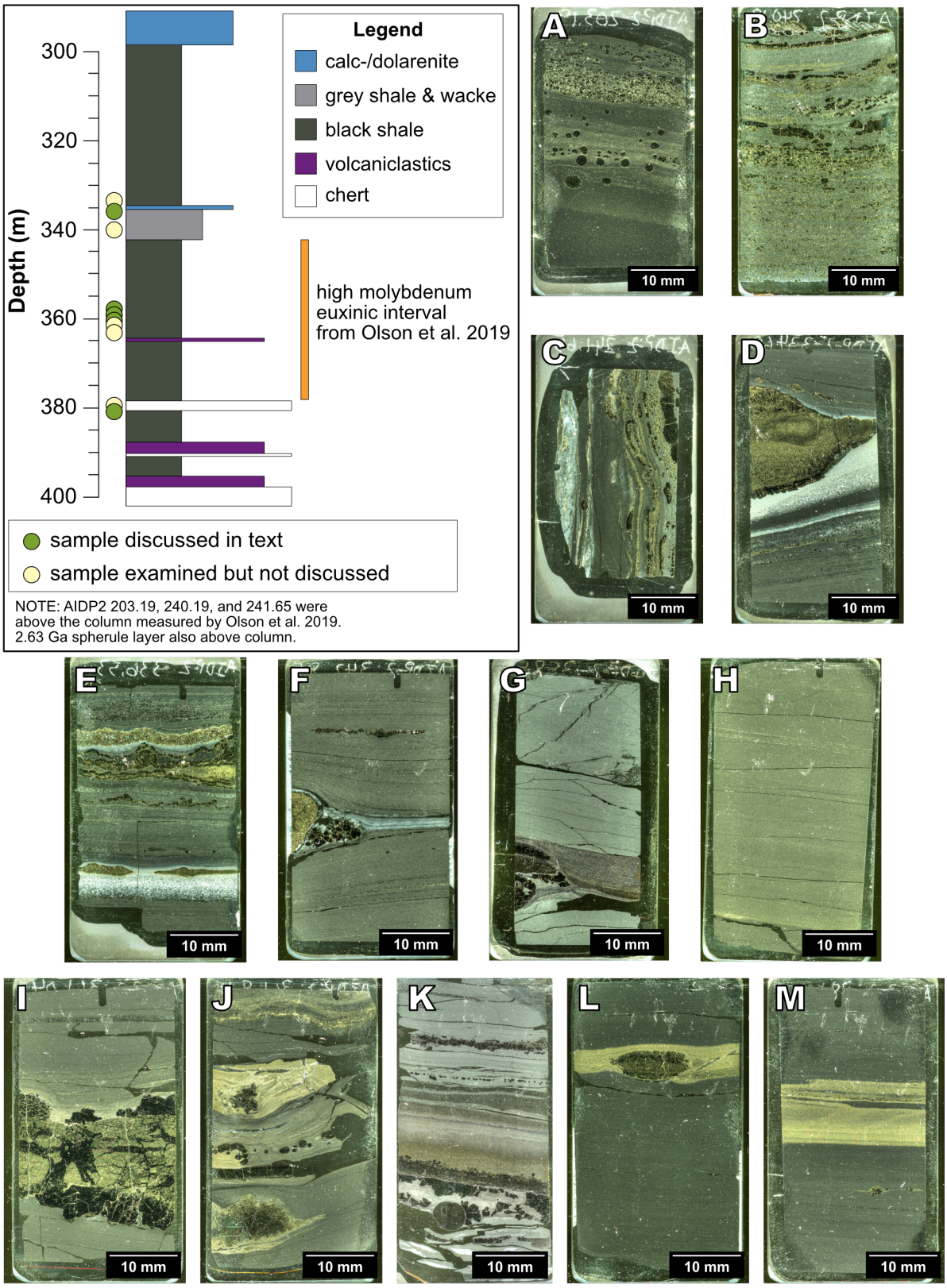
Depth (m)
300
320
340
360
380
400
Legend
calc-/dolarenite
grey shale & wacke
black shale
volcaniclastics
chert
high molybdenum
euxinic interval
from Olson et al. 2019
sample discussed in text
sample examined but not discussed
NOTE: AIDP2 203.19, 240.19, and 241.65 were
above the column measured by Olson et al. 2019.
2.63 Ga spherule layer also above column.
A
B
C
D
E
F
G
H
I
J
K
L
M
10 mm

Figure 2.0. AIDP2 30 µm thin sections scanned in reflected light. Numbers represent core depths. A: AIDP2 203.19 B: AIDP2 240.19 C: AIDP2 241.65 D: AIDP2 334.60 E: AIDP2 336.53 F: AIDP2 342.86 G: AIDP2 358.56 H: AIDP2 359.41 I: AIDP2 361.04 J: AIDP2 361.91 K: AIDP2 362.68 L: AIDP2 380.94 M: AIDP2 381.45 Inset: Depths of samples described and their location within the geochemical zones measured by Olson et al. 2019.

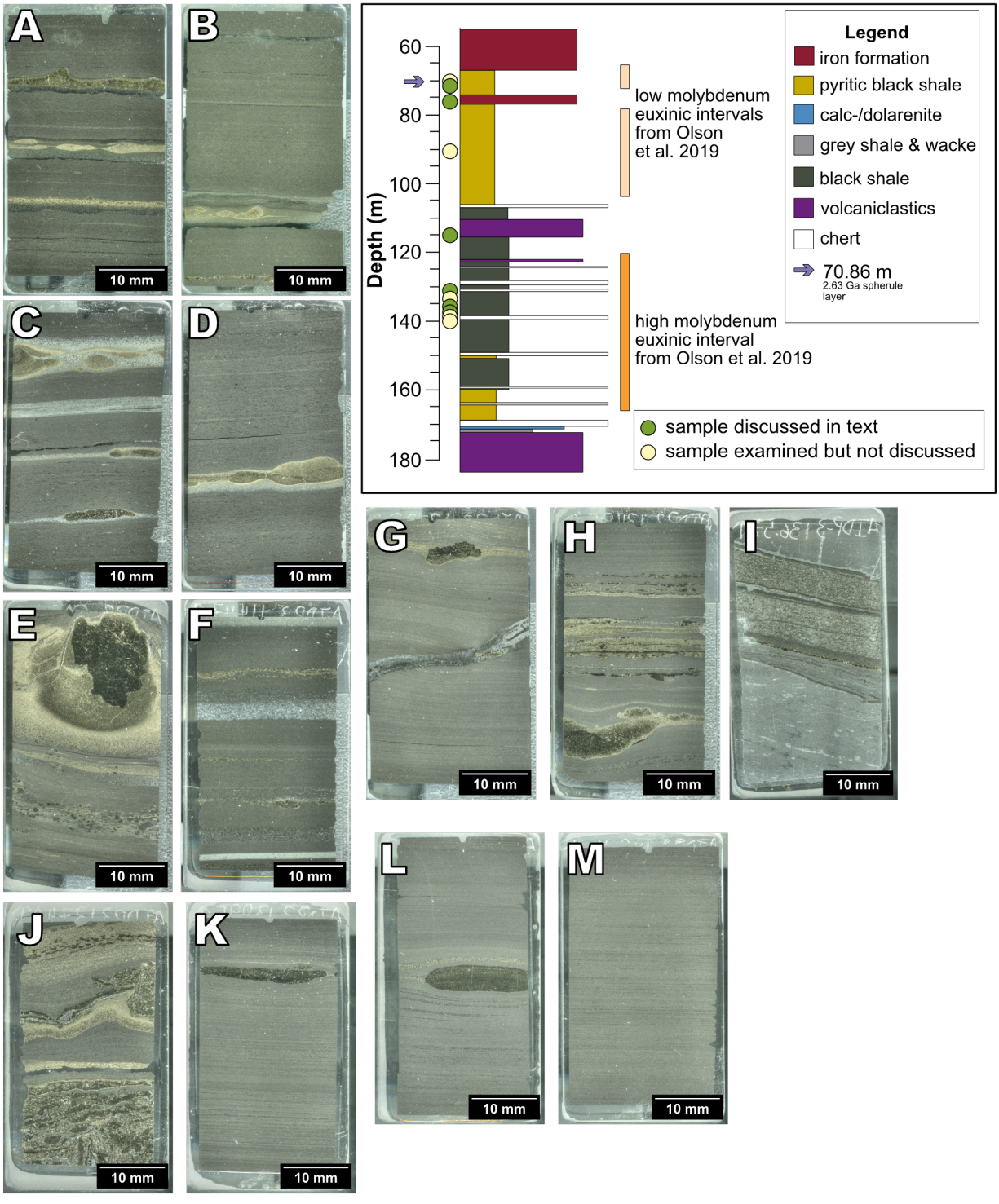
A
B
C
D
E
F
G
H
I
J
K
L
M
10 mm
Depth (m)
60
80
100
120
140
160
180
low molybdenum euxinic intervals from Olson et al. 2019
high molybdenum euxinic interval from Olson et al. 2019
Legend
iron formation
pyritic black shale
calc-/dolarenite
grey shale & wacke
black shale
volcaniclastics
chert
70.86 m
2.63 Ga spherule layer
sample discussed in text
sample examined but not discussed

Figure 2.0. AIDP3 30 µm thin sections scanned in reflected light. Numbers represent core depths. A: 70.80 B: 70.70 C: 77.01 D: 77.50 E: 90.99 F: 114.47 G: 132.98 H: 134.95 I: 136.57 J: 137.40 K: 138.95 L: 140.04 M: 140.34 Inset: Depths of samples described and their location within the geochemical zones measured by Olson et al. 2019.

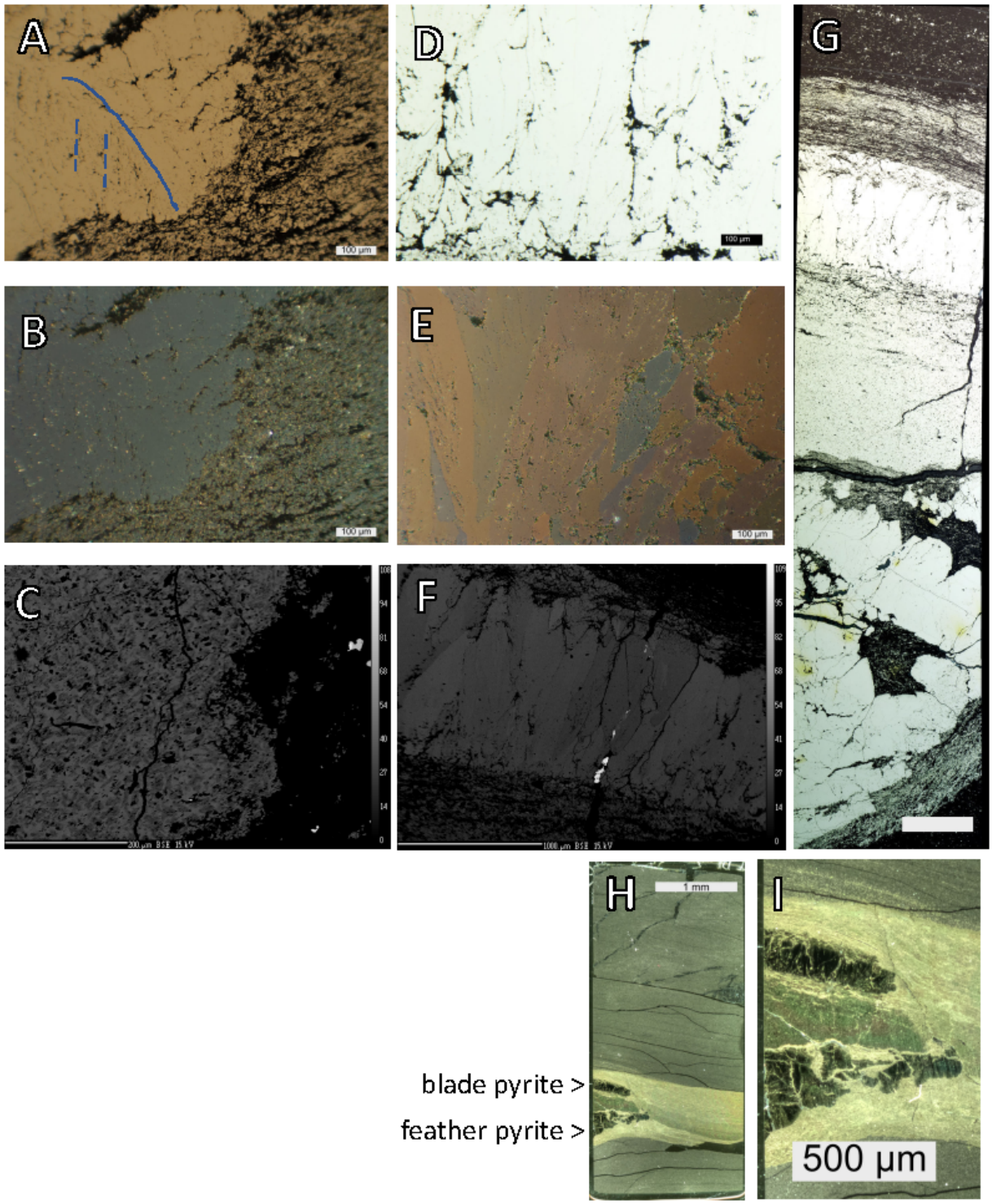
A
D
G
B
E
C
F
H
I
blade pyrite >
feather pyrite >
1 mm
500 µm

Figure 2.0. Feather and blade pyrite. A, B: Feather pyrite under plane (A) and crossed (B) polarized light. The pyrite here has a feather-like texture, with a central inclusion-poor section (solid line) with radiating lines of pores (dashed lines) heading off at a 30 degree angle from the inclusion-poor core. The view under crossed polars shows that there is no anisotropy associated with the feather pyrite. C: EDS image of the inclusion-rich pyrite between the blade and feather pyrite, showing how the crystal structure appears mottled. The rough parallel alignment of the pores can be seen near the top of the pyritic feature. D, E: Blade pyrite under plane (D) and crossed (E) polarized light. Pores of pyrite are arranged along lines that diverge upward from each other away from a rounded to pointed origin. The image under crossed polars shows a red-blue anisotropy that is interpreted to result from solid-state conversion of marcasite to pyrite. F: EDS image of blade pyrite, showing subtle variations in electron density along the domains of pyrite. A calcite vein (black) filled with sphalerite (bright white) cuts diagonally starting from the center of the bottom of the image. G: Large photomosaic of the feather and blade pyrite region. H: AIDP2 358.56 thin section scan, with locations of feather and blade pyrite marked. I: Detail of feather and blade region.

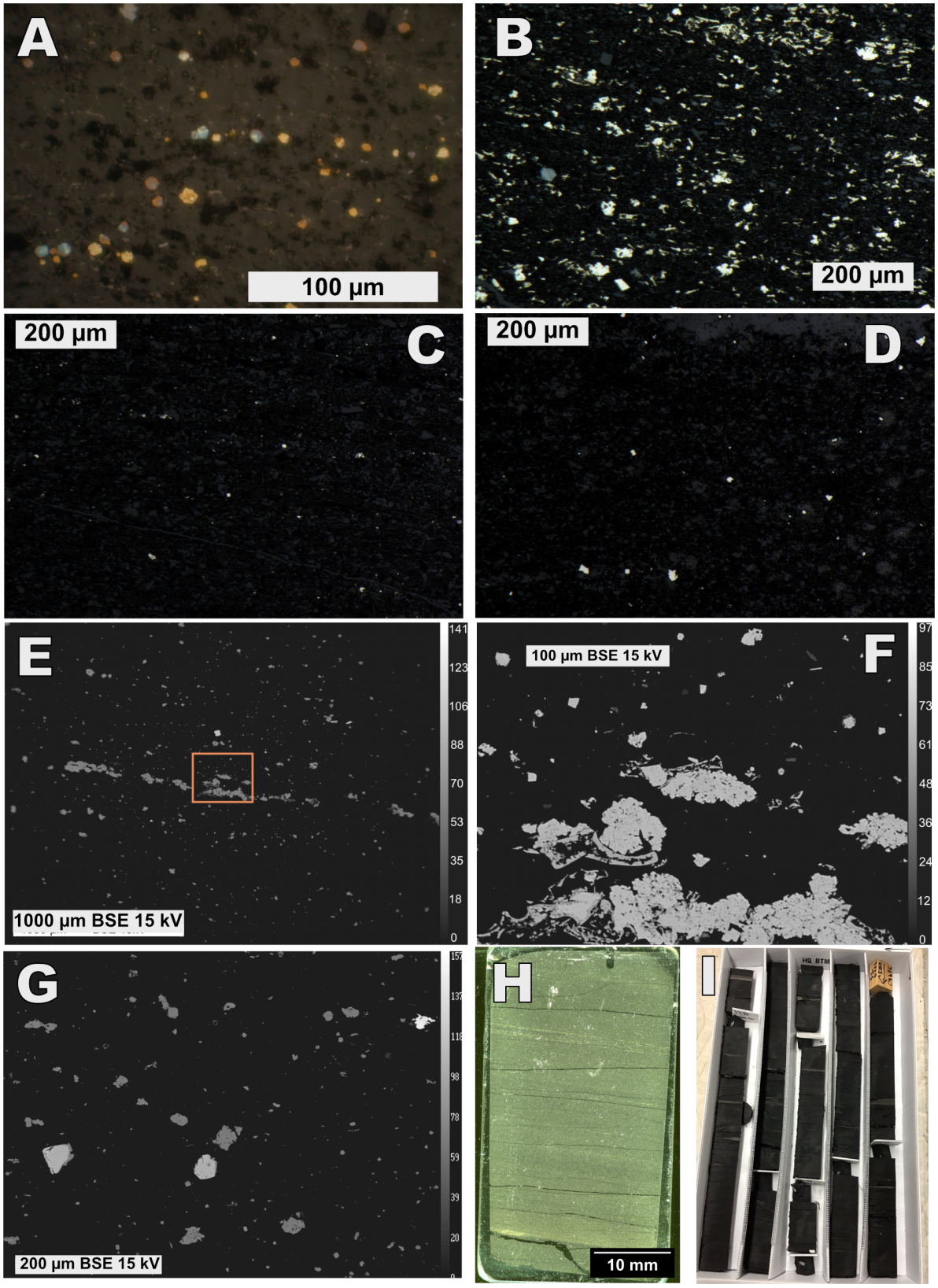
A
100 µm
B
200 µm
200 µm
C
200 µm
D
E
1000 µm BSE 15 kV
141
123
106
88
70
53
35
18
0
100 µm BSE 15 kV
F
97
85
73
61
48
36
24
12
0
G
200 µm BSE 15 kV
H
10 mm
I
HQ BTM

Figure 2.1. Small isolated pyrite crystals. A: AIDP3 70.80 30um. Disseminated pyrite with euhedral habit, equant, $\sim$ 5 µm in diameter, loosely arranged in layers, in a mostly calcite matrix with minor silica cements and shale minerals. Color differences are due to the presence of tarnish. Euhedral pyrite lacks sub-µm pores. B: AIDP2 358.56 30 µm. Disseminated pyrite with a primarily amorphous habit, variable in length and width, loosely arranged in layers, in a mostly clay matrix. C: AIDP2 336.53 30 µm. Sparsely disseminated pyrite, consisting of roughly equal amounts of euhedral and amorphous disseminated pyrite. Pyrite is found loosely associated with discontinuous laminations of calcite rather than laminations of shale. D: AIDP2 361.04 30 um, Sparsely disseminated pyrite found below a graded bed interpreted as a microturbidite. E, F, G: AIDP2 359.41 BSE: Different textures of pyrite seen in a typical sample chosen for inorganic chemical analysis (H). I: AIDP3 core box showing the locations and textures of samples chosen for inorganic chemical analysis. Samples were chosen based on the apparent lack of large bodies of pyrite at the hand sample scale.

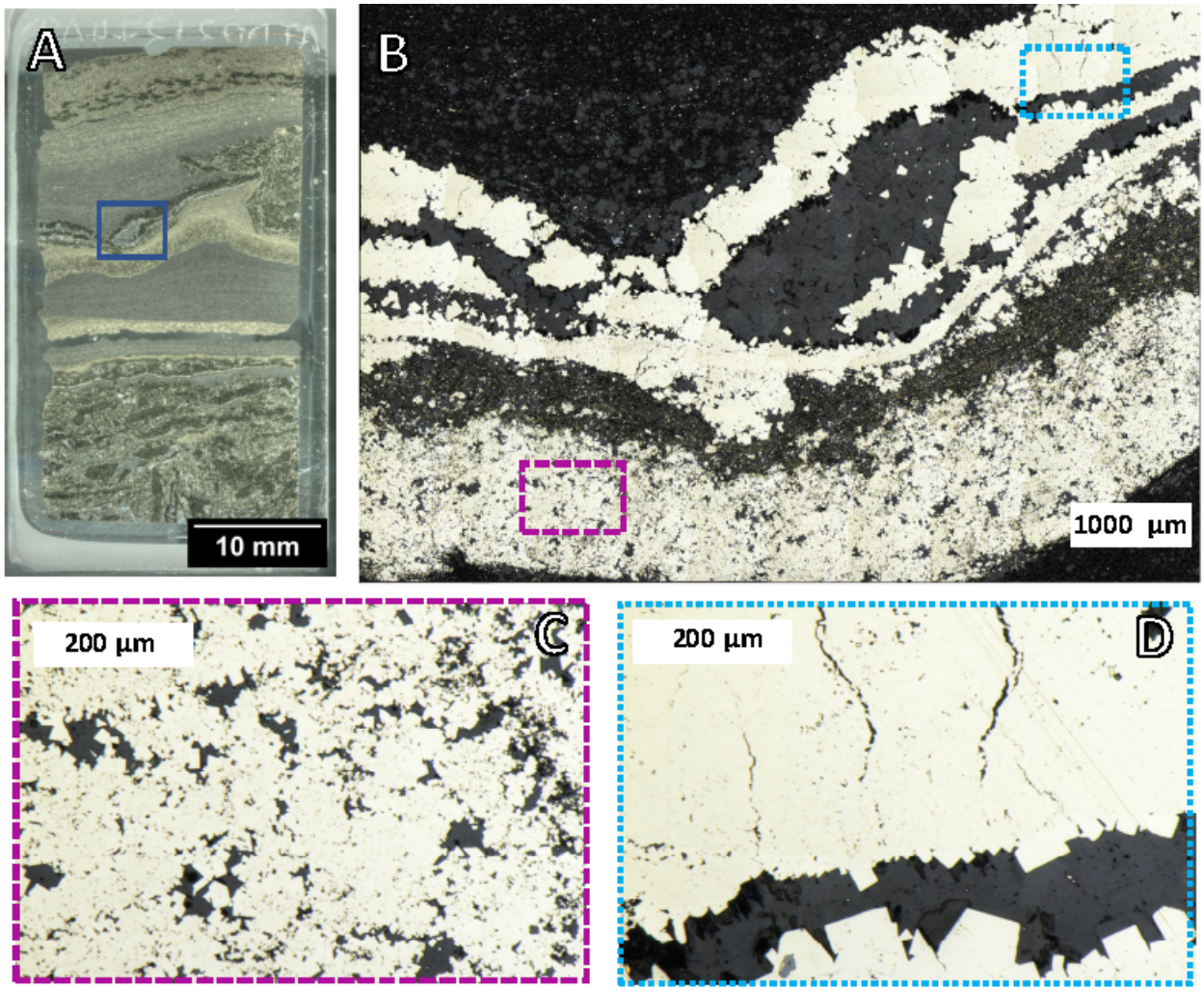

Figure 2.2. Aggregated pyrite crystals. A: AIDP3 137.40 30 µm. Area shown in B is outlined in blue. B: Euhedral, inclusion-poor cubic pyrite forms on the interior of pyrite layers. The crystal edges can be most easily seen inside of the calcite that runs through the middle of the image. At the top of the image, disseminated pyrite is found among shale minerals and calcite. C: Texture below the vein showing euhedral pyrite crystals growing over calcite, at multiple scales ranging from 5 to 20 µm crystal size. This texture suggests that pyrite crystal nucleated while earlier-nucleated crystals continued to grow larger. D: Close up view of the carbonate and pyrite at the top of A. Large euhedral crystals of pyrite (20 – 100 µm) grow into the calcite on both sides of the vein. A bleb of grey sphalerite and yellow chalcopyrite is present in the lower-left part of the image.

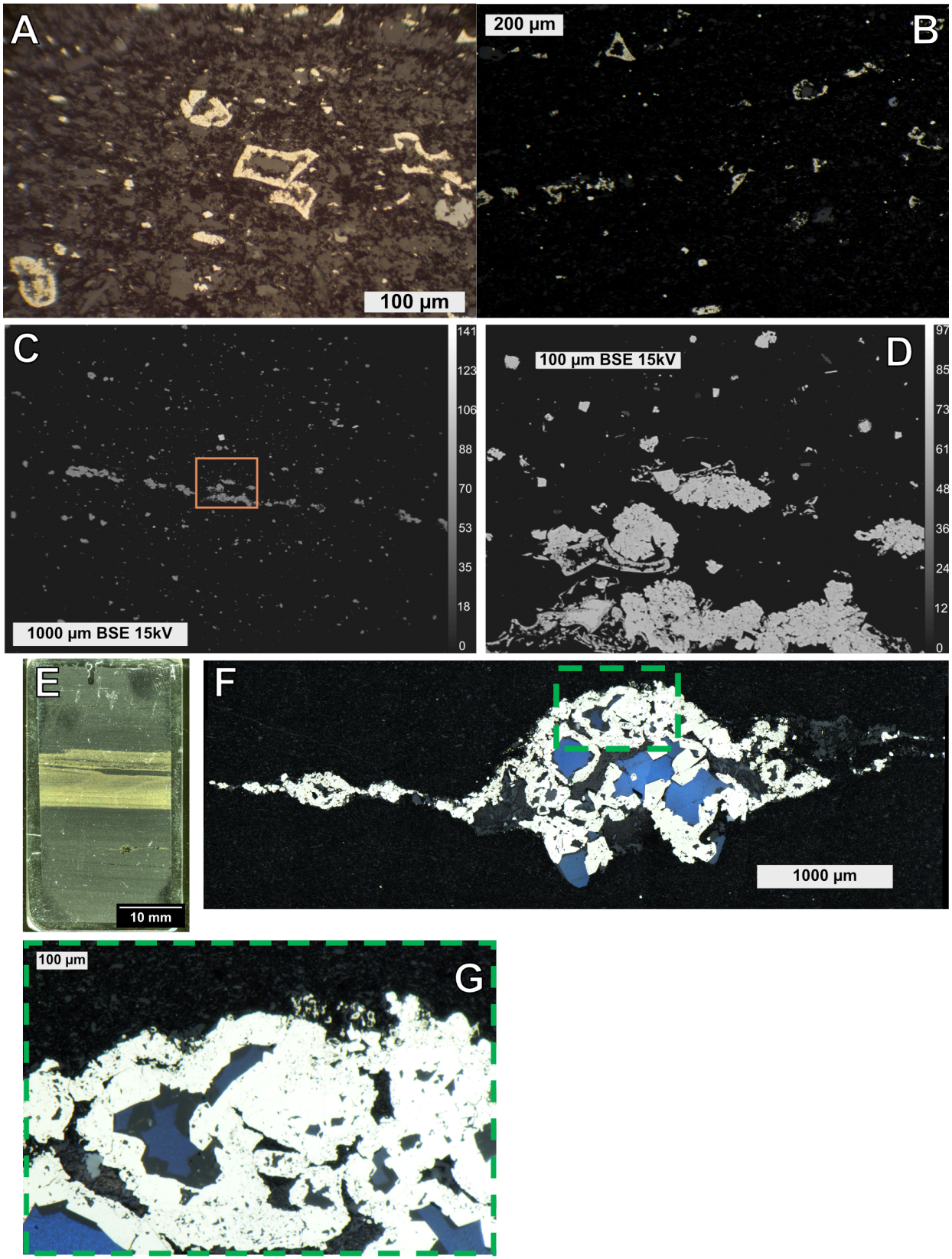
A
100 µm
200 µm
B
C
1000 µm BSE 15kV
141
123
106
88
70
53
35
18
0
100 µm BSE 15kV
D
97
85
73
61
48
36
24
12
0
E
10 mm
F
1000 µm
100 µm
G

Figure 2.2. Pyrite rimming calcite. A, B: AIDP3 132.98 30 µm, plane-polarized reflected light. Disseminated pyrite grain outlines, with carbonate core. The smooth outside edge and the jagged inner edge define a border $\sim$ 10 µm across. This texture likely represents dissolution of pyrrhotite and reprecipitation of pyrite. C, D: AIDP2 359.41 BSE. Rim pyrite around calcite is seen in the layer at the center of C, enlarged in D. E: AIDP2 381.45 30 µm, blue box shows location of F. F: Lens of pyrite and calcite. The pyrite forms rims around calcite. G: Detail of an area in F. Rim pyrite around calcite at a scale similar to A-D, outlined in F by dashed green line. Larger ($>$ 100 µm) calcite inclusions within pyrite are rimmed by comparatively thicker rims of pyrite, which has a more euhedral form and longer crystal size, particularly at the center left of the image.

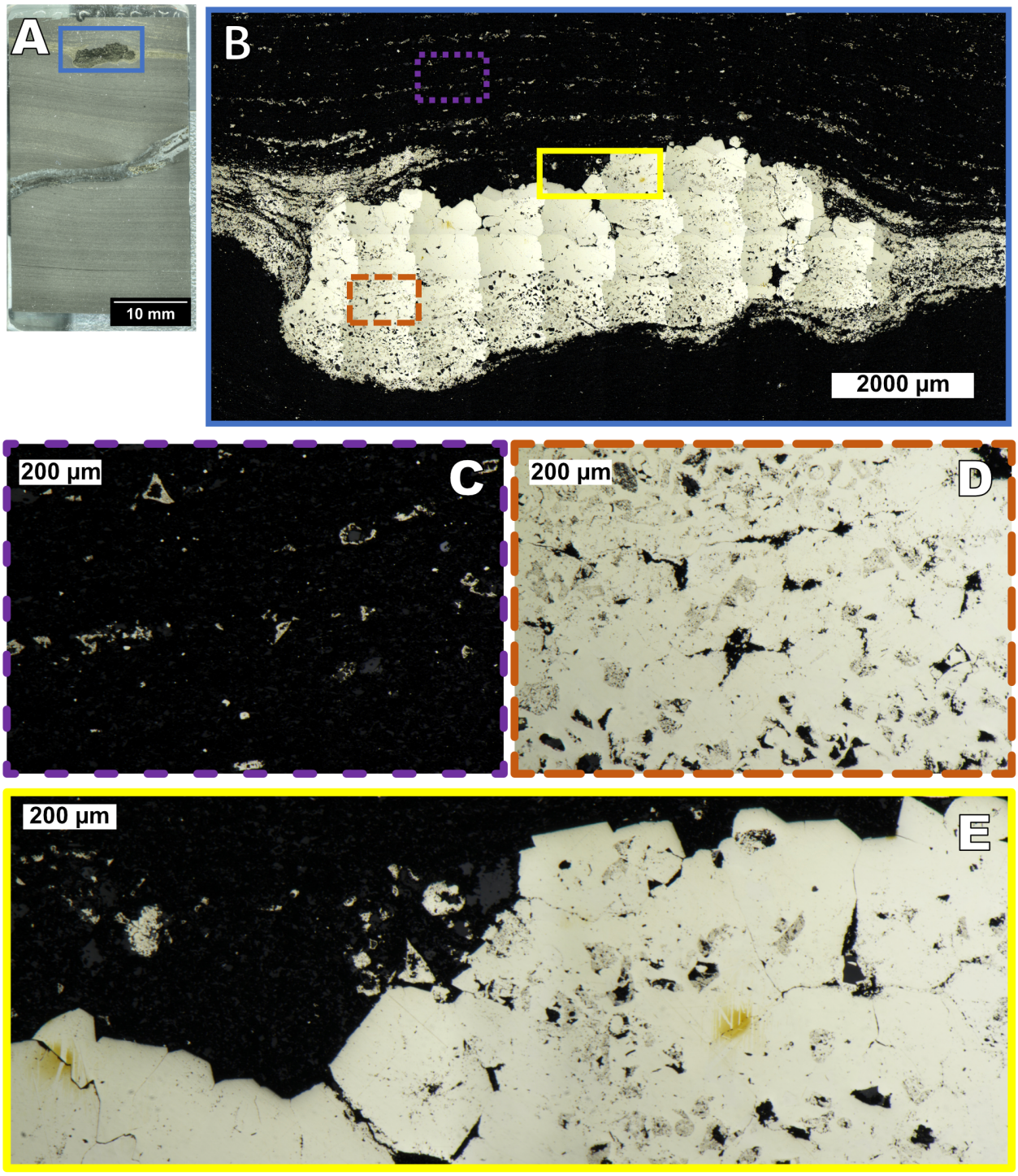
A
10 mm
B
2000 µm
200 µm
C
200 µm
D
200 µm
E

Figure 2.2. Pyrrhotite recrystallization within a pyrite concretion. A: AIDP3 132.98 30 µm. The blue box highlights the area shown in B. B: Composite micrograph of the pyrite concretion. The top part of the image has pyrite loosely arranged in layers consisting of polyhedral zones of inclusion-rich pyrite with calcite cores. The top of the pyrite concretion has fewer inclusions than the bottom. The locations of figures C, D, and E are shown in different colored boxes with different line dashes. C: A layer of rim pyrite above the pyrite concretion. D: The interior of the pyrite concretion, showing structures defined by increased inclusions within an inclusion-poor pyrite background. The size and sharp-sided geometry of these inclusion bodies is the same as for the rim pyrite in the surrounding layers. E: The top of the inclusion-poor pyrite at the top of the pyrite concretion. The layer of rim pyrite continues past the edge of inclusion-poor pyrite going into the interior of the pyrite concretion.

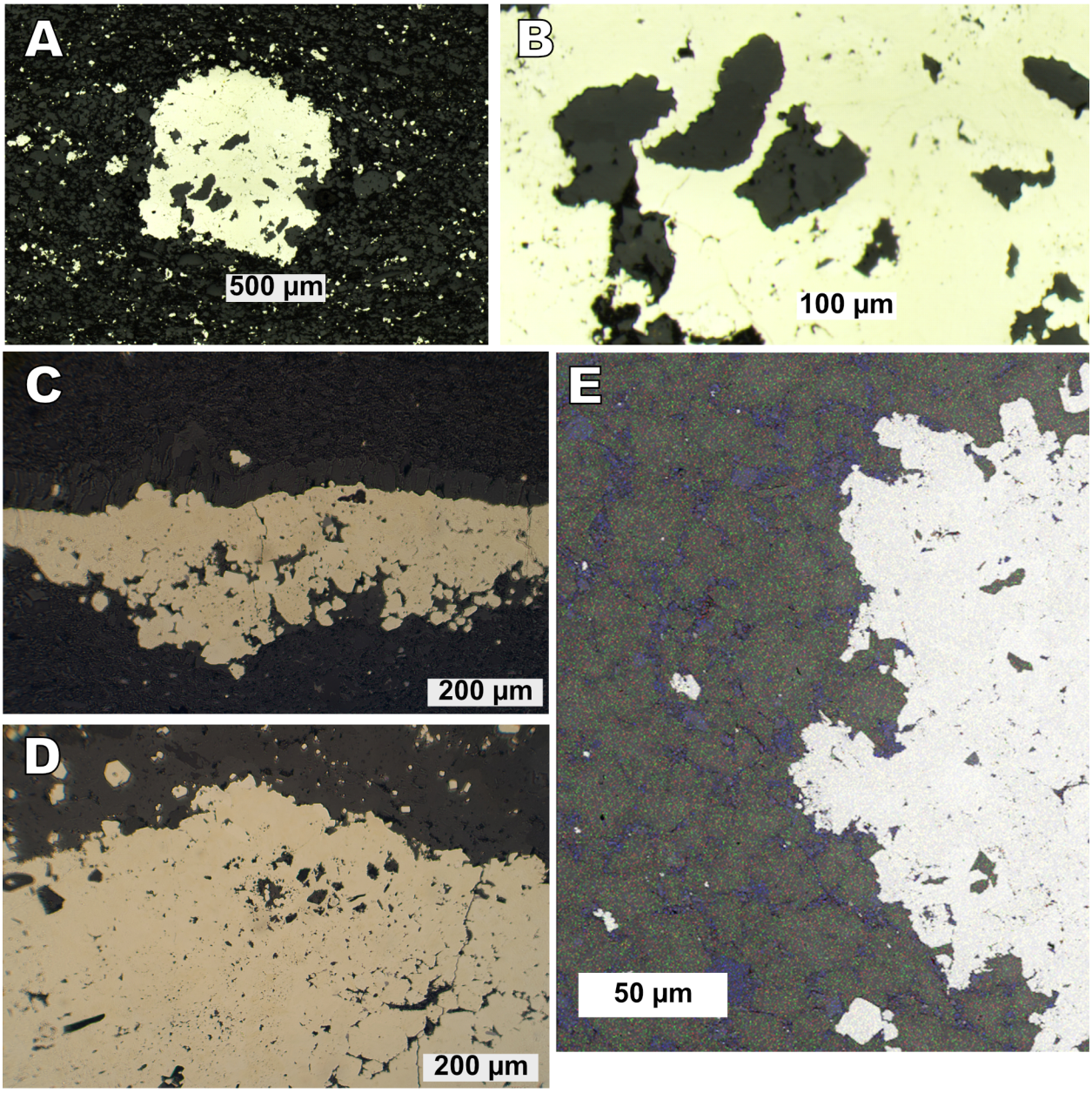

Figure 2.3. Concretionary pyrite. A: AIDP2 203.19. This pyrite concretion is rounded on top and flat on the sides and bottoms. B: Bean-shaped inclusions of calcite 50-150 um in length within the pyrite concretion. Small euhedral crystal points of inclusion-poor pyrite growing inward from the boundary of the calcite inclusion. C: AIDP3 114.47 30 µm. Layer of pyrite below a calcite vein. The pyrite within this layer consists of a darker yellow, inclusion-rich part and a lighter-colored inclusion-poor part. Subhedral to euhedral crystals of lighter-colored pyrite can be observed within carbonate at the bottom and middle of the pyrite layer. D: AIDP3 114.47 30 µm, lateral from C. Detail of the top of the pyrite layer in C . Lighter inclusion-poor pyrite forms rounded to subrounded shapes within the inclusion-poor pyrite that are most readily seen around the calcite inclusions at the top center of the pyrite. E: Element map of the side of a different concretion in AIDP2 203.19 than the concretions shown in A and B. The bean-shaped inclusions inside of the concretion are filled with calcite. Blue = Si, Red = C, Green = Ca, S = yellow, overlaid on black and white EDS.

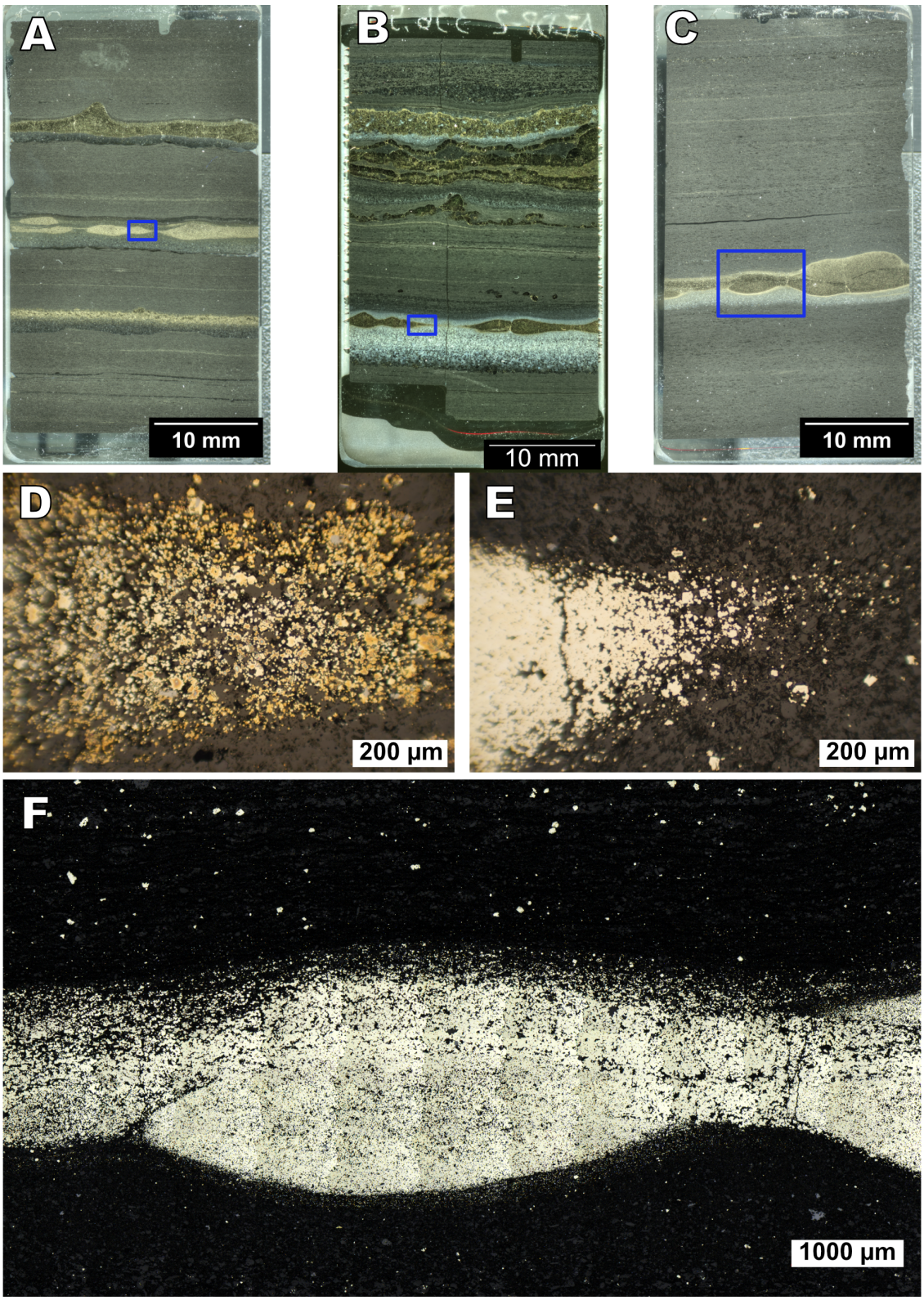
A
10 mm
B
10 mm
C
10 mm
D
200 µm
E
200 µm
F
1000 µm

Figure 2.3. Pyrite lenses within calcite. A: AIDP2 336.53, with location of D marked. B: AIDP3 70.80, with location of E marked. C: AIDP3 77.50, with location of F marked. D: Detail of area outlined in A. The small pyrite crystals cross-cut rounded grains of calcite. E: Detail of area outlined in B. The edge of a lens. The texture within the calcite surrounding the lends does not appear to change with the density of pyrite crystals. F: Detail of area outlined in C. There is minimal deflection of surrounding shale laminae around the rounded top and bottom of this lens of nucleation-dominated pyrite.

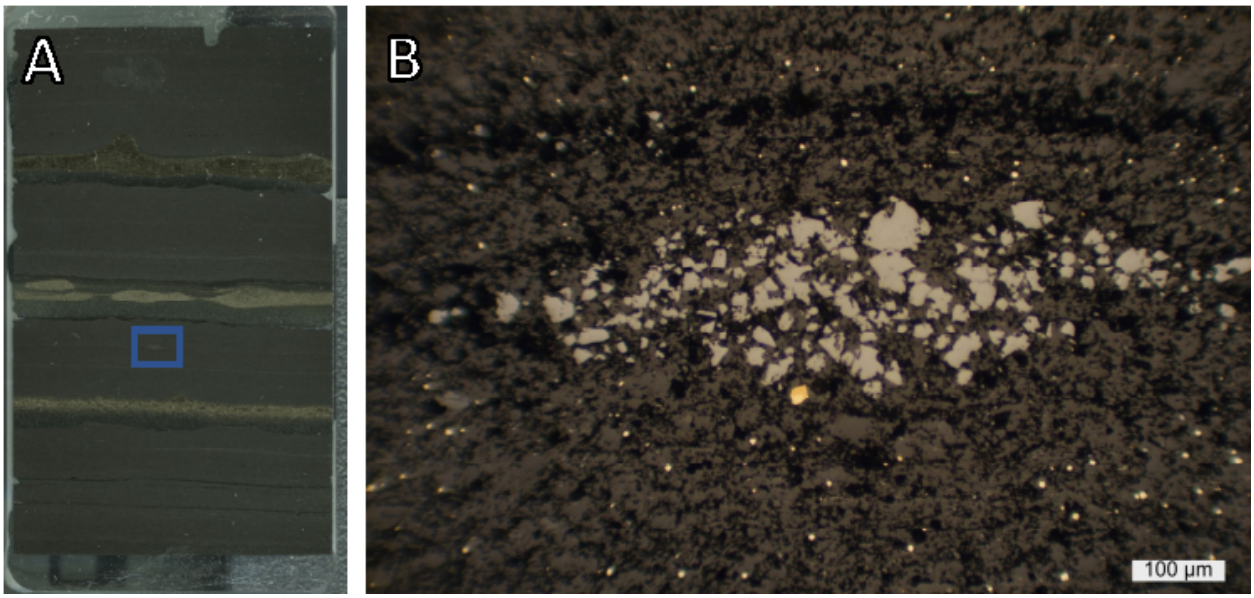

Figure 2.4. Lens of sphalerite. A: Reflected light scan of AIDP3 70.80 30 um. Blue box indicates the location of micrograph in B. B: Lens of nearly pure sphalerite surrounded by disseminated pyrite. Grains are angular to subrounded with diameter 5-40 um. The small size suggests nucleation-dominated growth similar to the texture of nucleation-dominated growth of pyrite.

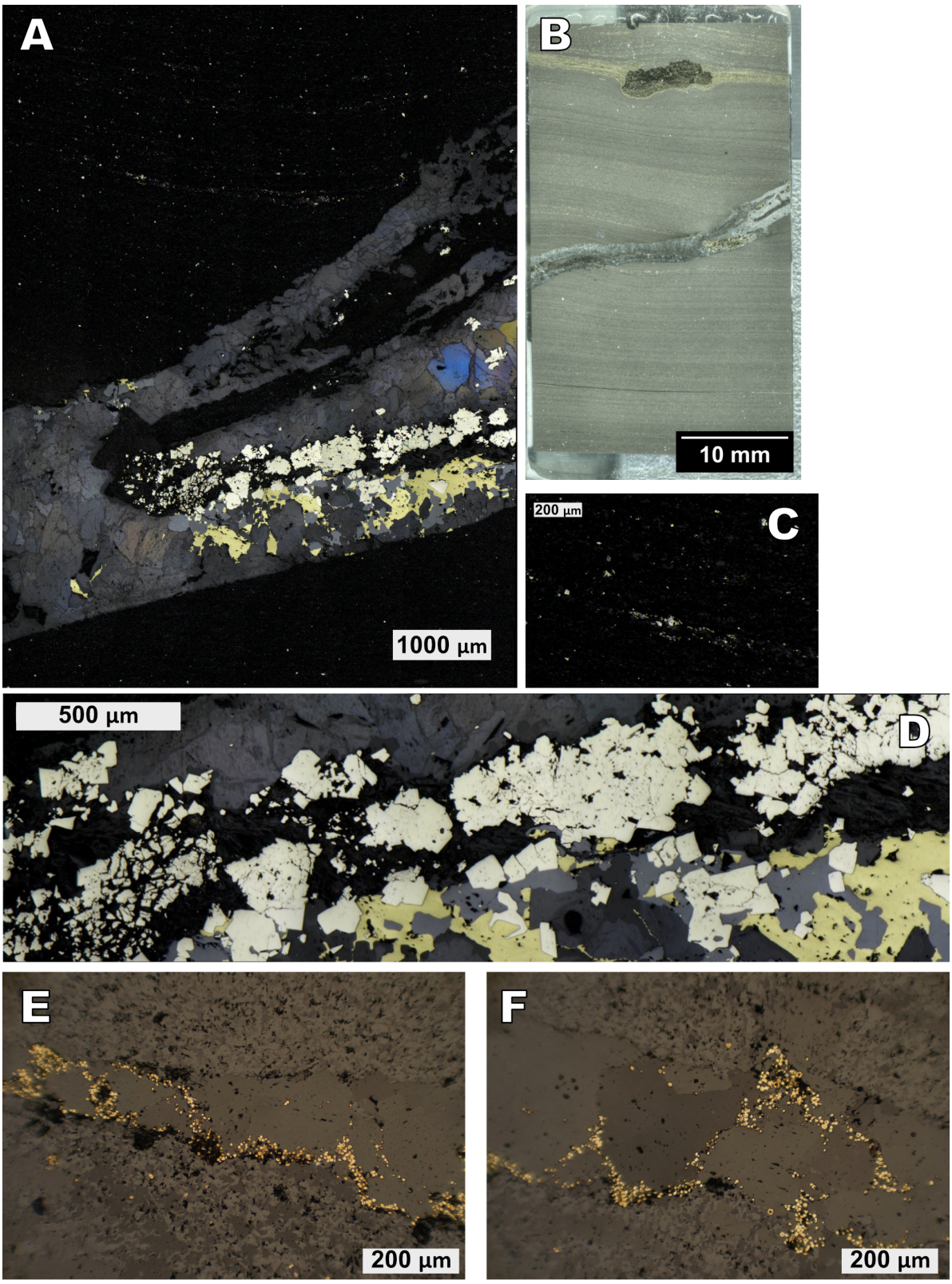
A
1000 µm
B
10 mm
200 µm
C
500 µm
D
E
200 µm
F
200 µm

Figure 2.4. Vein-associated pyrite, sphalerite, and chalcopyrite. Micrographs A-D are from AIDP3 132.98 30 um (B). Micrographs E and F are from AIDP3 136.57. A: Detail of calcite vein cutting through shale. The location of the micrograph is outlined in B. C: Pyrite to the side of the vein consists of a layer of rim pyrite. D: Close-up of the center of the vein, showing the texture of the pyrite between two legs of the veins. Pyrite within shale is broken up and consists of euhedral to subhedral crystals with inclusions concentrated towards the center. At the bottom, yellower chalcopyrite and gray sphalerite intergrow with the calcite in the vein. Euhedral pyrite crosscuts the fabric of sphalerite and chalcopyrite. E, F: Nucleation-dominated pyrite along crystal boundaries between large calcite crystals. Vein cuts through smaller anhedral calcite.

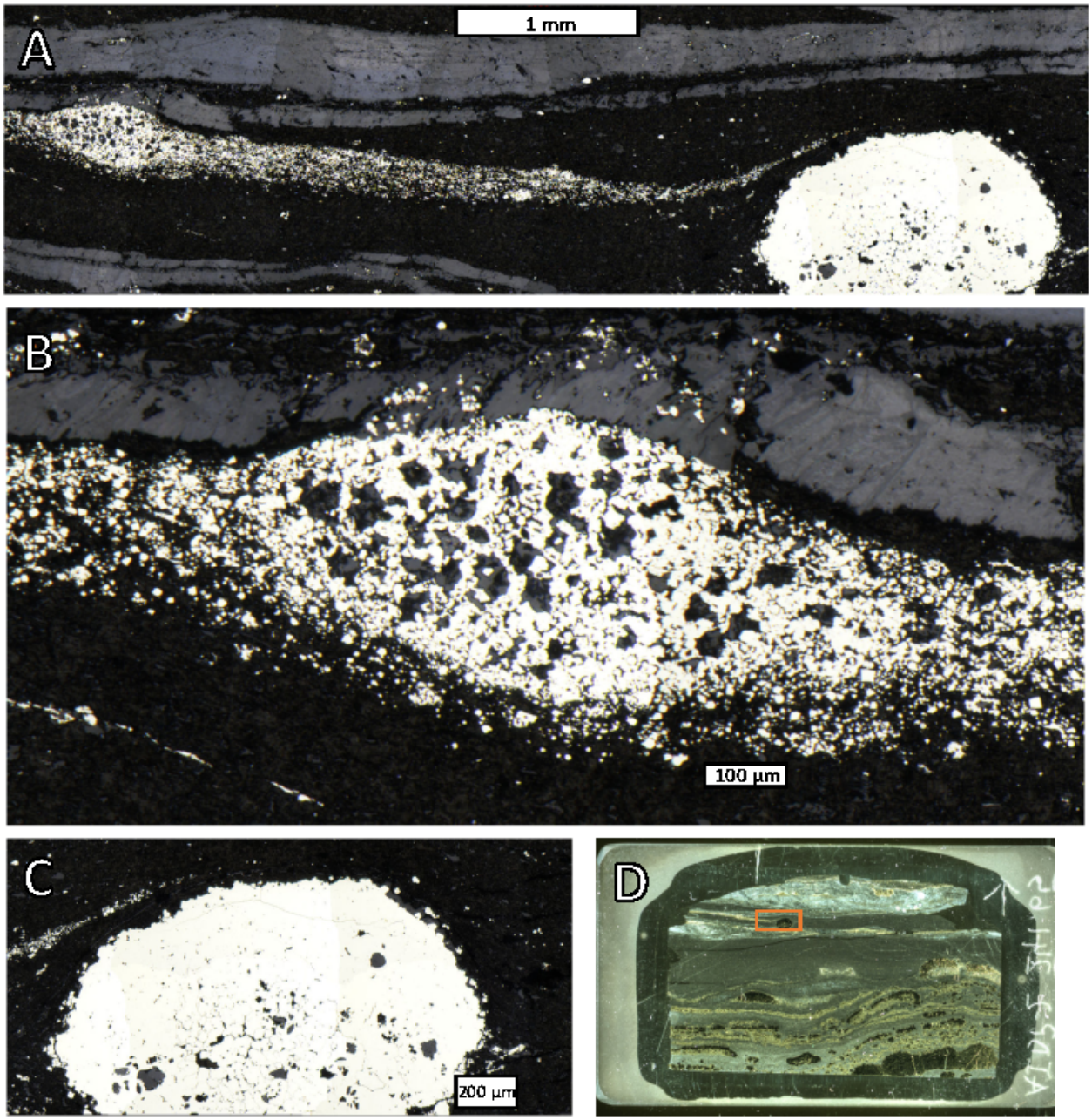

Figure 2.5. Timing information from thin section AIDP2 241.65. A: Large mosaic from AIDP2 241.65 showing nucleation-dominated pyrite lens, pyrite concretion, and calcite vein. B: Detail of nucleation-dominated layer near a calcite vein. C: The rounded concretion deflects the rightmost edge of the nucleation-dominated layer. D: Reflected light scan of AIDP2 241.65, showing the location of the large micrograph (B) in orange.

CHAPTER 3

Archean Seafloor Pyrite Nodules

3.1. Abstract

The 2.63 Gya Jeerinah Formation contains pyrite nodules that show textural evidence of having precipitated on the Neoarchean seafloor. Shale and thin carbonate turbidites lap onto the nodules, demonstrating relief on the seafloor over the nodules. In addition, overhanging pyrite growths produced shelter porosity later filled with calcite. The petrographic textures at the tops of the nodules are sometimes laminated and columnar in contrast to euhedral crystal forms at the bases of nodules, demonstrating different growth conditions upward versus downward. This differential growth of nodules at the seafloor is analogous to polymetallic manganese nodules in the modern ocean. These very unusual iron sulfide seafloor nodules suggest that iron and sulfur cycling may have been unique in Earth history during this ca. 20 Ma interval, consistent with an overall exceptionally high concentration of pyrite in a subtidal siliciclastic/carbonate ramp of this age.

3.2. Introduction

Neoarchean time represents a significant transition from an anoxic world to one with an increasing amount of local accumulation of molecular oxygen from photosynthesis. This production of O_2 affected the cycling of all biologically and redox-active elements, particularly the iron and sulfur cycles through the oxidation and re-reduction of iron and sulfur species in the atmosphere, on land, and in seawater (*Bosco-Santos et al.*, 2020; *Eroglu et al.*, 2018; *Havig et al.*, 2017; *Johnston*, 2011; *Ostrander et al.*, 2021). Substantial research has gone into trying to understand these changes, particularly through analyses of black shales and banded iron formations (i.e. *Araújo and Lobato* (2019); *French et al.* (2015); *Mukhopadhyay* (2019); *Olson et al.* (2019); *Schröder et al.* (2006). Interestingly, there is an interval with an exceptionally high concentration of pyrite in $\sim 2.65 - 2.63$ Gya subtidal mixed carbonate-shale facies (Chapter 1). This pyrite has multiple origins (Chapter 2). Here, I document the formation of pyrite nodules on the Neoarchean seafloor and provide

an initial interpretation of conditions allowing their formation related to mineral precipitation in geochemical gradients between sediments and seawater.

3.2.1. Mineral Precipitation at Geochemical Gradients. Metal oxides and sulfides form in geochemical gradients due to both microbial processes and mixing of fluids in disequilibrium. Even modern oceanic sediments tend to be highly reduced, owing to the presence of bacteria that rapidly consume oxygen, nitrate, and sulfate along a redox gradient ((*Liu et al.*, 2020b). Therefore, oceanic sediments under oxic waters tend to be characterized by a relatively steep geochemical redox gradient (e.g. *Schieber* (2002a, 2011)). These gradients can induce the precipitation of polymetallic manganese nodules (*Kuhn et al.*, 2017).

Polymetallic manganese nodule growth is divided into hydrogenetic growth and diagenetic growth, which have different petrographic textures (*Kuhn et al.* (2017) and references therein). Hydrogenetic Mn and Fe oxides precipitate from colloids directly from oxic seawater. This style of precipitation also forms ferromanganese crusts on hard rock surfaces of seamounts. In contrast, diagenetic precipitation of Mn and Fe oxides occurs within suboxic pore water. Polymetallic manganese nodules are typically composed of alternating layers of these two types of precipitates, which can be distinguished texturally due to different growth processes. Hydrogenetic layers are typically composed of finely laminated layers which grade into laminated columnar structures, while layers that form within the sediment tend to have a dendritic habit. Additionally, it is common for the tops to be smooth and the bottom to be rough and coarse-grained.

In the modern oceans, sulfides form where reduced black smoker hydrothermal fluids mix with cool, oxidized ocean water (*Haymon and Kastner*, 1981; *Humphris et al.*, 1995; *Spiess et al.*, 1980). These massive sulfide deposits primarily form because sulfides and oxides are significantly less soluble in oxidized and cool ocean waters than in the reduced and hot hydrothermal vent waters (*Colín-García*, 2016). These minerals can form at the sediment-water interface in the presence of hydrothermal circulation, which rapidly falls off away from the vent axis *Colín-García* (2016). Away from hydrothermal activity, the sources of both reduced iron and sulfide come from microbial activity within the sediment, and the resulting geochemical gradients in Fe(II) and sulfide concentrations promote sulfide mineral precipitation within the sediment. In euxinic basins such as fjords within the North Sea, pyrite precipitation as framboids can happen in the water column

(*Neumann et al.*, 2005; *Roychoudhury et al.*, 2003; *Schieber*, 2011). However, larger pyrite structures are formed over thousands of years and are interpreted to have grown within the sediment (*Liu et al.*, 2020a; *Rickard*, 2012c; *Schieber*, 2002a). Thus, precipitation of sulfide minerals at the sediment-water interface is rare or at least rarely documented.

Iron sulfide mineral precipitation is limited by the saturation state of mackinawite, or FeS. Mackinawite precipitation occurs rapidly when its solubility constant is even slightly exceeded (*Rickard*, 2012a). The activities of iron and sulfur where this occurs are very close to the activities of iron and sulfur where pyrite precipitation begins (*Rickard*, 2012c); thus, mackinawite may potentially provide seed nuclei for pyrite nucleation and growth. Mackinawite forms first; however, it also rapidly converts to other more stable iron sulfides, especially pyrite, so that it is not preserved in ancient rocks (*Benning et al.*, 2000; *Rickard*, 2012c; *Wilkin and Barnes*, 1996). Pyrite in ancient rocks may therefore record the presence of iron and sulfide relatively close to the time that it precipitated but it may be a product of mackinawite recrystallization; in addition, later generations of pyrite may overprint primary geochemical signatures (*Fischer et al.*, 2014; *Meyer et al.*, 2017; *Slotznick et al.*, 2022; *Watanabe et al.*, 2009).

3.2.2. Archean Pyrite. Pyrite has been used as a record of ocean chemistry for decades due to the kinetics of its precipitation and relative stability to dissolution under most diagenetic and early metamorphic conditions (*Large et al.*, 2022). Bulk analyses of disseminated pyrite have been used to understand redox reactions in deep time, from the presence and activity of sulfate-reducing bacteria at the smallest scale (*Busigny et al.*, 2017; *Roerdink et al.*, 2012), to the redox state of a basin from trace elements within pyrite at the mesoscale (*Large et al.*, 2014), to the presence of oxygen in the atmosphere at the largest scale (*Farquhar and Wing*, 2003). These analyses rely on the assumption that disseminated pyrite forms early during diagenesis when the host sediment is in exchange with the surrounding water column, so that the pyrite's geochemistry accurately reflects the surrounding environment.

Sulfur is a biologically and redox active element. Biological sulfur cycling strongly fractionates sulfur isotopes, with sulfide tending to be isotopically lighter than sulfate. Because these processes occur at the microbial scale in poorly connected porewaters, sulfur isotopes can be significantly affected by local biological activity. Pyrite nodules, which can show more petrographic textures, can

be a target to better understand these biological processes and the timing of sulfide precipitation in Archean sediments (i.e., *Marin-Carbonne et al.* (2014); *Meyer et al.* (2017); *Partridge et al.* (2008); *Slotznick et al.* (2022).

3.2.3. Site Description. The Pilbara Craton is a segment of Paleoarchean continental crust in northwestern Western Australia (*French et al.*, 2015; *Hickman*, 2012). The 2.78|2.63 Gya Fortescue Group formed on the Pilbara Craton and is a predominantly volcanic succession, consisting mainly of a basaltic large igneous province. Deposition along a passive margin at the top of the Fortescue Group and throughout the overlying Hamersley Group resulted in the simultaneous deposition of the Carawine Formation (a shallow carbonate platform) and the Jeerinah Formation (a deep water shale). A meteorite impact at 2.63 Gya provides an instantaneous marker bed that stretches across these depositional environments (Chapter 1, *Simonson et al.* (2009a,b)).

The stratigraphy surrounding the meteorite impact has been previously studied (*Czaja et al.*, 2010; *Eigenbrode and Freeman*, 2006; *French et al.*, 2015; *Knoll and Beukes*, 2009; *Simonson et al.*, 2009b) and represents a platform to basin transition with deeper facies deposited below storm wave base with abundant microturbidites. Around the time of this meteorite impact, both the Carawine and Jeerinah formations contain extensive pyrite deposition that has been proposed to record an early euxinic interval (*Koehler et al.*, 2018; *Lyons et al.*, 2009; *Olson et al.*, 2019; *Ostrander et al.*, 2021). However, the source of sulfur to the basin at this time has not been conclusively identified. A high sulfur influx may have been due to an increase in oxidative weathering on land (*Koehler et al.*, 2018; *Ostrander et al.*, 2019, 2021, 2020) or to an increase in volcanism (*Olson et al.*, 2019). These scenarios are discussed in more detail in Chapter 1.

Cores AIDP2 and AIDP3 were drilled by the Agouron Drilling Project through the Fortescue and Hamersley Groups, specifically targeting organic-rich sedimentary rocks (*French et al.*, 2015). Core AIDP2 was collected less than 1 km from the older RHDH2A core and contains the same stratigraphy which has been previously studied (e.g. *Eigenbrode and Freeman* (2006); *Gregory et al.* (2019); *Ono et al.* (2003); *Williford et al.* (2016)). Prior work has not characterized the petrography of pyrite in this interval or connected pyrite precipitation to regional processes. Our work shows that some pyrite precipitated directly on the seafloor as nodules, a texture that is likely to preserve

the geochemistry of the seawater it precipitated from, in addition to precipitation of diverse other phases at different times (Chapter 2).

A prior study identified an enrichment in molybdenum in the shallower water AIDP2 and to a lesser degree in AIDP3 (*Olson et al.*, 2019). Additional iron speciation data in the same study identified periods of euxinic and ferruginous conditions. For AIDP2, the shales between 400 and 380 m have modest enrichments of reactive Fe primarily bound in carbonate rather than pyrite. This geochemistry is consistent with a ferruginous ocean. Between 380 and 340 m, the amount of highly reactive Fe increases, and that iron is predominately found within pyrite (*Olson et al.*, 2019). This increase in pyrite is accompanied with an increase in molybdenum and organic carbon. Above 340 m, pyrite content drops, and iron is predominately found within carbonate. For ADIP3, pyrite enrichment is observed in shales between 160 and 120 m. This pyrite enrichment is accompanied by an increase in molybdenum but not organic carbon. Shales between 120 and 105 m are enriched in iron-rich carbonates, consistent with ferruginous conditions. A larger magnitude of pyrite enrichment is observed between 105 and 65 m, which is not associated with an increase in molybdenum but is associated with a modest enrichment in organic carbon. The lower euxinic interval in AIDP3 may be equivalent to the euxinic interval in AIDP2; however, correlations between the shales in these cores has not been published.

3.3. Description of Pyrite Nodules

3.3.1. General Description. Pyrite nodules are elongate parallel to sedimentary layering and can be 0.5 to more than 27 mm wide. Some expand outward from a narrower base to a wider top (Figure 3.1), while others span the whole core width (Figure 3.1, 3.3). They tend to have bulbous tops and flatter bottoms, making them morphologically complex in three dimensions. Pyrite nodules tend to be found in shale layers where tabular aluminosilicate minerals are aligned along bedding planes in roughly defined sub-mm layers. These layers are in part defined by varying amounts of kerogen. Some laminations above and below the nodules contain rounded grains of calcite and quartz. Three samples from core AIDP- 2 and one from AIDP- 3 containing pyrite nodules were described in detail: AIDP2 362.63, AIDP2 342.86, AIDP2 336.53, and AIDP3 114.57. The sample names refer to the depth of sampling in the core.

AIDP2 362.63 is slightly below the peak euxinic interval (*Olson et al.*, 2019). This core section contains both a core-spanning 0.8 to 1.5 mm-thick layer of nodules and a core-spanning layer of euhedral and laminated pyrite that is 14 mm thick. The thick layer of pyrite is 5.8 mm below the pyrite nodule layer.

AIDP2 342.86 is within the peak euxinic interval (*Olson et al.*, 2019). The flat-lying nodule-bearing layer is 0 – 1.6 mm thick and is within a thick bed of shale. Nine millimeters lower in the sample, there is a round pyrite growth that is at least 8.5 mm tall and 10 mm wide, which deflects the immediately surrounding laminae.

AIDP2 336.53 is above the euxinic interval identified by *Olson et al.* (2019). Several highly pyritized layers are present in the sample (Figure 3.1; Chapter 2). One of these layers, which ranges from 0 to 1 mm thick in the plane of the thin section, occurs within an interval consisting of mostly clay minerals. This nodular layer is found ≥ 0.7 mm below a 1.5 mm graded bed composed of rounded carbonate grains, interpreted as a microturbidite. The bed fines upward from 0.2 mm diameter grains to finely laminated mud, and the surface upon which these largest grains were deposited truncates some of the laminations that onlap the nodules (Figure 3.3).

AIDP3 114.57 is within an interval described by *Olson et al.* (2019) as being molybdenum-poor and under ferruginous iron speciation conditions. Pyrite in this thin section is distributed in four discontinuous bands, 0 to 4 mm thick. The lowermost band contains pyrite nodules and is 0.1 to 0.4 mm thick.

3.3.2. Detailed Description. The nodule mineralogy is primarily pyrite, which is present in two forms: a lighter-colored, inclusion-poor pyrite and a darker-colored, inclusion-rich pyrite (see Chapter 2). The relationships between the nodules and the surrounding sediment as well as internal textures provide insights into the processes influencing nodule growth. The key relationships include: the onlap of detrital grains onto nodules; compaction below nodules; the distributions of inclusion-rich and inclusion-poor pyrite; and the distribution of other minerals within the nodules.

3.3.2.1. *Onlap Relationships.* Bulbous, inclusion-rich pyrite defines the topography at the top of nodules, creating highs and lows that deflect laminae in the shale. Laminae tend to be flat-lying above nodule highs and in lows and are subhorizontally to subvertically oriented where the underlying nodule top slopes (Figures 3.1, 3.2). Laminae tend to flatten upward by 2 mm above

the top of the nodules; however, in one instance, subhorizontal laminae are truncated by a 1.5 mm thick graded bed (Figure 3.2). This graded bed is interpreted as a microturbidite that eroded the shale layers on top of a nodule, indicating that the topographic influence of the pyrite nodule was syndepositional.

Detrital laminae thicken between highs on the tops of nodules as a result of increased accumulation of clay minerals and rounded calcite in the lows. This geometry suggests that there was locally more accommodation space in the topographic depressions created by the pyrite nodules. In contrast, the kerogen laminae have a more consistent thickness between highs and lows, although kerogen laminae are slightly thinner above topographic highs. This geometry is consistent with kerogen-rich layers forming from microbial mats that experienced small amounts of differential compaction.

3.3.2.2. *Compactional Distortion of Laminae at the Bottom of Nodules.* The bottoms of nodules, although typically flat, have some protrusions that truncate the underlying laminae. The thickness of shale layers is the same whether found below a downward protrusion or not. This geometry suggests a uniform depositional thickness of shale minerals, with deformation of the laminae primarily reflecting compaction.

3.3.2.3. *Inclusion-Rich Pyrite.* The nodules are composed primarily of pyrite that contains abundant $< 1 - 2$ µm sized inclusions composed of aluminosilicate minerals and kerogen. This inclusion-rich pyrite texture is distributed pervasively throughout nodules, with some faint banding and clustering of inclusions occasionally observed (Figure 3.1C). Where pyrite crystals can be observed, they tend to be anhedral and 2—8 µm in diameter. Inclusions are equant to low-aspect ratio oval. The aluminosilicate minerals within inclusions are often randomly aligned (Figure 3.1E, I). There is a higher concentration of organic carbon in the inclusions within the pyrite versus in the shale around the nodule. Additionally, the kerogen inclusions in the pyrite nodule further suggest a biological presence during pyrite precipitation (*Duverger et al.*, 2021; *Picard et al.*, 2016, 2018).

3.3.2.4. *Carbonate and Silica Cements.* The interiors and edges of nodules contain areas composed of quartz and carbonate, which are at least 100 µm across. These cements are often found under overhangs composed of inclusion-rich pyrite or may be surrounded by inclusion-rich pyrite.

The carbonate consists almost entirely of calcite with minor dolomite . Calcite crystals are euhedral and equant in habit, with crystal sizes ranging from 10 – 50 µm. Quartz crystals tend to be anhedral and interfinger with calcite as small, 5 – 10 mm equant inclusions and borders of calcite or as larger 20 – 50 um rounded calcite and silica areas, which may have cores of organic carbon (Figure 3.1E, I).

3.3.2.5. *Inclusion-Poor Pyrite.* Inclusion-poor pyrite has a euhedral to subhedral crystal habit with long (10 – 100 µm) crystal faces. The internal parts of this phase do not contain the organic and aluminosilicate mineral inclusions characteristic of inclusion-rich pyrite. Although the interiors of inclusion-poor pyrite bodies do not have inclusions, some inclusions can be found at the borders between inclusion-rich and inclusion-poor pyrite. The inclusion-poor pyrite bodies within a larger pyrite nodule may be shaped like other voids filled with carbonate cement, or it may be bean-shaped (see Chapter 2). Inclusion-poor pyrite may incompletely to completely replace carbonate cements. When pyrite incompletely replaces carbonate, prismatic pyrite crystal faces grow inward into the carbonate.

Inclusion-poor pyrite is lighter colored in reflected light than inclusion-rich pyrite and has a higher electron density in BSE images (Chapter 2) however, it was not possible to measure elemental differences with an electron microprobe between the higher- and lower-electron density pyrite. The color and textural contrast between these phases mean that they can be distinguished visually on the microscope and on photomicrographs with machine learning.

3.3.3. Growth Model for Pyrite Nodules. The pyrite nodules described above have a proposed genetic origin at or immediately below the sediment-water interface. In the model proposed here, pyrite growth initiated on the sea floor at the sediment or mat surface. Pyrite continued to grow where the crystals were exposed to seawater. Clay minerals and organic matter were deposited on parts of the pyrite nodule, stopping its growth in these areas if the flux was high enough. Lower and varying amounts of clay minerals and organic matter flux created laminations in the pyrite nodules.

Pyrite precipitation continued to the sides of the area where sedimentation caused precipitation to stop, and detrital sediments continued to accumulate in the low areas with no pyrite growth. To the sides of these topographic lows, pyrite continued to grow upwards creating relative highs.

When pyrite continued to grow both upward and laterally, it created overhangs that partially or completely covered the lows where pyrite growth had stopped. The overhanging areas created water-filled voids with sediment on their bottom surfaces. If these areas were not fully enclosed, additional sediment may have settled under the overhangs. Clay minerals near overhangs and voids created by pyrite growth were incorporated into pyrite nodules prior to compaction, as evidenced by the random orientation of clay minerals within inclusions within pyrite when compared to the compressed and aligned clay minerals in the surrounding shale.

Where not buried by sediment, pyrite continued to grow upwards, sometimes creating stromatolite-like structures. Growth continued until conditions changed either in the water chemistry or the sedimentation rate. The chemistry of the water or microbial activity could have changed to no longer favor pyrite precipitation, or sedimentation may have outpaced pyrite precipitation and completely covered the top of the nodule. The difference in texture between the top and bottom of the pyrite nodules suggests that they grew in a geochemical gradient, with different conditions for growth of pyrite between the top and bottom of the nodule.

Following burial of the nodule, compaction of the surrounding sediment continued. Where voids created by pyrite growth were incompletely closed off from the surrounding sediment, compaction forced clay minerals into overhangs. Enclosed voids were filled with carbonate and lesser silica cements. In other voids, carbonate precipitation occurred at the top of the voids as detrital clay minerals settled to the bottoms of voids and compacted due to gravity.

Carbonate that filled the voids was then partially replaced by later-stage inclusion-poor pyrite, which grew in from the margins of the voids. This inclusion-poor pyrite may also have nucleated within shale inclusions, displacing remnant shale minerals to the edges of the inclusion-poor pyrite.

3.4. Discussion of Seafloor Pyrite Precipitation

The precipitation of pyrite on the seafloor is either rare or poorly documented in Earth history. However, comparison with manganese nodules can help guide interpretations of the large scale environmental conditions allowing its formation as well as local geochemical implications when seafloor pyrite precipitation occurred. These considerations help place the 2.63 Gya seafloor pyrite nodules into context.

3.4.1. Comparison with Manganese Nodules. Growth of Archean pyrite nodules may be partially analogous to modern polymetallic manganese nodules, which grow at the sediment-water interface driven by a geochemical gradient created by manganese-oxidizing bacteria. Manganese nodules show differences in morphology between the top and bottom much like that observed in pyrite nodules. This similarity suggests a potential geochemical gradient across the Archean sediment-water interface. While the morphologies of manganese nodules are very different from pyrite nodules due to the different crystallographic behaviors of the early-forming mineral precipitates, the growth processes may still produce some similar features.

Manganese nodules tend to have lots of pore spaces that remain open and allow for the circulation of seawater through the nodule (*Kuhn et al.*, 2017). These pores can be analogous to the calcite-filled voids within Archean pyrite nodules, suggesting a possible role for circulating seawater that can be tested with isotopic analyses. Additionally, the columnar form of some diagenetic manganese nodule layers is caused by bottom currents removing sediment and delivering ions to the manganese nodule surface (*Kuhn et al.*, 2017). A similar process may have promoted the growth of the observed topographic highs on pyrite nodules. The bulbous to columnar tops of both pyrite and manganese nodules is promoted by this type of differential sedimentation.

3.4.2. Large-Scale Environmental Considerations. The large amounts of pyrite precipitating at the sea floor during the interval from $2.65 - 2.63$ Gya points to an increase in flux of sulfur to the environment relative to the Archean background (*Izon et al.*, 2015, 2017, 2022; *Knoll and Beukes*, 2009). The iron for pyrite precipitation is thought to come from a hydrothermal source further off-shore (*Eroglu et al.*, 2018; *Thibon et al.*, 2019). Iron isotopes in Neoarchean pyrite show that iron was not quantitatively removed by pyrite precipitation, leading to an interpretation that the Archean oceans had relatively high concentrations of dissolved Fe(II) (*Johnson et al.*, 2008). If these iron isotope trends are found in the 2.63 Ga euxinic interval, particularly within pyrite nodules, it would be consistent with an abundance of Fe(II) in seawater and the delivery of sulfate that is locally reduced at the sediment-water interface to form pyrite nodules. In this case, an increase in sulfate supply would be a primary cause of the euxinic interval.

An increased flux of sulfur could have come from an increase in volcanic activity, which could deliver SO_2 gas to the oceans and atmosphere along with its photochemical disproportionation

products, including sulfate and elemental sulfur. Alternatively, an increase in sulfate could come into this continental ramp environment from runoff created by oxidative weathering of continental basalts (*Lalonde and Konhauser*, 2015; *Wilmeth et al.*, 2019, 2022). These two sources of sulfate would have a distinct quadruple isotope signature from each other. Sulfur from volcanic emissions, processed in the atmosphere would show non-zero $\Delta^{33}S$ and $\Delta^{36}S$. In contrast, oxidation of volcanic pyrite during weathering would have a $\Delta^{33}S$ and $\Delta^{36}S$ close to zero (*Farquhar and Wing*, 2003; *Ono et al.*, 2009a,b). A mix of atmospheric and weathering sulfur sources is also possible, which could provide significant variability in local isotopic compositions.

Identifying pyrite that precipitated directly from seawater, such as the nodules described here, provides targets for in situ isotope analysis. Results may reveal heterogeneity in sedimentary sulfide sources as well as several generations of pyrite growth, possibly with different sources of sulfur for each. The interpreted hydrogenetic growth of pyrite nodules makes them an interesting target for better understanding the sources of sulfur that caused the 2.63 Gya euxinic interval.

3.4.3. Local Geochemical Implications. Pyrite precipitating at the sea floor can be an excellent target geochemical and isotopic studies aiming to understand ancient environments. In particular, the presence of pyrite precipitation at the sediment-water interface points to high enough concentrations of both iron and sulfur to facilitate pyrite precipitation. In the modern ocean, pyrite tends to precipitate in anoxic sediments under oxic and sulfate-rich water columns, or in euxinic settings where pyrite can precipitate in the water column in the presence of dissolved iron. Traditionally, sulfate in the Archean ocean is thought to be at low concentration due to little oxidative weathering (*Crowe et al.*, 2014; *Paris et al.*, 2014). Concentrations of sulfate may have been kept low due to low rates of sulfide oxidation as well as quantitative reduction of sulfate by sulfate-reducing bacteria . During the precipitation of pyrite nodules, sulfate may have still been low because it was removed from seawater by a high rate of sulfate reduction followed by pyrite precipitation.

One possible driver of a geochemical gradient in anoxic sediments could be the different redox potentials of methane reduction and sulfate oxidation. The redox potentials of methane and sulfate reduction/sulfide oxidation are different, and these microbially mediated reactions take place in different places in modern sediments (*Liu et al.*, 2020b). These reactions could have created a

redox and chemical gradient in Archean sediments that could drive pyrite nodule precipitation at the sediment-water interface. There is evidence for methane and sulfur cycling through this period of the Archean (*Eigenbrode and Freeman*, 2006; *Izon et al.*, 2015, 2017, 2022; *Liu et al.*, 2019), and pyrite nodules could represent a fossil microbially driven geochemical gradient.

A potential pyrite nodule from the Jeerinah Formation was analyzed for trace elements and $\delta^{34}S$ (*Gregory et al.*, 2019). The observed geochemical signatures were relatively uniform throughout the nodule, which is consistent with the author's interpretation that the nodule formed relatively rapidly due to high levels of nucleation in pore waters with high concentrations of Fe(II) and H_2S. This interpretation was supported by the observation that the analyzed nodule is composed of many small ($10-30$ µm diameter), interlocked pyrite grains. The internal texture of pyrite nodules in our study could not be determined, and a larger scale description of the pyrite body in *Gregory et al.* (2019) was not provided, limiting the direct comparison. However, this emphasizes the clear need for petrographically constrained observations of pyrite in this interval.

3.5. Conclusions

Archean pyrite nodules have textures that suggest hydrogenetic precipitation from Archean seawater. Because these features have been identified along a depth gradient, roughly contemporaneous hydrogenetic precipitates could be used to understand how sulfur cycling operated in different environments. The identification of this novel texture with specific geochemical implications in these ancient sediments points to the continued importance of petrography in understanding chemical precipitates that are analyzed with geochemistry to understand the distant past. These features should be targeted for future in situ geochemical analyses to understand the Archean sulfur cycle.

3.6. Methods

Cores were collected using methods described in *French et al.* (2015) and were split in half, with one half of each shipped to the United States. The US portions of the cores was logged and sampled by D. Sumner to obtain representative petrographic textures for pyrite within euxinic intervals. Thin sections were cut to 30 and 100 µm and polished with Buehler MicroPolish™ Alumina 0.3 µm, which has a basic pH. Textures representing possible sea floor pyrite nodules were identified based on sample inspection at the slide scale and with reflected light petrography.

Large mosaic images were collected in a grid using a Nikon SMZ25 with an automated stage and single-point coaxial reflected light illumination. The focus was adjusted manually every five frames since reflected light has only a single plane of focus. Large mosaics were stitched with the Nikon Advanced Research Best Path algorithm. Pairwise images were stitched with the ImageJ Stitcher program (*Preibisch et al.*, 2009).

Petrographic phases in the image mosaics were categorized using the software package Ilastik (*Berg et al.*, 2019). In brief, this program uses a Random Forest algorithm to classify pixels based on their probability of belong to a labelled training set. Training is done by interactively labelling pixels as belonging to each specific phase until a suitable fit is observed. One component frame of the mosaic of AIDP2 362.63 was used to train the algorithm with 5 training labels: shale, carbonate, epoxy, inclusion-poor pyrite, and inclusion-rich pyrite. The two phases of pyrite were distinguished by color and the number of inclusions per unit area in the image. The algorithm was able to separate out these phases in both the training data and in the larger mosaic.

Element maps of selected regions of interest were collected with the Hitachi SU 3500 VP-SEM with an Oxford Instruments X-Max^{N} 150 mm^2 silicon drift energy dispersive spectroscopy system at Jet Propulsion Laboratory's Astrobiogeochemistry Laboratory. EDS maps were generated on this system, as well as with the Cameca SX-100 electron microprobe at UC Davis Earth and Planetary Sciences.

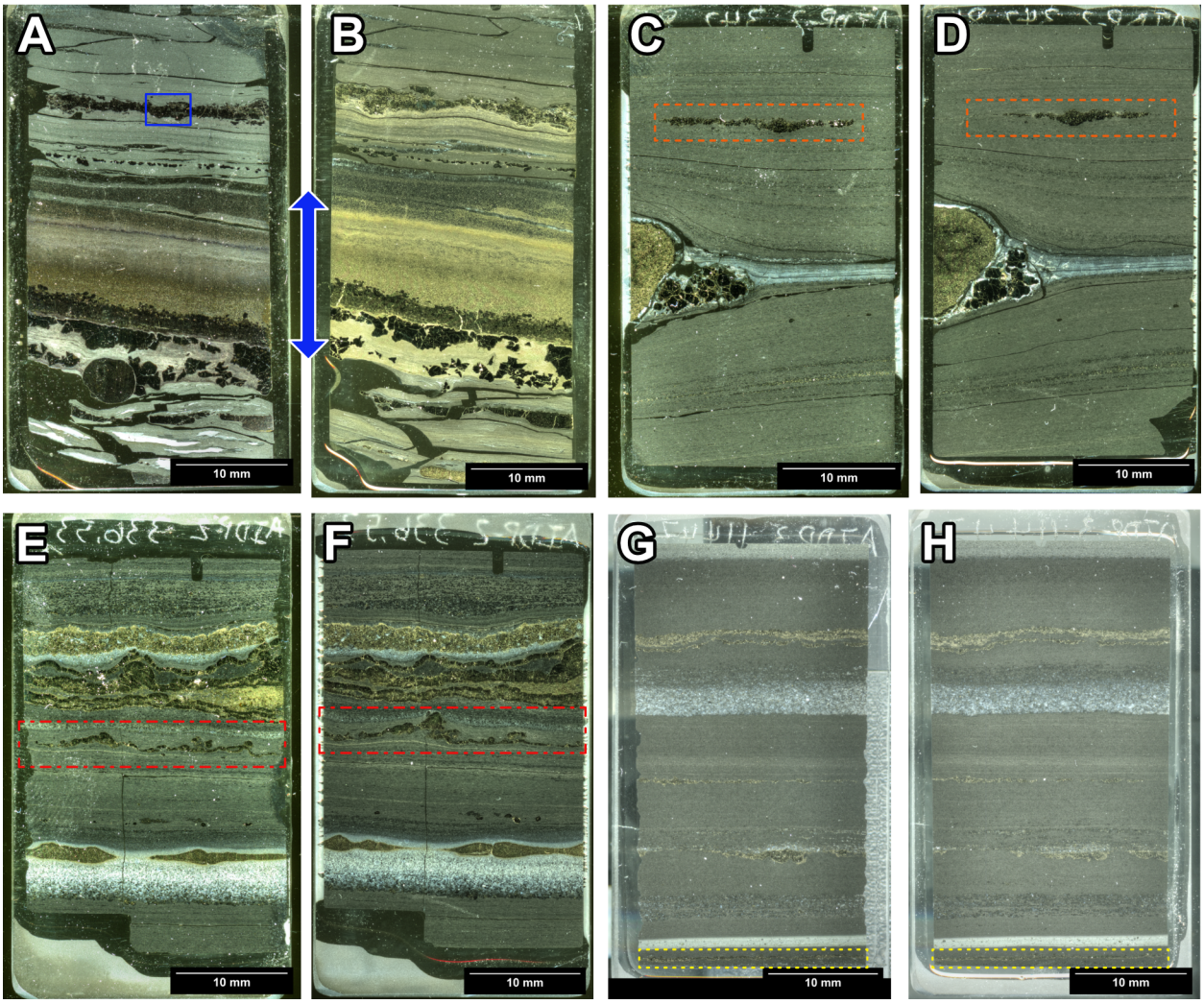

Figure 3.1. Reflected light full slide scans of thin sections. A, B: AIDP2 362.63 30 µm (A) and 100 µm thick polished thin sections. (B). The nodule area shown in figure 3 is highlighted in blue. C, D: AIDP2 342.86 30 µm (C) and 100 µm thick polished thin sections (D). The nodule area show in figure 4 is highlighted in orange. E, F: AIDP2 336.53 30 µm (E) and 100 µm (F) thick polished thin sections. The nodule area is highlighted in red. G, H: AIDP3 114.57 30 µm (G) and 100 µm (H) thick polished thin sections. The nodule area is highlighted in yellow.

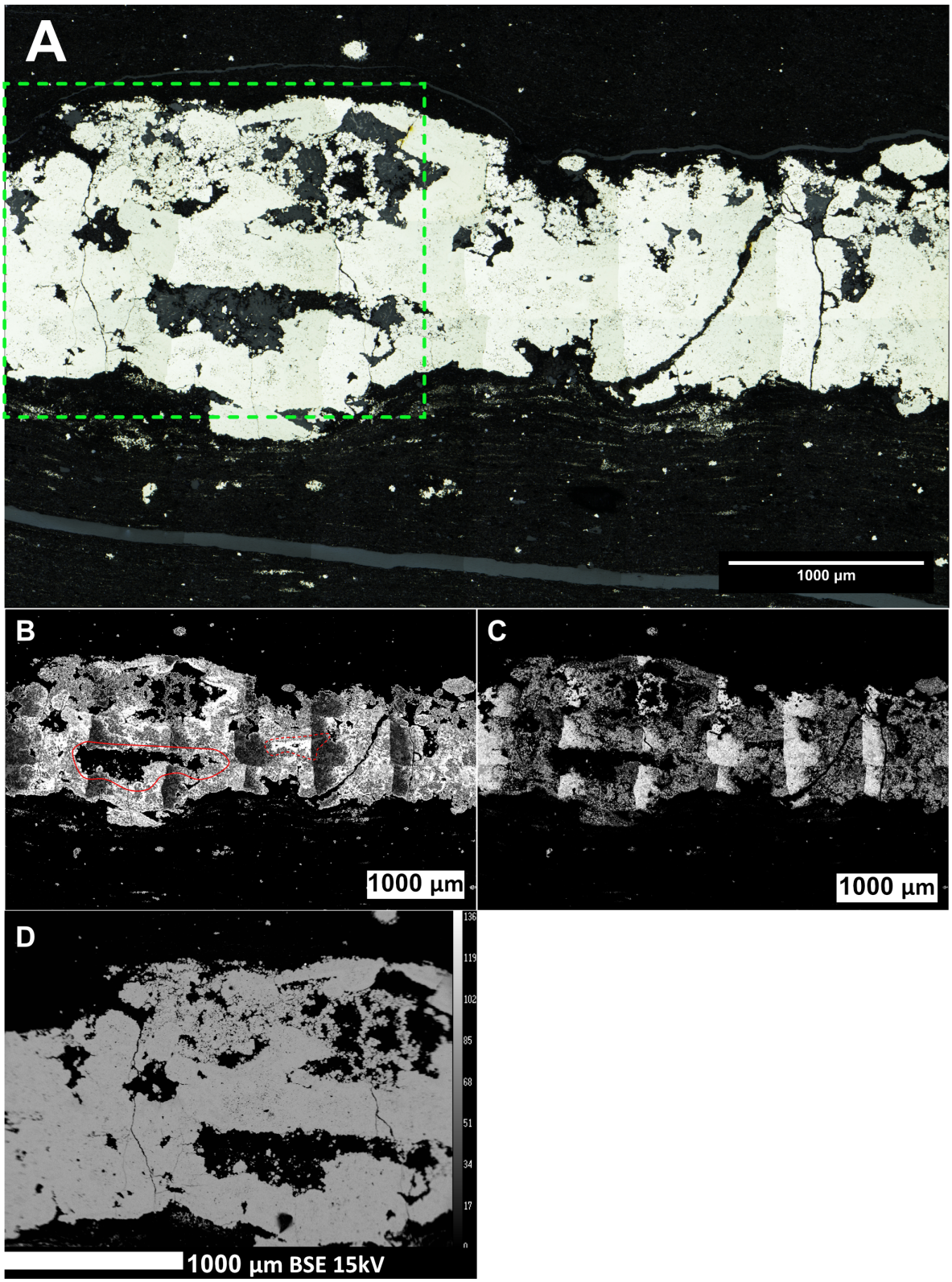
A
1000 µm
B
1000 µm
C
1000 µm
D
136
119
102
85
68
51
34
17
0
1000 µm BSE 15kV

Figure 3.1. Representative pyrite nodule from AIDP2 362.63 30 µm thick polished thin section. A: AIDP2 362.63 composite image in reflected light. Box shows the area in D. B: Inclusion-poor pyrite identified with Ilastik. Brighter pixels represent a greater probability that a pixel represents inclusion-poor pyrite. The grid pattern is an artifact of the stitching process. The similarity in shape between a calcite cement (solid outline) and inclusion-poor pyrite (dashed line) is noted in the outlined areas. C: Inclusion-rich pyrite identified with Ilastik. The faint banding of shale inclusions within inclusion-rich pyrite is observable in this image. D: BSE image of the area outlined in A.

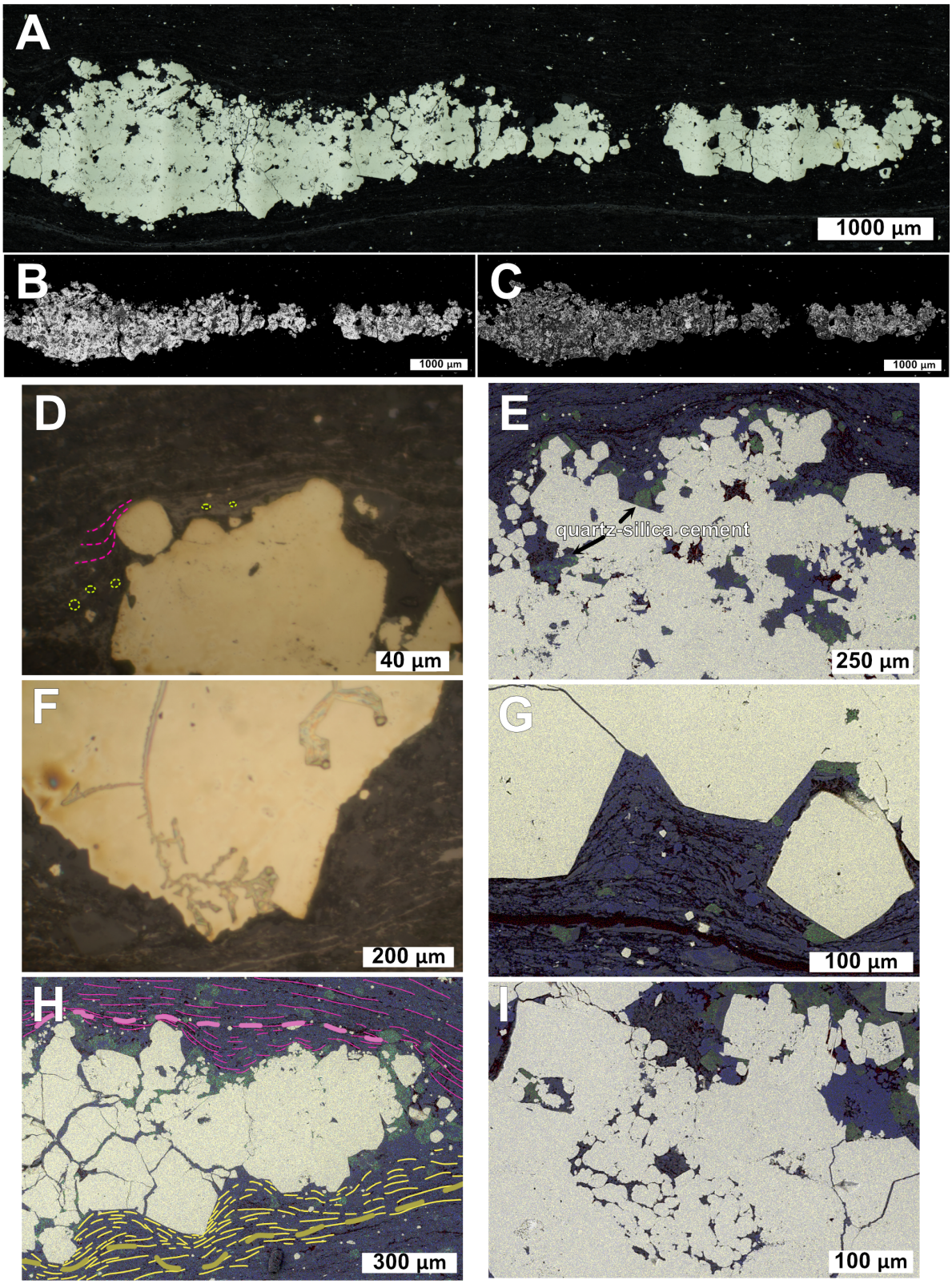
A
1000 µm
B
1000 µm
C
1000 µm
D
40 µm
E
quartz-silica cement
250 µm
F
200 µm
G
100 µm
H
300 µm
I
100 µm

Figure 3.1. : Representative pyrite nodule from AIDP2 342.86 30 µm thick polished thin section A: Nodule composite in reflected light. B: Inclusion-poor pyrite identified with ilastik. C: Inclusion-rich pyrite identified with ilastik. D: Texture on top of a nodule showing thicker accumulation of dark gray detrital shale minerals inside of topographic lows when compared to topographic highs. The separation of lighter gray layers by shale layers is highlighted in pink. Rounded grains of detrital calcite are outlined in yellow. E: Onlap texture on top of the nodule, showing relative changes in thickness of detrital clay mineral layers with topography. Also, the lack of alignment of shale minerals within kerogen-enriched inclusions can be seen in the center of the nodule. Quartz and silica cements are marked in one area. F: Euhedral pyrite on the bottom of the nodule, showing compression and cross-cutting of shale layers. G: Euhedral pyrite on the bottom of the nodule, showing compression of kerogen-rich layers (red) and uniform thickness of shale layers (blue). Tabular clay minerals have been deformed and bent due to compressional forces. H: Sketch showing the different relationships of contorted kerogen laminae to nodule morphology based on position relative to a nodule imaged using EDS. Onlapping kerogen layers (pink) and compactionally distorted layers (yellow) are traced, with one continuous layer for each traced with a thicker line. I: Inclusions within the nodule are enriched in organic carbon. Colors throughout the text on electron maps are: Red = C, Blue = Si, Green = Ca, Yellow = S, base image (black and white) = EDS.

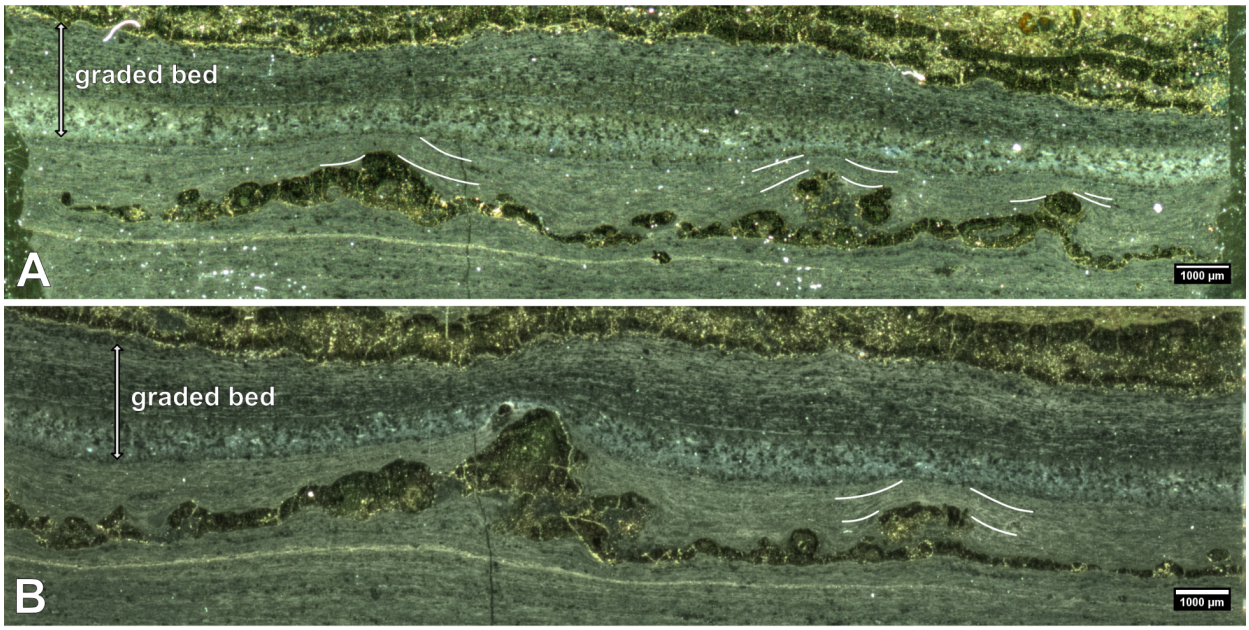

Figure 3.2. Relationship between nodules and microturbidites. AIDP2 336.53 30 µm (A) and 100 µm (B) thick polished thin sections, reflected light scan. Semicontinuous layer of pyrite nodules, showing laminae (white lines) truncated by overlying graded bed.

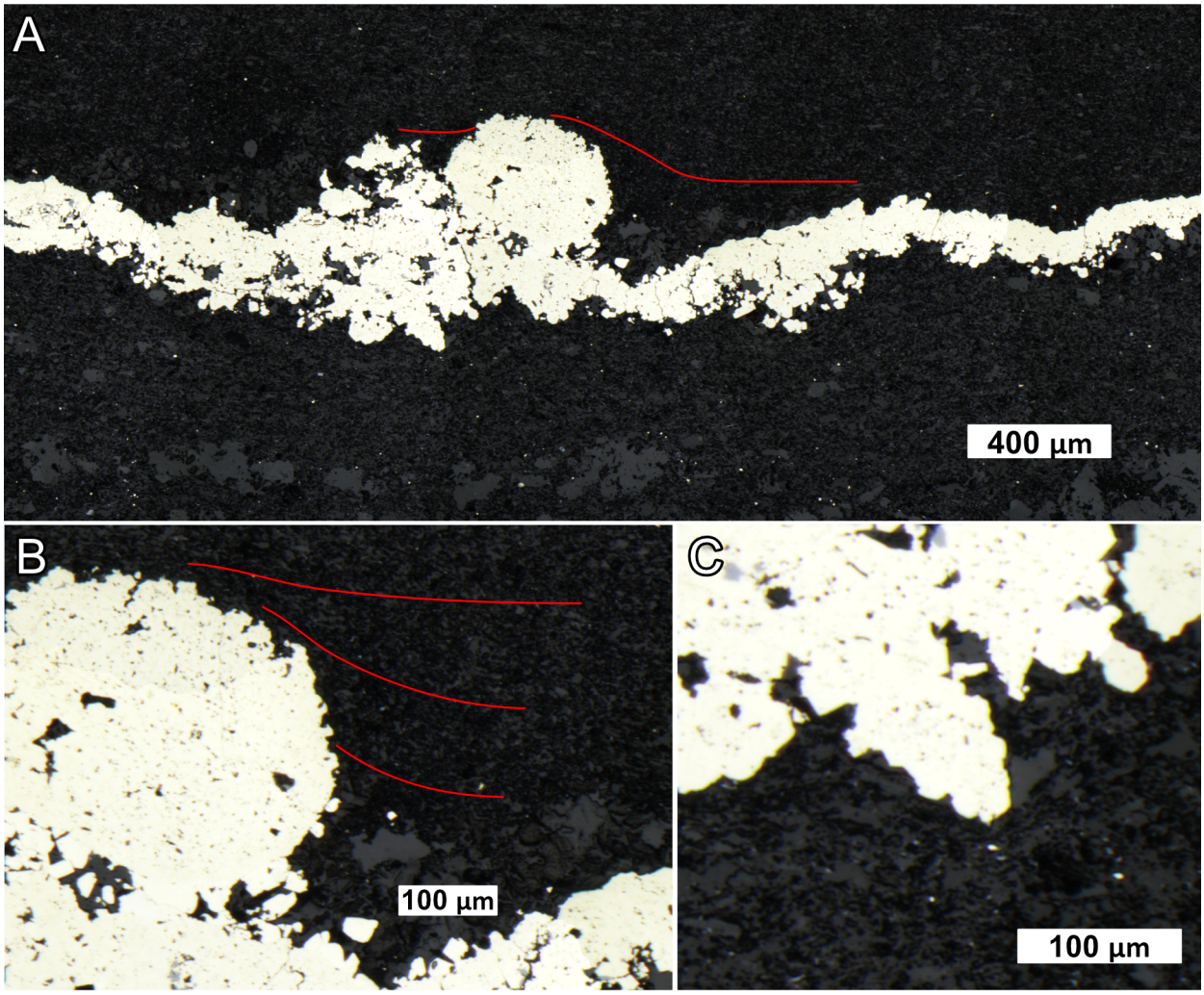

Figure 3.3. Representative pyrite nodule from AIDP3 114.57 30 µm thick polished thin section. A: Nodule from AIDP3 114.57 30 µm thick polished thin section in reflected light. Red lines show onlap geometry of laminae against rounded part of nodule. B: Shale laminae have onlap geometry (red lines) onto the top of the rounded part of the nodule, which consists mostly of inclusion-rich pyrite at the top. Due to less clear lamination than in AIDP2 samples, onlap is more difficult to see in this sample. Additionally, post-burial precipitation of pyrite further obscures seafloor nodule growth textures. C: Inclusion-poor pyrite penetrates into the sediment below during compaction.

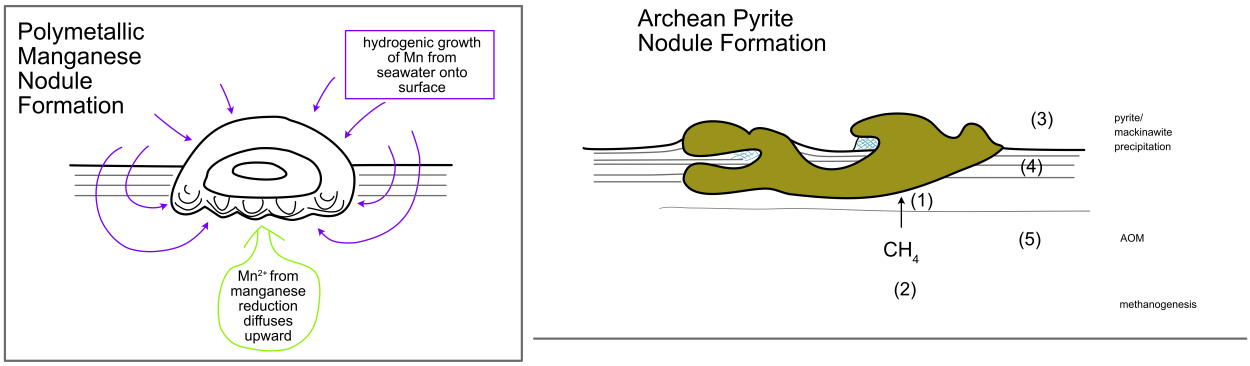

(1)	sulfate reduction / anaerobic methane oxidation (AOM)	$CH_4 + {SO_4}^{2-} \longrightarrow {HCO_3}^- + HS^- + H_2O$
(2)	methanogenesis	$CO_2 + 4\,H_2 \longrightarrow CH_4 + 2\,H_2O$
(3)	mackinawite formation	$Fe^{2+} + HS^- \longrightarrow [FeS]_m + H^+$
(4)	pyrite formation	$[FeS]_m + H_2S \longrightarrow FeS_2py + H_2$
(5)	hydrogenotrophy	$2\,H^+ + {SO_4}^{2-} + 4\,H_2 \longrightarrow H_2S + 4\,H_2O$

Figure 3.4. Growth model of polymetallic manganese nodules and Archean pyrite nodules. Proposed redox reactions and their location along a redox gradient are shown. Mn nodule figure adapted from *Kuhn et al.* (2017)

Bibliography

Anbar, A. D., et al., A Whiff of Oxygen Before the Great Oxidation Event?, *Science*, *317*(5846), 1903–1906, doi:10.1126/science.1140325, 2007.

Araújo, J. C. S., and L. M. Lobato, Depositional model for banded iron formation host to gold in the Archean Rio das Velhas greenstone belt, Brazil, based on geochemistry and LA-ICP-MS magnetite analyses, *Journal of South American Earth Sciences*, *94*, 102,205, doi:10.1016/j.jsames.2019.05.021, 2019.

Bannister, F. A., The distinction of pyrite from marcasite in nodular growths, *Mineralogical Magazine and Journal of the Mineralogical Society*, *23*(138), 179–187, doi:10.1180/minmag.1932.023.138.04, 1932.

Benning, L. G., R. T. Wilkin, and H. L. Barnes, Reaction pathways in the Fe–S system below 100°C, *Chemical Geology*, *167*(1), 25–51, doi:10.1016/S0009-2541(99)00198-9, 2000.

Berg, S., et al., ilastik: interactive machine learning for (bio)image analysis, *Nature Methods*, *16*(12), 1226–1232, doi:10.1038/s41592-019-0582-9, number: 12 Publisher: Nature Publishing Group, 2019.

Bosco-Santos, A., W. P. Gilhooly, F. Fouskas, W. Fabricio-Silva, and E. P. Oliveira, Euxinia in the Neoarchean: The starting point for early oxygenation in a Brazilian Craton, *Precambrian Research*, *341*, 105,655, doi:10.1016/j.precamres.2020.105655, 2020.

Busigny, V., J. Marin-Carbonne, E. Muller, P. Cartigny, C. Rollion-Bard, N. Assayag, and P. Philippot, Iron and sulfur isotope constraints on redox conditions associated with the 3.2Ga barite deposits of the Mapepe Formation (Barberton Greenstone Belt, South Africa), *Geochimica et Cosmochimica Acta*, *210*, 247–266, doi:10.1016/j.gca.2017.05.002, 2017.

Colín-García, M., Hydrothermal vents and prebiotic chemistry: a review, *Boletín de la Sociedad Geológica Mexicana*, *68*(3), 599–620, doi:10.18268/BSGM2016v68n3a13, 2016.

Crowe, S. A., et al., Sulfate was a trace constituent of Archean seawater, *Science*, *346*(6210), 735, doi:10.1126/science.1258966, 2014.

Cui, H., K. Kitajima, M. J. Spicuzza, J. H. Fournelle, A. Ishida, P. E. Brown, and J. W. Valley, Searching for the Great Oxidation Event in North America: A Reappraisal of the Huronian Supergroup by SIMS Sulfur Four-Isotope Analysis, *Astrobiology*, *18*(5), 519–538, doi:10.1089/ast.2017.1722, 2018.

Czaja, A. D., C. M. Johnson, B. L. Beard, J. L. Eigenbrode, K. H. Freeman, and K. E. Yamaguchi, Iron and carbon isotope evidence for ecosystem and environmental diversity in the 2.7 to 2.5Ga Hamersley Province, Western Australia, *Earth and Planetary Science Letters*, *292*(1), 170–180, doi:10.1016/j.epsl.2010.01.032, 2010.

Duan, Y., A. D. Anbar, G. L. Arnold, T. W. Lyons, G. W. Gordon, and B. Kendall, Molybdenum isotope evidence for mild environmental oxygenation before the Great Oxidation Event, *Geochimica et Cosmochimica Acta*, *74*(23), 6655–6668, doi:10.1016/j.gca.2010.08.035, 2010.

Duverger, A., S. Bernard, J.-C. Viennet, J. Miot, and V. Busigny, Formation of Pyrite Spherules From Mixtures of Biogenic FeS and Organic Compounds During Experimental Diagenesis, *Geochemistry, Geophysics, Geosystems*, *22*(10), e2021GC010,056, doi:10.1029/2021GC010056, _eprint: https://onlinelibrary.wiley.com/doi/pdf/10.1029/2021GC010056, 2021.

Eigenbrode, J. L., and K. H. Freeman, Late Archean rise of aerobic microbial ecosystems, *Proceedings of the National Academy of Sciences*, *103*(43), 15,759–15,764, doi:10.1073/pnas.0607540103, 2006.

Eroglu, S., R. Schoenberg, S. Pascarelli, N. J. Beukes, I. C. Kleinhanns, and E. D. Swanner, Open ocean vs. continentally-derived iron cycles along the Neoarchean Campbellrand-Malmani Carbonate platform, South Africa, *American Journal of Science*, *318*(4), 367–408, doi:10.2475/04.2018.01, 2018.

Farquhar, J., and B. A. Wing, Multiple sulfur isotopes and the evolution of the atmosphere, *Earth and Planetary Science Letters*, *213*(1), 1–13, doi:10.1016/S0012-821X(03)00296-6, 2003.

Farquhar, J., H. Bao, and M. Thiemens, Atmospheric Influence of Earth's Earliest Sulfur Cycle, *Science*, *289*(5480), 756–758, 2000.

Farquhar, J., J. Savarino, S. Airieau, and M. H. Thiemens, Observation of wavelength-sensitive mass-independent sulfur isotope effects during SO2 photolysis: Implications for the early atmosphere, *Journal of Geophysical Research: Planets*, *106*(E12), 32,829–32,839, doi:10.1029/2000JE001437, 2001.

Farquhar, J., J. Cliff, A. L. Zerkle, A. Kamyshny, S. W. Poulton, M. Claire, D. Adams, and B. Harms, Pathways for Neoarchean pyrite formation constrained by mass-independent sulfur isotopes, *Proceedings of the National Academy of Sciences*, *110*(44), 17,638–17,643, 2013.

Fischer, W. W., D. A. Fike, J. E. Johnson, T. D. Raub, Y. Guan, J. L. Kirschvink, and J. M. Eiler, SQUID–SIMS is a useful approach to uncover primary signals in the Archean sulfur cycle, *Proceedings of the National Academy of Sciences*, *111*(15), 5468–5473, doi:10.1073/pnas.1322577111, 2014.

French, K. L., et al., Reappraisal of hydrocarbon biomarkers in Archean rocks, *Proceedings of the National Academy of Sciences*, *112*(19), 5915–5920, doi:10.1073/pnas.1419563112, 2015.

G. Harmandas, N., E. Navarro Fernandez, and P. Koutsoukos, *Crystal Growth of Pyrite in Aqueous Solutions. Inhibition by Organophosphorus Compounds*, vol. 14, doi:10.1021/la970354c, 1998.

Glass, B. P., and B. M. Simonson, Spherule Layers Near the Archean-Proterozoic Boundary, in *Distal Impact Ejecta Layers*, Impact Studies, Springer, Berlin, Heidelberg, 2013.

Glikson, A., Asteroid impact ejecta units overlain by iron-rich sediments in 3.5–2.4 Ga terrains, Pilbara and Kaapvaal cratons: Accidental or cause–effect relationships?, *Earth and Planetary Science Letters*, *246*(3), 149–160, doi:10.1016/j.epsl.2006.03.045, 2006.

Glikson, A., Archaean asteroid impacts, banded iron formations and MIF-S anomalies: A discussion, *Icarus*, *207*(1), 39–44, doi:10.1016/j.icarus.2009.11.024, 2010.

Glikson, A. Y., Field evidence of Eros-scale asteroids and impact-forcing of Precambrian geodynamic episodes, Kaapvaal (South Africa) and Pilbara (Western Australia) Cratons, *Earth and Planetary Science Letters*, *267*(3), 558–570, doi:10.1016/j.epsl.2007.12.007, 2008.

Gregory, D., et al., The formation mechanisms of sedimentary pyrite nodules determined by trace element and sulfur isotope microanalysis, *Geochimica et Cosmochimica Acta*, *259*, 53–68, doi:10.1016/j.gca.2019.05.035, 2019.

Gregory, D. D., R. R. Large, J. A. Halpin, J. A. Steadman, A. H. Hickman, T. R. Ireland, and P. Holden, The chemical conditions of the late Archean Hamersley basin inferred from whole rock and pyrite geochemistry with Δ33S and δ34S isotope analyses, *Geochimica et Cosmochimica Acta*, *149*, 223–250, doi:10.1016/j.gca.2014.10.023, 2015.

Hassler, S. W., and B. M. Simonson, The Sedimentary Record of Extraterrestrial Impacts in Deep-Shelf Environments: Evidence from the Early Precambrian, *The Journal of Geology*, *109*(1), 1–19, doi:https://doi.org/10.1086/317958, 2001.

Hassler, S. W., H. F. Robey, and B. M. Simonson, Bedforms produced by impact-generated tsunami, 2.6Ga Hamersley basin, Western Australia, *Sedimentary Geology*, *135*(1), 283–294, doi:10.1016/S0037-0738(00)00078-6, 2000.

Havig, J. R., C. Grettenberger, and T. L. Hamilton, Geochemistry and microbial community composition across a range of acid mine drainage impact and implications for the Neoarchean-Paleoproterozoic transition: AMD Sites as Possible Neoarchean Analogs, *Journal of Geophysical Research: Biogeosciences*, *122*(6), 1404–1422, doi:10.1002/2016JG003594, 2017.

Haymon, R. M., and M. Kastner, Hot spring deposits on the East Pacific Rise at 21°N: preliminary description of mineralogy and genesis, *Earth and Planetary Science Letters*, *53*, 363–381, doi:10.1016/0012-821X(81)90041-8, aDS Bibcode: 1981E&PSL..53..363H, 1981.

Heard, A. W., N. Dauphas, R. Guilbaud, O. J. Rouxel, I. B. Butler, N. X. Nie, and A. Bekker, Triple iron isotope constraints on the role of ocean iron sinks in early atmospheric oxygenation, *Science*, doi:10.1126/science.aaz8821, publisher: American Association for the Advancement of Science, 2020.

Hickman, A. H., Review of the Pilbara Craton and Fortescue Basin, Western Australia: Crustal evolution providing environments for early life, *Island Arc*, *21*(1), 1–31, doi:10.1111/j.1440-1738.2011.00783.x, _eprint: https://onlinelibrary.wiley.com/doi/pdf/10.1111/j.1440-1738.2011.00783.x, 2012.

Humphris, S. E., R. A. Zierenberg, L. S. Mullineaux, and R. E. Thomson, Seafloor hydrothermal systems: physical, chemical, biological, and geological interactions, *Washington DC American Geophysical Union Geophysical Monograph Series*, *91*, 1995.

Ishida, H., K. Kaiho, and S. Asano, Effects of a large asteroid impact on ultra-violet radiation in the atmosphere, *Geophysical Research Letters*, *34*(23), doi:10.1029/2007GL030697, 2007.

Izon, G., A. L. Zerkle, I. Zhelezinskaia, J. Farquhar, R. J. Newton, S. W. Poulton, J. L. Eigenbrode, and M. W. Claire, Multiple oscillations in Neoarchaean atmospheric chemistry, *Earth and Planetary Science Letters*, *431*, 264–273, doi:10.1016/j.epsl.2015.09.018, 2015.

Izon, G., A. L. Zerkle, K. H. Williford, J. Farquhar, S. W. Poulton, and M. W. Claire, Biological regulation of atmospheric chemistry en route to planetary oxygenation, *Proceedings of the National Academy of Sciences*, *114*(13), E2571–E2579, doi:10.1073/pnas.1618798114, 2017.

Izon, G., G. Luo, B. T. Uveges, N. Beukes, K. Kitajima, S. Ono, J. W. Valley, X. Ma, and R. E. Summons, Bulk and grain-scale minor sulfur isotope data reveal complexities in the dynamics of Earth's oxygenation, *Proceedings of the National Academy of Sciences*, *119*(13), e2025606,119, doi:10.1073/pnas.2025606119, publisher: Proceedings of the National Academy of Sciences, 2022.

Jamieson, J. W., B. A. Wing, J. Farquhar, and M. D. Hannington, Neoarchaean seawater sulphate concentrations from sulphur isotopes in massive sulphide ore, *Nature Geoscience*, *6*(1), 61–64, doi:10.1038/ngeo1647, 2013.

Johnson, C. M., B. L. Beard, and E. E. Roden, The Iron Isotope Fingerprints of Redox and Biogeochemical Cycling in Modern and Ancient Earth, *Annual Review of Earth and Planetary Sciences*, *36*(1), 457–493, doi:10.1146/annurev.earth.36.031207.124139, 2008.

Johnston, D. T., Multiple sulfur isotopes and the evolution of Earth's surface sulfur cycle, *Earth-Science Reviews*, *106*(1-2), 161–183, doi:10.1016/j.earscirev.2011.02.003, 2011.

Jones-Zimberlin, S., Using impact spherule layers to correlate sedimentary successions: a case study of the Neoarchean Jeerinah layer (Western Australia), *South African Journal of Geology*, *109*(1-2), 245–261, doi:10.2113/gssajg.109.1-2.245, 2006.

Kendall, B., C. T. Reinhard, T. W. Lyons, A. J. Kaufman, S. W. Poulton, and A. D. Anbar, Pervasive oxygenation along late Archaean ocean margins, *Nature Geoscience*, *3*(9), 647–652, doi:10.1038/ngeo942, number: 9 Publisher: Nature Publishing Group, 2010.

Knoll, A. H., and N. J. Beukes, Introduction: Initial investigations of a Neoarchean shelf margin-basin transition (Transvaal Supergroup, South Africa), *Precambrian Research*, *169*(1), 1–14, doi:10.1016/j.precamres.2008.10.009, 2009.

Koehler, M. C., R. Buick, M. A. Kipp, E. E. Stüeken, and J. Zaloumis, Transient surface ocean oxygenation recorded in the 2.66-Ga Jeerinah Formation, Australia, *Proceedings of the National Academy of Sciences*, *115*(30), 7711–7716, doi:10.1073/pnas.1720820115, 2018.

Kohl, I., B. M. Simonson, and M. Berke, Diagenetic alteration of impact spherules in the Neoarchean Monteville layer, South Africa, in *Special Paper 405: Processes on the Early Earth*, vol. 405, pp. 57–73, Geological Society of America, doi:10.1130/2006.2405(04), 2006.

Kuhn, T., A. Wegorzewski, C. Rühlemann, and A. Vink, Composition, Formation, and Occurrence of Polymetallic Nodules, in *Deep-Sea Mining: Resource Potential, Technical and Environmental Considerations*, edited by R. Sharma, pp. 23–63, Springer International Publishing, Cham, doi:10.1007/978-3-319-52557-0_2, 2017.

Lalonde, S. V., and K. O. Konhauser, Benthic perspective on Earth's oldest evidence for oxygenic photosynthesis, *Proceedings of the National Academy of Sciences*, *112*(4), 995–1000, doi:10.1073/pnas.1415718112, 2015.

Large, R., I. Mukherjee, L. Danyushevsky, D. Gregory, J. Steadman, and R. Corkrey, Sedimentary pyrite proxy for atmospheric oxygen; evaluation of strengths and limitations, *Earth-Science Reviews*, p. 103941, doi:10.1016/j.earscirev.2022.103941, 2022.

Large, R. R., et al., Trace element content of sedimentary pyrite as a new proxy for deep-time ocean–atmosphere evolution, *Earth and Planetary Science Letters*, *389*, 209–220, doi:10.1016/j.epsl.2013.12.020, 2014.

Libowitzky, E., Anisotropic pyrite: A polishing effect, *Physics and Chemistry of Minerals*, *21*(1), 97–103, doi:10.1007/BF00205220, 1994.

Liu, J., A. Pellerin, G. Antler, S. Kasten, A. J. Findlay, I. Dohrmann, H. Røy, A. V. Turchyn, and B. B. Jørgensen, Early diagenesis of iron and sulfur in Bornholm Basin sediments: The role of near-surface pyrite formation, *Geochimica et Cosmochimica Acta*, *284*, 43–60, doi:10.1016/j.gca.2020.06.003, 2020a.

Liu, J., A. Pellerin, G. Izon, J. Wang, G. Antler, J. Liang, P. Su, B. B. Jørgensen, and S. Ono, The multiple sulphur isotope fingerprint of a sub-seafloor oxidative sulphur cycle driven by iron, *Earth and Planetary Science Letters*, *536*, 116,165, doi:10.1016/j.epsl.2020.116165, 2020b.

Liu, P., C. E. Harman, J. F. Kasting, Y. Hu, and J. Wang, Can organic haze and O2 plumes explain patterns of sulfur mass-independent fractionation during the Archean?, *Earth and Planetary Science Letters*, *526*, 115,767, doi:10.1016/j.epsl.2019.115767, 2019.

Lyons, T. W., A. D. Anbar, S. Severmann, C. Scott, and B. C. Gill, Tracking Euxinia in the Ancient Ocean: A Multiproxy Perspective and Proterozoic Case Study, *Annual Review of Earth and Planetary Sciences*, *37*(1), 507–534, doi:10.1146/annurev.earth.36.031207.124233, 2009.

Marin-Carbonne, J., C. Rollion-Bard, A. Bekker, O. Rouxel, A. Agangi, B. Cavalazzi, C. C. Wohlgemuth-Ueberwasser, A. Hofmann, and K. D. McKeegan, Coupled Fe and S isotope variations in pyrite nodules from Archean shale, *Earth and Planetary Science Letters*, *392*, 67–79, doi:10.1016/j.epsl.2014.02.009, 2014.

May, P. M., D. Batka, G. Hefter, E. Königsberger, and D. Rowland, Goodbye to S2 in aqueous solution, *Chemical Communications*, *54*(16), 1980–1983, doi:10.1039/C8CC00187A, 2018.

Meyer, N. R., A. L. Zerkle, and D. A. Fike, Sulfur cycling in a Neoarchaean microbial mat, *Geobiology*, *15*(3), 353–365, doi:10.1111/gbi.12227, 2017.

Mishima, K., R. Yamazaki, M. Satish-Kumar, Y. Ueno, T. Hokada, and T. Toyoshima, Multiple sulfur isotope geochemistry of Dharwar Supergroup, Southern India: Late Archean record of changing atmospheric chemistry, *Earth and Planetary Science Letters*, *464*, 69–83, doi:10.1016/j.epsl.2017.02.007, 2017.

Muhling, J. R., and B. Rasmussen, Widespread deposition of greenalite to form Banded Iron Formations before the Great Oxidation Event, *Precambrian Research*, *339*, 105,619, doi:10.1016/j.precamres.2020.105619, 2020.

Mukhopadhyay, J., Archean banded iron formations of India, *Earth-Science Reviews*, p. 102927, doi:10.1016/j.earscirev.2019.102927, 2019.

Murowchick, J. B., Marcasite inversion and the petrographic determination of pyrite ancestry, *Economic Geology*, *87*(4), 1141–1152, doi:10.2113/gsecongeo.87.4.1141, 1992.

Neumann, T., N. Rausch, T. Leipe, O. Dellwig, Z. Berner, and M. E. Böttcher, Intense pyrite formation under low-sulfate conditions in the Achterwasser lagoon, SW Baltic Sea, *Geochimica et Cosmochimica Acta*, *69*(14), 3619–3630, doi:10.1016/j.gca.2005.02.034, 2005.

Nwaila, G., R. Durrheim, O. Jolayemi, H. Maselela, L. Jakaitė, M. Burnett, and S. Zhang, Significance of granite-greenstone terranes in the formation of Witwatersrand-type gold mineralisation – A case study of the Neoarchaean Black Reef Formation, South Africa, *Ore Geology Reviews*, *121*, 103,572, doi:10.1016/j.oregeorev.2020.103572, 2020.

Nwaila, G. T., M. S. D. Manzi, J. Kirk, H. K. Maselela, R. J. Durrheim, D. H. Rose, P. C. Nwaila, L. C. Bam, and T. Khumalo, Recycling of Paleoplacer Gold through Mechanical and Postdepositional Mobilization in the Neoarchean Black Reef Formation, South Africa, *The Journal of Geology*, *127*(2), 137–166, doi:10.1086/701678, publisher: The University of Chicago Press, 2019.

Olson, S. L., C. M. Ostrander, D. D. Gregory, M. Roy, A. D. Anbar, and T. W. Lyons, Volcanically modulated pyrite burial and ocean–atmosphere oxidation, *Earth and Planetary Science Letters*, *506*, 417–427, doi:10.1016/j.epsl.2018.11.015, 2019.

Ono, S., J. L. Eigenbrode, A. A. Pavlov, P. Kharecha, D. Rumble, J. F. Kasting, and K. H. Freeman, New insights into Archean sulfur cycle from mass-independent sulfur isotope records from the Hamersley Basin, Australia, *Earth and Planetary Science Letters*, *213*(1), 15–30, doi:10.1016/S0012-821X(03)00295-4, 2003.

Ono, S., N. J. Beukes, and D. Rumble, Origin of two distinct multiple-sulfur isotope compositions of pyrite in the 2.5 Ga Klein Naute Formation, Griqualand West Basin, South Africa, *Precambiran Research*, *169*(1-4), 48–57, 2009a.

Ono, S., A. J. Kaufman, J. Farquhar, D. Y. Sumner, and N. J. Beukes, Lithofacies control on multiple-sulfur isotope records and Neoarchean sulfur cycles, *Precambrian Research*, *169*(1-4), 58–67, 2009b.

Ostrander, C. M., S. G. Nielsen, J. D. Owens, B. Kendall, G. W. Gordon, S. J. Romaniello, and A. D. Anbar, Fully oxygenated water columns over continental shelves before the Great Oxidation Event, *Nature Geoscience*, *12*(3), 186–191, doi:10.1038/s41561-019-0309-7, number: 3 Publisher: Nature Publishing Group, 2019.

Ostrander, C. M., A. C. Johnson, and A. D. Anbar, Earth's First Redox Revolution, *Annual Review of Earth and Planetary Sciences*, *49*(1), 337–366, doi:10.1146/annurev-earth-072020-055249, _eprint: https://doi.org/10.1146/annurev-earth-072020-055249, 2021.

Ostrander, C. M., et al., An expanded shale δ98Mo record permits recurrent shallow marine oxygenation during the Neoarchean, *Chemical Geology*, *532*, 119,391, doi:10.1016/j.chemgeo.2019.119391, 2020.

Paris, G., J. F. Adkins, A. L. Sessions, S. M. Webb, and W. W. Fischer, Neoarchean carbonate–associated sulfate records positive Δ33S anomalies, *Science*, *346*(6210), 739–741, doi:10.1126/science.1258211, 2014.

Partridge, M. A., S. D. Golding, K. A. Baublys, and E. Young, Pyrite paragenesis and multiple sulfur isotope distribution in late Archean and early Paleoproterozoic Hamersley Basin sediments, *Earth and Planetary Science Letters*, *272*(1), 41–49, doi:10.1016/j.epsl.2008.03.051, 2008.

Picard, A., A. Gartman, and P. R. Girguis, What Do We Really Know about the Role of Microorganisms in Iron Sulfide Mineral Formation?, *Frontiers in Earth Science*, *4*, doi:10.3389/feart.2016.00068, 2016.

Picard, A., A. Gartman, D. R. Clarke, and P. R. Girguis, Sulfate-reducing bacteria influence the nucleation and growth of mackinawite and greigite, *Geochimica et Cosmochimica Acta*, *220*, 367–384, doi:10.1016/j.gca.2017.10.006, 2018.

Pierazzo, E., A. N. Hahmann, and L. C. Sloan, Chicxulub and Climate: Radiative Perturbations of Impact-Produced S-Bearing Gases, *Astrobiology*, *3*(1), 99–118, doi:10.1089/153110703321632453, 2003.

Preibisch, S., S. Saalfeld, and P. Tomancak, Globally optimal stitching of tiled 3D microscopic image acquisitions, *Bioinformatics*, *25*(11), 1463–1465, doi:10.1093/bioinformatics/btp184, 2009.

Qian, G., F. Xia, J. Brugger, W. M. Skinner, J. Bei, G. Chen, and A. Pring, Replacement of pyrrhotite by pyrite and marcasite under hydrothermal conditions up to 220 C: An experimental study of reaction textures and mechanisms, *American Mineralogist*, *96*(11-12), 1878–1893, doi:10.2138/am.2011.3691, 2011.

Rickard, D., Chapter 6 - Sedimentary Pyrite, in *Sulfidic Sediments and Sedimentary Rocks*, *Developments in Sedimentology*, vol. 65, edited by D. Rickard, pp. 233 – 285, Elsevier, doi:10.1016/B978-0-444-52989-3.00006-4, 2012a.

Rickard, D., Chapter 13 - Euxinic Systems, in *Sulfidic Sediments and Sedimentary Rocks*, *Developments in Sedimentology*, vol. 65, edited by D. Rickard, pp. 495 – 542, Elsevier, doi:10.1016/B978-0-444-52989-3.00013-1, 2012b.

Rickard, D., Chapter 9 - Microbial Sulfide Oxidation in Sediments, in *Sulfidic Sediments and Sedimentary Rocks*, *Developments in Sedimentology*, vol. 65, edited by D. Rickard, pp. 353 – 372, Elsevier, doi:10.1016/B978-0-444-52989-3.00009-X, 2012c.

Roerdink, D. L., P. R. D. Mason, J. Farquhar, and T. Reimer, Multiple sulfur isotopes in Paleoarchean barites identify an important role for microbial sulfate reduction in the early marine environment, *Earth and Planetary Science Letters*, *331-332*, 177–186, doi:10.1016/j.epsl.2012.03.020, 2012.

Roychoudhury, A. N., J. E. Kostka, and P. Van Cappellen, Pyritization: a palaeoenvironmental and redox proxy reevaluated, *Estuarine Coastal and Shel Science*, *57*, 1183–1193, 2003.

Schieber, J., The Role of an Organic Slime Matrix in the Formation of Pyritized Burrow Trails and Pyrite Concretions, *PALAIOS*, *17*(1), 104–109, doi:10.1669/0883-1351(2002)017⟨0104:TROAOS⟩2.0.CO;2, 2002a.

Schieber, J., Sedimentary pyrite: A window into the microbial past, *Geology*, *30*(6), 531–534, doi:10.1130/0091-7613(2002)030⟨0531:SPAWIT⟩2.0.CO;2, 2002b.

Schieber, J., Oxidation of detrital pyrite as a cause for Marcasite Formation in marine lag deposits from the Devonian of the eastern US, *Deep Sea Research Part II: Topical Studies in Oceanography*, *54*(11), 1312–1326, doi:10.1016/j.dsr2.2007.04.005, 2007.

Schieber, J., Iron Sulfide Formation, in *Encyclopedia of Geobiology*, edited by J. Reitner and V. Thiel, pp. 486–502, Springer Netherlands, Dordrecht, doi:10.1007/978-1-4020-9212-1_118, 2011.

Schieber, J., and L. Riciputi, Pyrite and Marcasite Coated Grains in the Ordovician Winnipeg Formation, Canada: An Intertwined Record of Surface Conditions, Stratigraphic Condensation, Geochemical Reworking, and Microbial Activity, *Journal of Sedimentary Research*, *75*(5), 907–920, doi:10.2110/jsr.2005.070, 2005.

Schoonen, M. A. A., and H. L. Barnes, Reactions forming pyrite and marcasite from solution: II. Via FeS precursors below 100°C, *Geochimica et Cosmochimica Acta*, *55*(6), 1505–1514, doi: 10.1016/0016-7037(91)90123-M, 1991a.

Schoonen, M. A. A., and H. L. Barnes, Reactions forming pyrite and marcasite from solution: I. Nucleation of FeS2 below 100°C, *Geochimica et Cosmochimica Acta*, *55*(6), 1495–1504, doi: 10.1016/0016-7037(91)90122-L, 1991b.

Schröder, S., J. P. Lacassie, and N. J. Beukes, Stratigraphic and geochemical framework of the Agouron drill cores, Transvaal Supergroup (Neoarchean-Paleoproterozoic, South Africa), *South African Journal of Geology*, *109*, 23–54, 2006.

Scott, C. T., A. Bekker, C. T. Reinhard, B. Schnetger, B. Krapež, D. Rumble, and T. W. Lyons, Late Archean euxinic conditions before the rise of atmospheric oxygen, *Geology*, *39*(2), 119–122, doi:10.1130/G31571.1, 2011.

Sen, A., S. Mukhopadhyay, P. Samanta, A. Ghosh, and D. Pal, Micro-Facies Analysis and Geochemistry of Shaley-Banded Iron Formations (S-Bifs) from Late-Archaean Kushtagi-Hungund Schist Belt (KHSB), Karnataka, South Indian Shield (SIS), *Authorea Preprints*, publisher: Authorea, 2022.

Simonson, B. M., and K. E. Carney, Roll-up structures; evidence of in situ microbial mats in late Archean deep shelf environments, *PALAIOS*, *14*(1), 13–24, doi:10.2307/3515358, 1999.

Simonson, B. M., and B. P. Glass, Spherule Layers – Records of Ancient Impacts, *Annual Review of Earth and Planetary Sciences*, *32*, 329–361, doi:https://doi.org/10.1146/annurev.earth.32.101802.120458, 2004.

Simonson, B. M., S. W. Hassler, and N. J. Beukes, Late Archean impact spherule layer in South Africa that may correlate with a Western Australian layer, in *Large Meteorite Impacts and Planetary Evolution II*, no. 339 in Geological Society of America Special Papers, pp. 249–261, Geological Society of America, Boulder, Colorado, 1999.

Simonson, B. M., D. Davies, and S. W. Hassler, Discovery of a layer of probable impact melt spherules in the Late Archaean Jeerinah Formation, Fortescue Group, Western Australia, *Australian Journal of Earth Sciences*, *47*(2), 315–325, doi:10.1046/j.1440-0952.2000.00784.x, 2000a.

Simonson, B. M., M. Hornstein, and S. Hassler, Particles in late archean carawine dolomite (Western Australia) resemble muong nong-type tektites, in *Impacts and the Early Earth*, edited by I. Gilmour and C. Koeberl, Lecture Notes in Earth Sciences, pp. 181–213, Springer, Berlin, Heidelberg, doi:10.1007/BFb0027760, 2000b.

Simonson, B. M., I. McDonald, A. Shykolyukov, C. Koeberl, W. U. Reimold, and G. W. Lugmair, Geochemistry of 2.63-2.49 Ga impact spherule layers and implications for stratigrahic correlations and impact processes, *Precambrian Research*, *175*, 51–76, 2009a.

Simonson, B. M., D. Y. Sumner, N. J. Beukes, S. Johnson, and J. Gutzmer, Correlating multiple Neoarchean–Paleoproterozoic impact spherule layers between South Africa and Western Australia, *Precambrian Research*, *169*(1), 100–111, doi:10.1016/j.precamres.2008.10.016, 2009b.

Simonson, B. M., N. J. Beukes, and S. Biller, Extending the paleogeographic range and our understanding of the Neoarchean Monteville impact spherule layer (Transvaal Supergroup, South Africa), *Meteoritics & Planetary Science*, *0*(0), 1–24, doi:10.1111/maps.13228, 2018.

Sindhuja, C. S., C. Manikyamba, A. Pahari, and M. Satyanarayanan, Geochemistry of banded sulphidic cherts of Sandur greenstone belt, Dharwar Craton, India: Constraints on hydrothermal processes and gold mineralization, *Ore Geology Reviews*, *122*, 103,529, doi:10.1016/j.oregeorev.2020.103529, 2020.

Slotznick, S. P., J. E. Johnson, B. Rasmussen, T. D. Raub, S. M. Webb, J.-W. Zi, J. L. Kirschvink, and W. W. Fischer, Reexamination of 2.5-Ga "whiff" of oxygen interval points to anoxic ocean before GOE, *Science Advances*, *8*(1), eabj7190, doi:10.1126/sciadv.abj7190, 2022.

Spiess, F. N., et al., East Pacific Rise: Hot Springs and Geophysical Experiments, *Science*, *207*, 1421–1433, doi:10.1126/science.207.4438.1421, aDS Bibcode: 1980Sci...207.1421S, 1980.

Stüeken, E. E., D. C. Catling, and R. Buick, Contributions to late Archaean sulphur cycling by life on land, *Nature Geoscience*, *5*(10), 722–725, doi:10.1038/ngeo1585, number: 10 Publisher: Nature Publishing Group, 2012.

Sumner, D. Y., Late Archean Calcite-Microbe Interactions: Two Morphologically Distinct Microbial Communities that Affected Calcite Nucleation Differently, *PALAIOS*, *12*, 302–318, 1997.

Sumner, D. Y., and N. J. Beukes, Sequence Stratigraphic Development of the Neoarchean Transvaal Craton, South Africa, *South African Journal of Geology*, *109*, 11–22, 2006.

Thibon, F., J. Blichert-Toft, H. Tsikos, J. Foden, E. Albalat, and F. Albarede, Dynamics of oceanic iron prior to the Great Oxygenation Event, *Earth and Planetary Science Letters*, *506*, 360–370, doi:10.1016/j.epsl.2018.11.016, 2019.

Torres, M. A., G. Paris, J. F. Adkins, and W. W. Fischer, Riverine evidence for isotopic mass balance in the Earth's early sulfur cycle, *Nature Geoscience*, *11*(9), 661–664, doi:10.1038/s41561-018-0184-7, number: 9 Publisher: Nature Publishing Group, 2018.

Watanabe, Y., J. Farquhar, and H. Ohmoto, Anomalous Fractionations of Sulfur Isotopes During Thermochemical Sulfate Reduction, *Science*, *324*(5925), 370–373, doi:10.1126/science.1169289, 2009.

Wilkin, R. T., and H. L. Barnes, Pyrite formation by reactions of iron monosulfides with dissolved inorganic and organic sulfur species, *Geochimica et Cosmochimica Acta*, *60*(21), 4167–4179, doi:10.1016/S0016-7037(97)81466-4, 1996.

Wille, M., J. D. Kramers, T. F. Nägler, N. J. Beukes, S. Schröder, T. Meisel, J. P. Lacassie, and A. R. Voegelin, Evidence for a gradual rise of oxygen between 2.6 and 2.5Ga from Mo isotopes and Re-PGE signatures in shales, *Geochimica et Cosmochimica Acta*, *71*(10), 2417–2435, doi:10.1016/j.gca.2007.02.019, 2007.

Williford, K. H., et al., Carbon and sulfur isotopic signatures of ancient life and environment at the microbial scale: Neoarchean shales and carbonates, *Geobiology*, *14*(2), 105–128, doi:10.1111/gbi.12163, 2016.

Wilmeth, D. T., F. A. Corsetti, N. J. Beukes, S. M. Awramik, V. Petryshyn, J. R. Spear, and A. J. Celestian, Neoarchean (2.7Ga) lacustrine stromatolite deposits in the Hartbeesfontein Basin, Ventersdorp Supergroup, South Africa: Implications for oxygen oases, *Precambrian Research*, *320*, 291–302, doi:10.1016/j.precamres.2018.11.009, 2019.

Wilmeth, D. T., et al., Evidence for benthic oxygen production in Neoarchean lacustrine stromatolites, *Geology*, *50*(8), 907–911, doi:10.1130/G49894.1, 2022.